THESIS

FTIR SPECTROSCOPY OF METHYL BUTANOATE-AIR AND PROPANE-AIR LOW PRESSURE FLAT FLAMES

Submitted by

Kristen Ann Naber

Department of Mechanical Engineering

In partial fulfillment of the requirements

For the Degree of Master of Science

Colorado State University

Fort Collins, Colorado

Fall 2012

Master's Committee:

Advisor: Anthony Marchese

Xinfeng Gao
Kimberly Catton

ABSTRACT

FTIR SPECTROSCOPY OF METHYL BUTANOATE-AIR AND PROPANE-AIR LOW PRESSURE FLAT FLAMES

The combustion of fatty acid methyl esters (FAME) in diesel engines has been shown to produce lower emissions of carbon monoxide (CO), unburned hydrocarbons, greenhouse carbon dioxide (CO_2), and particulate matter than petroleum based fuels. However, most diesel engine studies have shown that emission of oxides of nitrogen (NO_x) typically increase for methyl ester fuels in comparison to petroleum based fuels. Many theories have been proposed to explain these NO_x increases from FAME combustion but a general consensus has emerged toward two primary mechanisms: (1) the increased bulk modulus of biodiesel results in earlier fuel injection into the cylinder and/or (2) the presence of oxygen in the fuel results in a leaner (but still rich) premixed autoignition zone thereby increasing the local flame temperature during the premixed burn phase. It is well known that NO_x is produced during the combustion of hydrocarbons in air from three different mechanisms: prompt NO_x, thermal NO_x, and via fuel bound nitrogen. Both of the mechanisms that have been proposed to explain the observed NO_x increases from the combustion of FAME in diesel engines are related to the thermal NO_x production route. However, no quantitative data exist on local in-cylinder temperatures and associated in-cylinder NO production during the premixed autoignition phase to experimentally verify these hypotheses. The present work is aimed at developing an experimental approach to examine a third hypothesis that suggests that the chemical structure of methyl esters results in an increase in prompt NO_x in comparison to non-oxygenated hydrocarbons. This new hypothesis has the potential to be verified by conducting experiments with steady, laminar flames. Accordingly, in

the present study, low pressure, flat flame burner experiments were conducted, which enabled direct temperature measurements using a thermocouple and direct species sampling using a quartz microprobe. The fuels used in the flame experiments were propane (C_3H_8) and methyl butanoate ($C_5H_{10}O_2$), a small methyl ester fuel whose chemical kinetic mechanism has been the subject of substantial research in the past decade. The gas samples were directed to an FTIR spectrometer for analysis of various species including NO, CO, and CO_2. Equivalence ratios of φ = 0.8, 1.0, and 1.2 were examined for both fuels. Temperatures were obtained using coated Pt-Pt/13%Rh type R thermocouples and were corrected for radiation losses. In addition to the experiments, laminar flame modeling studies were conducted using CHEMKIN for the both fuel types at each equivalence ratio using existing detailed chemical kinetic mechanisms to predict temperature and species concentrations. Because no methyl butanoate mechanisms containing detailed NO_x chemistry exist, the propane/NO_x chemical kinetic mechanism of Konnov and was combined with a detailed methyl butanoate mechanism Gail and coworkers. Experimental and modeling results show that nitric oxide production in the steady, premixed laminar methyl butanoate flames did not differ substantially from that produced in similar propane flames. Results were inconclusive on which nitric oxide formation mechanisms contributed to the overall measured concentrations.

ACKNOWLEDGEMENTS

First, I would like to thank Dr. Anthony Marchese for providing me with the opportunity and guidance he offered throughout the course of this project. It was a long road, and I really appreciate the time and effort you spent on this work. A thank you is also owed to Ph. D candidates, Tim Vaughn and Torben Grumstrup for their assistance in bringing the present work to fruition. All members of the ABC^2 lab were essential, providing plenty of knowledge and encouragement when it was needed. I wish each of them the best of luck in their future endeavors. Thank you as well to the staff and students of the EECL for providing such an exciting and diverse work environment. Finally, a big thanks goes to Nick Wilvert for bringing me food on late work nights and pushing me to finish the work required for this degree.

Funding of this work was provided by the US Department of Energy under contract DE-EE0003046 awarded to the National Alliance for Advance Biofuels and Bioproducts, along with a Graduate Teaching Assistantship provided by the Department of Mechanical Engineering at CSU. I would like to give special thanks to the NAABB and the Department of Mechanical Engineering at CSU for their financial assistance throughout the Master of Science degree program.

TABLE OF CONTENTS

LIST OF TABLES

LIST OF FIGURES

1. Introduction

1.1 Motivation for Biofuel Investigation

Emissions of greenhouse gases (GHG) from anthropogenic sources such as the combustion of fossil fuels have resulted in a substantial increase in atmospheric concentration of GHG's and has threatened to produce significant climate change over a relatively short period of time. Climate change, also known as global warming, refers to an increase in the Earth's average temperature, and has been well documented in locations across the globe. Continuous combustion of fossil fuels causes GHG's to accumulate in the atmosphere, causing a greenhouse effect in the Earth's atmosphere. Specifically, the GHG's affect the absorption, scattering, and emission of radiation within the atmosphere and at the Earth's surface, resulting in radiative forcing on global climate [1]. The effects of global warming have become increasingly evident in the climate record, where rate and magnitude of warming due to increased atmospheric concentration of GHG's is directly comparable to observed increases in temperature [2]. In 2007, the Intergovernmental Panel on Climate Change produced a report which concluded that the occurrence of global warming is largely due to carbon dioxide (CO_2) emissions from the combustion of fossil fuels [1].

In addition to GHG emissions, the combustion of fossil fuels also produces a myriad of other pollutants such as unburned hydrocarbons (HC), carbon monoxide (CO), oxides of nitrogen (NO_x), particulate matter (PM) and other hazardous air pollutants. These pollutants have not only affect the atmosphere and local air quality, but also adversely affect human health. Specifically, pollutants produced from the burning of fossil fuels contribute to smog, ground level ozone, and a variety of other negative health effects [3].

Reliance on fossil fuels not only appears to be causing long-term damage to the climate and our health but our ever increasing consumption means that the peak of petroleum production is also imminent [2]. The term **"**peak oil" has been coined as the point in history when conventional liquid fossil fuel production transitions from the period of increased production to the period of decline [4]**.** Current estimates predict that world petroleum resources will approach exhaustion in the next 50 years, while some predict a sooner occurrence. This figure can be affected by many factors including natural disasters, political occurrences, or by efforts made to increase conservation and alternative energy production, making it difficult to produce an accurate projection [5].

According to the U.S. Energy Information Administration the United States consumed 18.8 million barrels per day of petroleum products during 2011, making it the largest consumer of petroleum in the world. Approximately 45% of crude oil used in 2011 was imported from other countries [6].

To establish energy independence and to reduce contributions to global warming, the U.S. must produce alternatives to petroleum based fuels. Biofuels have gained the attention of both researchers and policy makers as a potential way to help mitigate the effects of global warming and fossil fuel depletion [7].

Biofuels are of increasing interest as alternatives to petroleum-based transportation fuels because they offer the long term promise of fuel-source regeneration and reduced climatic impact. [8] Most biofuels produce a net reduction in greenhouse CO2 emissions. The amount of CO_2 taken in by the plant in the growth process offsets a portion of that displaced when the biofuel is burned, leading to a significant overall reduction in GHGs. The Department of Energy's (DOE) Replacement Fuel Goal under the Alternative Fuel Transportation Program has

mandated that 30% of U.S. motor fuel consumption be replaced with alternative fuels by the year 2030 [9].

1.2 Biodiesel

Biodiesel is an oxygenated, diesel-like fuel consisting of fatty acid alkyl esters, most commonly fatty acid methyl esters (FAME), which are derived from vegetable oils, animal fats, or algae oil through a process called transesterification. In the transesterification process, triglycerides are reacted with methanol to form methyl esters by use of a catalyst, typically potassium hydroxide (KOH) or sodium hydroxide (NaOH). As can be seen in figure 1-1, the transesterification process splits the triglyceride molecule into a mixture of these methyl esters, with glycerol as a byproduct.

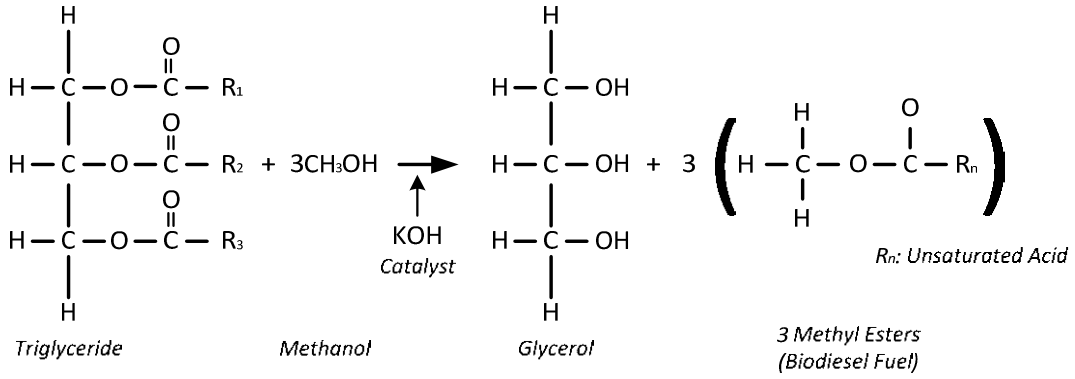

Figure 1-1: Chemical reaction for the transesterification process [10].

While it is possible, in principle, to directly burn straight vegetable oil (SVO) in a diesel engine, the triglycerides in pure animal fat and SVO have approximately three times the molecular mass of biodiesel, resulting in higher viscosity, lower vapor pressure, higher pour point and poor cold temperature properties. These characteristics can lead to severe engine deposits, congealing of fuel in the engine and fuel lines, as well as higher exhaust emissions. The

transesterification process improves the combustion characteristics and usability of the oil or fat, giving it properties closer to that of petroleum diesel [10].

Although biodiesel production is not completely carbon neutral, numerous lifecycle analyses (LCA) of biodiesel production have been have been performed to estimate the total emissions of greenhouseCO_2 and other pollutants, as well as energy requirements in the production and transportation of the fuel. For example, one such study by Sheehan et al. found that using biodiesel reduces net CO_2 emissions by nearly 80% compared to petroleum diesel [11].

Biodiesel is biodegradable, non-toxic, and can be used in its pure form, or as a blend with petroleum-derived fuel, giving it the advantage of being generally compatible with existing combustion technologies and fuel infrastructure. The oxygenated chemical structure of biodiesel alters combustion and leads to differences in performance factors such as reactivity and pollutant formation [12] The effects of biodiesel and biodiesel blends on emissions have been studied extensively.

In addition to reduced lifecycle GHG emissions, the combustion of biodiesel in diesel engines also results in reduced pollutant emissions of CO, HC and PM in comparison to petroleum diesel. Figure 1-2 is a plot of percentage change in emissions of CO, HC and PM as a function of the percentage of biodiesel in petroleum diesel/biodiesel blends [13]. The figure was generated by the U.S. EPA based on the data from numerous diesel engine studies conducted over several decades. Regression analysis of the data from the numerous engines studies suggests that combustion of 100% biodiesel in a diesel engine results in a reduction of 50% in CO and PM emissions, and a reduction of 65% in HC emissions.

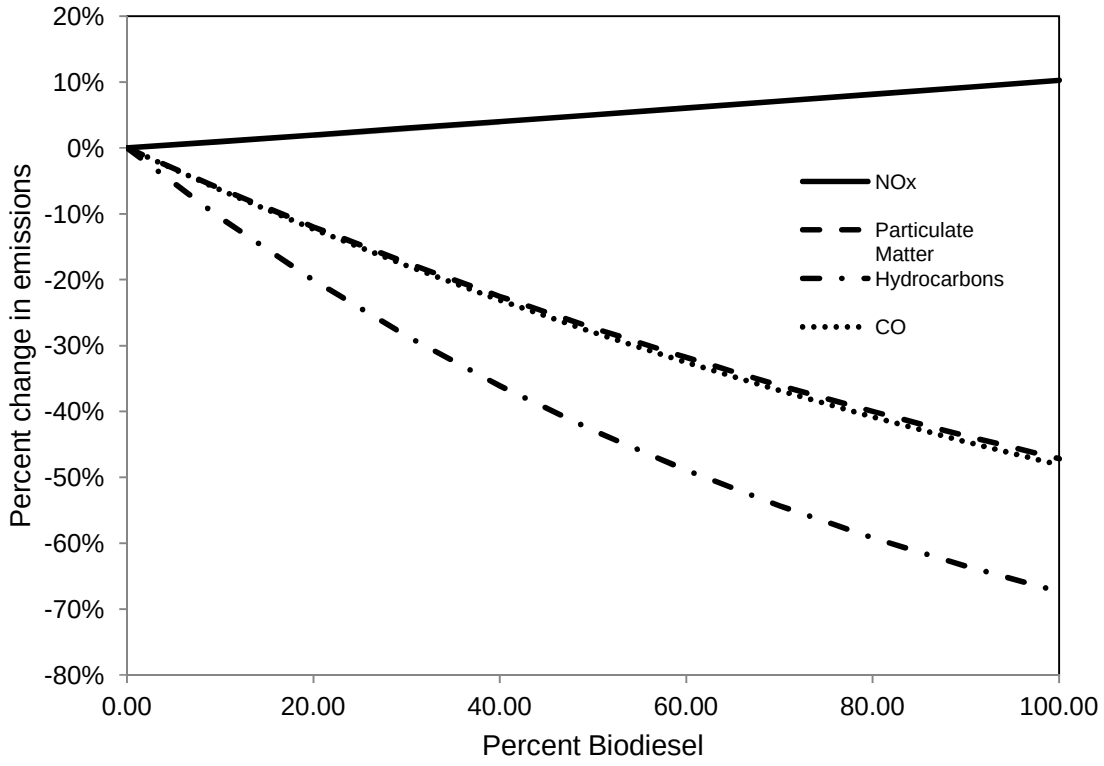

Figure 1-2: Average emission impact of biodiesel (heavy-duty highway engines) [13].

Studies by Lapuerta and coworkers [14] and Fisher et al. [15] showed that overall particulate matter in biodiesel combustion was reduced. However, the average particle size decreased and the organic matter content of the particles increased. These smaller particles can be inhaled deeper into the lungs, and organic matter has been linked to health problems including respiratory disease, cancer, and heart disease. [3]

While most emissions from biodiesel combustion are reduced when compared to petroleum diesel, emissions of nitrogen oxides (NO_x) have been found to generally increase with biodiesel. As shown in Fig. 1-2, the U.S. EPA study suggested that 100% biodiesel fuel will produce a 10% increase in NO_x emissions [13]. NO_x emissions are stringently regulated in the U.S. because of their contribution to photochemical smog and ground level ozone, which can

cause a variety of respiratory diseases, and even damage to crops. Acid rain is another byproduct of NO_x, which can cause damage to man-made structures and increase the acidity of waterways, making them unsuitable for aquatic life [16]. Nitric oxide (NO) is the most relevant NO_x pollutant species for combustion processes, emitted even when clean fuels like natural gas or hydrogen are burned, because it is formed from the reaction between the nitrogen and oxygen in the air at the high temperatures found in the combustion environment [17]. NO and PM emissions from biodiesel use in conventional diesel engines have been studied by multiple groups, and most have found that PM decreases as the biodiesel content in the fuel blend increases. However, there have been contradictory conclusions stemming from research into the effect of biodiesel production on NO_x emissions.

1.2.1 **Biodiesel Feedstocks**

In recent years, ethanol and biodiesel, produced from corn and soy feedstocks, respectively, have gained a large amount of interest as viable alternatives to reducing the current problems brought about by petroleum fuels. However, soybeans and corn, the main feedstocks used production of biodiesel, compete directly with the food and livestock industry. Another issue that is problematic, particularly in the case of soy biodiesel, is that the oil yield per area per year from soy biodiesel feedstock is too low to make a significant impact in replacing fossil fuels and meeting the goals of the DOE. Other feedstocks are being investigated for the potential to contribute to the DOE's fuel goals as well. The oil yields per land use for some of these feedstocks are outlined in Table 1-1, reproduced from [18]. Most of the crops included in this table are largely used in the global food supply and some might argue that it is not ethically or economically feasible to increase their production to contribute significantly to overall biofuel

production. Table 1-1 also highlights the amount of land area that would be needed to produce 100% of transportation fuels consumed by the U.S., as well as the current total U.S. crop area for that specific feedstock. Microalgae based fuel appears to have the greatest potential to produce enough oil in a reasonable amount of land area. To take advantage of all the potential benefits of biodiesel, the issues stemming from land use and increased nitric oxide emissions must be rectified.

Table 1-1: Oil yield and land use of biodiesel feedstocks adapted from [3], [18]

Crop	Oil Yield (gal/acre)	Land area needed (M acre)[a]	Percent of existing US crop area.[a]
Corn	18	7610	1692
Soybean	48	2935	652
Canola	127	1102	244
Jatropha	202	692	154
Coconut	287	489	108
Oil Palm	636	222	48
Microalgae[b]	6275	22	5

[a]For meeting 100% of all transport fuels in the United States

[b]For meeting Assuming 30% oil (by wt.) in biomass

The 2007 Energy Independence and Security Act (EISA) requires that 21 billion gallons of *advanced biofuels* be produced in the U.S. by 2022. The EISA defines an *advanced biofuel* as a renewable fuel, other than ethanol derived from corn starch, with lifecycle greenhouse gas emissions that are at least 50% less than baseline lifecycle greenhouse gas emissions [19]. Over the period from 2001 to 2011, biodiesel production increased from 9 million gallons to 967 million gallons, and the year 2012 is already on track to supersede 2011 production. Although this is a significant increase, the U.S. has a long way to go before meeting the goals set forth by the DOE and EISA.

1.2.2 NO_x Formation from Combustion of Fuels in Air

As mentioned previously, NO_x emissions can pose a serious threat to both the environment and human health. To mitigate NO_x emissions it is necessary to precisely understand the formation of NO during the combustion of fuels in air. Nitric oxide (NO) can be formed through three specific mechanisms: thermal NO, prompt NO and fuel NO. Each of these NO formation mechanisms will be described briefly below.

1.2.3 Thermal NO_x

Thermal NO forms from oxidation of atmospheric nitrogen at relatively high temperatures in fuel-lean environments and has strong temperature dependence [20]. The thermal NO mechanism, also referred to as the Zeldovich mechanism, consists of three main reactions:

$$O + N_2 \overset{k_1}{\leftrightarrow} N + NO \quad (1.1)$$

$$N + O_2 \overset{k_2}{\leftrightarrow} O + NO \quad (1.2)$$

$$N + OH \overset{k_3}{\leftrightarrow} H + NO \quad (1.3)$$

where the reactions are reversible, and k_1, k_2, and k_3 are rate constants. These reactions are highly dependent on temperature, residence time, and atomic oxygen concentration. The rate determining step is the first reaction due to its high activation energy (N_2 triple bond is broken). The formation of NO is also dependent on the availability of O_2 in the combustion environment, and as a result NO emission peaks on the slightly lean side of stoichiometry [21]. At temperatures below 1600-1800 K thermal NO formation is significantly reduced, making it much less prevalent in fuel-rich environments [20]. Thermal NO is typically prevalent in diesel engines, because diesel combustion produces high local combustion temperatures. In order to

reduce the rate of thermal NO production and consequently the overall NO formation, the temperature in the combustion chamber must be reduced.

1.2.4 **Prompt NO_x**

The thermal NO_x formation route is well established as the mechanism for NO formation in regions of the flame where high temperatures dominate. However, observations that NO levels did not extrapolate to zero at the flame front in premixed flat flame experiments led Fenimore [22] to postulate a "prompt NO" mechanism [23]. There exists substantial NO formation in the upstream, cold part of premixed hydrocarbon flames, where the O atom concentration is relatively low, and thermal NO_x cannot fully explain NO production; this formation tends to increase as the unburned mixture becomes fuel rich [21]. Prompt NO is formed by the reaction of atmospheric nitrogen with hydrocarbon radicals, which is subsequently oxidized to form NO [20]. Fenimore was the first to propose that the initial reaction that begins the prompt NO_x sequence was as follows:

$$N_2 + CH \rightarrow HCN + H \qquad (1.4)$$

For the several decades this became generally accepted as the major initiation step in prompt NO formation, and was included in all detailed NO_x mechanisms. However, in 2000, Moskaleva and Lin [24] reported that the reaction in (1.4) in the electronic ground state is spin forbidden and must be replaced with:

$$CH + N_2 \rightarrow NCN + H \qquad (1.5)$$

Oxidation reactions of NCN with O_2, O, H, and OH present routes back to standard nitrogen flame chemistry with chemical pathways consistent with established NO formation pathways, such as those presented in equations 1.2 and 1.3. Methane flame studies by Smith

[25], Sutton et al. [26], and Lamoureux et al. [27] demonstrate that the step in equation 1.5 is the most probable initial step in the prompt NO formation process. Smith determined this quantitatively by showing that the relative spatial distribution (height in flame) of NCN with respect to CH was consistent with NCN being the primary product from the reaction in equation 1.5 [25]. Sutton and coworkers conducted laser induced fluorescence (LIF) experiments on varying stoichiometry low pressure methane flames to quantify both NCN and CH and determined that there was high correlation in spatial distribution and concentration between the two, also consistent with NCN as a product of equation 1.5 [26]. Lamoureux and coworkers saw similar results using both LIF and cavity ring down spectroscopy (CRDS) methods on methane and acetylene flames of varying stoichiometry [27].

Several recent studies have suggested that species other than CH must be considered in the production of NCN and subsequent prompt NO_x production, due to increasing disagreement between calculations and experimental results, especially as alkane fuels increase in size, and the number of carbon atoms within a fuel increase. Sutton et al, mention that the C_2O molecule may be a plausible candidate as its reaction with N_2 is exothermic and the product channel could include NCN + CO, which proceeds to form NO, and that because it contains two carbon atoms it is likely to be produced in increasing fuel size [28]. The reaction in equation 1.6 was suggested for consideration by Williams and Fleming [29]:

$$C_2O + N_2 \rightarrow NCN + CO \qquad (1.6)$$

Konnov added this reaction to his small hydrocarbon mechanism with NO_x chemistry and found that in rich methane/air flames the reaction of C_2O with N_2 accounted for 24% of the rate of production of NCN, and its inclusion yielded better agreement with experimentally measured NO levels [30]. Marchese and coworkers performed further modeling studies, finding that the

Konnov mechanism predicted that the rate of NCN production from reaction 1.6 was over 4 times that produced by reaction 1.5, a much more dramatic effect that that predicted by Konnov. Further studies are currently underway at CSU to understand the role of C_2O in prompt NO_x production.

1.2.5 **Fuel NO_x**

Fuel NO_x forms when nitrogen that is chemically bound to the fuel combines with excess oxygen during the combustion process, and only occurs when the fuel in use contains nitrogen. The main pathway for this type of NO production involves the creation of intermediate species such as HCN, NH_3, NH, or CN, which then undergo the oxidation process to form NO. Because chemically bound nitrogen is not typically found in biodiesel, this NO_x formation route is generally not considered to contribute to the NO_x increases observed from biodiesel combustion in diesel engines.

1.2.6 **Biodiesel NO_x Formation**

As mentioned previously, the combustion of biodiesel in diesel engines typically results in reduced emissions of PM, CO, CO_2, HC as well as volatile organic compounds and sulfur oxides (SO_x), while increasing the emissions of NO_x. Many different effects including injection timing, combustion phasing (ignition/rate of combustion/heat release), premixing, adiabatic flame temperature, radiative heat transfer, and chemical kinetics have been proposed to be contributors to biodiesel NO_x increase and are discussed below.

An advance in injection timing, caused by the higher bulk modulus of the biodiesel, leads to an earlier start of combustion, causing longer residence times and higher in-cylinder

temperatures, thus leading to an increase in NO_x emissions. This has been well studied and researchers have found that, by retarding ignition timing, NO_x production can be controlled. Results show that the timing at which maximum cylinder temperatures and heat release rates occurred had more of an effect on NO_x production than the magnitude of the maximum temperature and maximum heat release [31]. Various other methods have been employed to decrease NO_x formation in engines such as exhaust gas recirculation (EGR), selective catalytic reduction (SCR), and direct water injection. Engine calibration is a large part of controlling NO emissions, but the combustion of the fuel must be well understood in order to try to mitigate these effects.

Biodiesel typically has a higher Cetane Number than conventional diesel, causing earlier ignition of the fuel. Because the combustion event occurs at a faster rate, higher in-cylinder temperatures and longer overall combustion residence times occur. Also, when fuel and air are premixed oxygen concentration is elevated and creates a hotter, leaner flame. The higher oxygen content of biodiesel allows fuel and air to premix more fully during ignition delay, and a larger fraction of heat release occurs during this premixed-burn phase. The aforementioned effects, along with increased bulk mean gas temperatures from reduced radiative heat loss (due to decreased PM production) are expected to lead to increased thermal NO_x production.

The chemical kinetic pathways of biodiesel and petroleum diesel oxidation vary substantially. Biodiesel fuels are larger and more complex than hydrocarbons such as propane and methane, which have historically been used for prompt NO_x studies. To fully characterize the complete oxidation mechanism of biodiesel, chemical kinetic mechanisms on the order of 3000 species are needed, in comparison to less than 100 species for methane or propane.

Therefore, it is presently challenging to elucidate the role of prompt NO_x in the observed NOx increases from biodiesel combustion in diesel engines.

However, it has been suggested that biodiesel might produce higher levels of CH in the autoignition zone (where the fuel begins to ignite) resulting in increased prompt NO_x formation. It has also been hypothesized that methyl esters produce higher levels of C_2O radical via methyl ester decomposition pathways that form stable oxygenated species such as ethenone (CH_2CO) and propadienone (CH_2CCO) [23].

Mueller and Boehman performed several studies with soy biodiesel in a highly modified optical engine in an attempt to understand a number of these various effects on the increase of biodiesel NO_x formation relative to petroleum diesel [32]. Their results suggest that the biodiesel NO_x increase is a result of a number of coupled mechanisms whose effects may tend to reinforce or cancel one another under different conditions, depending on specific combustion and fuel characteristics [32]. They concluded that the presence of oxygen in the fuel results in a leaner (but still rich) premixed autoignition zone thereby increasing the local flame temperature during the premixed burn phase. If this is indeed the case, however, then such an effect would be found with any oxygenated fuel burned in a diesel engine.

Various characteristics of biodiesel fuel, including density, Cetane Number, and degree of unsaturation, are also expected to play a substantial role in the formation of NO_x, Degree of unsaturation refers to the number of carbon double bonds that exist in the fuel molecule. McCormick and coworkers found that NO_x emissions increased for increasing fuel density or decreasing Cetane Number. Also, increasing the degree of unsaturation correlated with increased NO_x emissions. This led them to predict that for some fuels increased NO_x formation

is not driven by the thermal route. Also, for fully saturated fatty acid chains, NO_x appeared to increase when the carbon chain lengths decreased from 18 to 12 molecules [33].

In contrast, the recent engine research performed by Fisher et al. [15] showed that the highly unsaturated methyl esters, C20:5 and C22:6, did not follow the trend of increased NO_x with increasing number of double bonds presented by McCormick et al.

1.3 Methyl Butanoate

To evaluate the consequences of biodiesel use on engine performance and the environment, it is essential to advance our fundamental understanding of the oxidation of methyl esters. Achieving such understanding in well-controlled environments will allow for distinguishing the roles that the physical and chemical properties of biofuels play in determining the behavior that is observed and measured in engines [34]. In recent years, several biodiesel mechanisms have been developed by Westbrook and coworkers. [35] However, these mechanisms are relatively large, containing between 3000 and 5000 species, which is simply too large to validate against even 1-D steady flames. These mechanisms are slightly more feasible when used for 0-D modeling of apparatuses including shock tubes and rapid compression machines (RCM). The larger molecule size associated with biodiesel has made development and validation of kinetic models difficult. Only recently, have studies on lower molecular weight fuels that can act as surrogate candidates for complex biodiesel fuels begun to take place [36].

Methyl butanoate (MB, $C_5H_{10}O_2$) is a useful biodiesel surrogate fuel that possesses the primary structural features of biodiesel and the chemical features of larger methyl-esters. Although MB does not have the high molecular weight of a biodiesel fuel, it has the essential chemical structural features, namely the methyl ester moiety, as well as the alkyl chain [12,36].

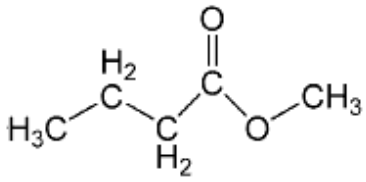

Figure 1-3: Methyl Butanoate Chemical Structure.

In 2000, Fisher et al. published a kinetic model for methyl butanoate, forming a basis for future development by other groups such as Gail et al, Dooley et al, and Huynh et al [37]**.** The mechanism uses a smaller *n*-propyl (C3H7) group to simulate the C16-C18 portion of the usual biodiesel molecule, and was developed using experimental data from low temperature oxidation in a small, constant-volume isothermal static reactor in the temperature range of 520 K to 740 K and pressure range of 13 kPa to 54 kPa. Gail et al modified and validated the mechanism with experiments performed with a jet stirred reactor and opposed diffusion flame at atmospheric pressure, and variable pressure flow reactor at high pressure (1.266 MPa) [38]. Low reactivity was observed in the range of 850 K to 1050 K in the experiment, but was not predicted in the model. Otherwise the experimental and simulation results were in good agreement. It was concluded that MB may not be an ideal biodiesel surrogate for compression ignition studies (because of its low Cetane Number), but may be useful for a better understanding of the methyl ester features on soot and NO_x formation.

Dooley et al. developed a modified mechanism to agree with shock tube and rapid compression machine (RCM) experiments [39]. Shock tube experiments were performed at 1 to 4 atm over a temperature range of 1250-1750 K and at equivalence ratios varying from 0.25 up to 1.5. The focus of this study was the behavior of autoignition of MB, which appeared to follow Arrhenius-like temperature dependence. The model was found to correctly simulate the effects

in the shock tube experiments; however, comparisons against the RCM ignition delay data were less accurate. The results did not exhibit the negative temperature coefficient (NTC) behavior seen previously in [31]. The model was used to predict species concentrations of various components, and good agreement was found with results from previous experiments.

Huynh et al. took a more theoretical approach and improved on the accuracy of important steps and rates presented in the kinetic mechanism. The model was combined with that of Fisher et al. [37] and was used to study CO_2 formation during the pyrolysis of MB and predict ignition delay times in shock tube experiments at different temperatures and pressures [40]. The computational results were found to be in good agreement with the experimental results.

In 2011 Feng [17] incorporated a NO_x sub-kinetic model into the modified MB mechanism of Huynh et al and verified it with ambient pressure premixed (counterflow of nitrogen and fuel/air streams) and non-premixed (counterflow of oxygen and fuel/N_2 streams) opposed jet flames of four different methyl ester fuels, including methyl formate, methyl acetate, methyl propionate, and methyl butanoate. Samples were taken with quartz microprobes and NO_x emissions were analyzed with a Chemiluminescence NO-NO_2- NO_x Analyzer. In the premixed flames, the ester compounds exhibited lower concentrations of NO_x than n-alkanes of similar size over an equivalence ratio range of 0.8-1.2. The MB NO_x formation was compared with n-butane. The MB was found to have a larger contribution of prompt NO_x. The model was considered in good qualitative agreement with the data.

Egolfopoulos [34] reviewed the many experiments that had been done in the advancement of a methyl butanoate mechanism. His own experiments included gas sampling and NO_x quantification in atmospheric premixed counter flow flames (φ = 0.8, 1.0, 1.2) with a quartz water-cooled microprobe. The disturbance to the flame was considered minimal. The sample

was analyzed with a Chemiluminescence NO-NO_2- NO_x Analyzer, with a lower detectability limit of 0.5 parts per million (ppm). The results of the MB-air flame were compared with n-pentane-air NO_x emissions. For all three equivalence ratios, the MB was found to have lower concentrations of NO_x at various locations above the burner surface.

1.4 Low-Pressure, Laminar Premixed Flat Flames

Laboratory flames are generally considered premixed or non-premixed. This definition is dependent on the mixing state of the fuel and oxidizer. In non-premixed flames, the fuel and oxidizer are initially unmixed and combustion occurs at the interface where the fuel and oxidizer meet. Conversely, in premixed flames, the fuel and oxidizer are mixed before the flame front. The flame speed of premixed flames is governed by the overall reaction rate and molecular diffusivity of the unburned mixture. For non-premixed flames, the diffusion rates are the main determinant in the burning process.

Flames can also be characterized as turbulent or laminar. With turbulent flames, complications arise due to a strong interaction between the diffusion/mixing processes and chemical reactions, making this type of flame difficult to develop accurate computational models. Therefore, laminar flames are much more popular in combustion studies such as the work described herein as well as the earlier studies performed by Fenimore to characterize prompt NOx [22] as well as the more recent studies by Sutton [28], Williams and Fleming [29], Feng [17] and Egolfopoulos [34].

A flat flame burner, also known as a McKenna burner, is utilized in the present study. The flat flame is often used in laboratory experiments due to its simple geometric nature and good stability. The flame is considered to be approximately one dimensional, and changes in

temperature and species mole fractions occur only in the axial direction, making it a relatively simple to compare experimental results against computational models with detailed chemical kinetics.

Experiments are often performed at low pressure because of the effect of pressure on the thickness of the flame. The rate of the chemical processes in a flame depends on the concentration of molecules present, which is roughly proportional to the total pressure [41]. An increase in pressure accelerates the chemical processes and the flame thickness narrows. Consequently, at low pressure the chemical processes slow and the flame thickness expands. For example, at atmospheric pressure, the typical flame thickness is on the order of 1 mm, whereas, if the pressure is reduced to the range of 10 to 100 torr, the reaction zone can widen to approximately 3 to 10 mm. This increased flame thickness allows for good spatial resolution of the flame, and thus, a more comprehensive analysis of the processes and formations occurring in the flame.

In a flat flame burner, the fuel and oxidizer are delivered to a chamber in the bottom of the burner where they can premix. These reactants subsequently flow through a porous sintered bronze plate at the top of the burner and into the reaction zone of the flame. The surface of the burner is water cooled, causing the flame to stabilize above the surface of the burner. The mechanism of stabilization is related to the increase of flame heat losses when the flame front nears the cooled burner surface. The flame velocity decreases as the flame moves closer to the burner due to the increase in cooling of the gas, until it stabilizes at the distance where the gas flow and flame velocity are equal [41].

The premixed, laminar flat flame is composed of three regions: the preheat zone, reaction zone, and post flame zone. The preheat zone is the region between the burner surface and the

reaction zone. This region is where the temperature and species gradients are the largest. As the gas mixture approaches the flame front, conduction from the reaction zone heats the mixture. Mass transport processes play a large role in the mole fraction profiles in this area. An example of this effect occurs when intermediate species from the reaction zone diffuse toward the burner surface and dilute the incoming gases. The reaction zone is the thin region where the temperatures are hot enough for the main reactions that convert the fuel and oxidizer into products to take place. This region is also the most luminous portion of the flame. The post flame zone occurs after the reaction zone, and is where reactions slow down, temperature begins to decline, radicals are consumed and CO is converted to CO_2.

1.5 Thesis Outline

The scope of this work involves low pressure flat flame sampling for analysis of nitric oxide formation in fatty acid methyl ester and alkane fuels. Specifically, the small biodiesel surrogate, methyl butanoate, was combusted in air at low pressures and compared against similar experiments conducted with propane. Chapter 2 presents the experimental setup and methods applied in the research study. Chapter 3 introduces the numerical modeling approaches used and for comparison with and interpretation of the experimental results. Chapter 4 presents the experimental and modeling results and a comparison of the methyl butanoate and propane flame results. In the final chapter, conclusions regarding the present work are summarized and future work is recommended for studies that might be conducted to gain a better understanding of the NO_x formation in methyl ester and alkane flames.

2. Experimental Techniques

This chapter details the materials and methods used in the low pressure flat flame experiments which are the focus of this study. The first section details the apparatus used in sampling of low pressure flat flames including the burner, sampling system, thermocouples, fuel vaporization, and the Fourier transform infrared (FTIR) spectrometer. The second section discusses the materials used in the experiments. Finally, the third section presents the methods for analysis of species and temperature sampling, and quantitative measurements of nitric oxide concentrations with FTIR spectroscopy.

2.1 Experimental Setup

This section will present details about the facility used in this work for low pressure flat flame sampling.

2.1.1 **Flat Flame Burner Apparatus and Sampling System**

The experiments were conducted at low pressure with steady, laminar, premixed flames stabilized on a flat flame burner, also known as a McKenna burner. Lean, stoichiometric, and rich propane-air and methyl butanoate-air flames were studied. The flat flame burner utilized in this experiment was 6 cm in diameter, and manufactured by Holthuis and Associates (Sebastopol, CA). A diagram of the burner is shown in figure 2-1. The premixed reactants enter a plenum from the bottom of the chamber and flow upward through a sintered bronze plate. The reactants flow through a region that is approximately 6 cm in diameter, and is surrounded by a 1.33 cm ring from which a shroud gas flows. The shroud gas is used to act as a barrier from outside effects on the flame, although at vacuum, these effects are minimal.

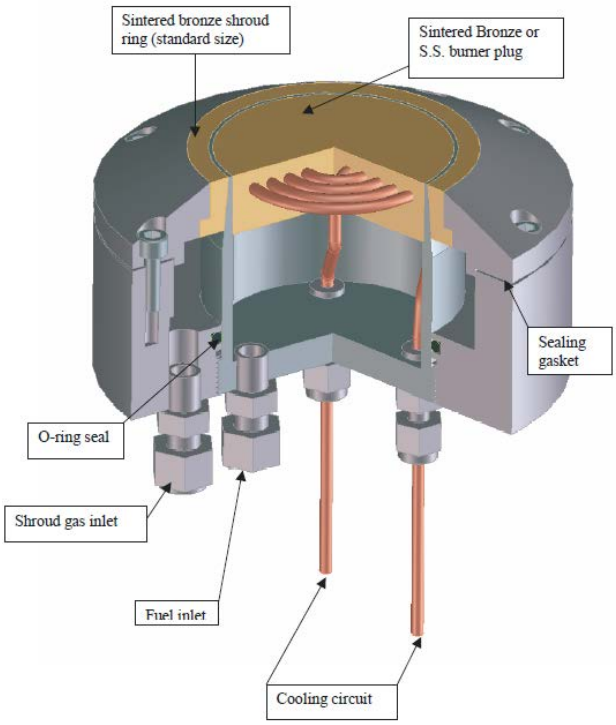

Figure 2-1: Flat flame burner [42].

The two primary fuels used in this experiment were methyl butanoate and propane. Methyl butanoate, a liquid at room temperature, had to be vaporized before being sent to the burner. The fuel vaporization apparatus is discussed in section 2.1.3. Propane (C_3H_8) is gaseous at room temperature and does not have to undergo the vaporization process. Propane was delivered from a liquid propane compressed tank and flow was controlled with a mass flow meter (Omega Engineering, Inc. – Stamford, CT - Model FMA1720), calibrated for propane use by the manufacturer. Air was delivered from a compressed gas bottle then delivered to a regulator. Downstream of the regulator, pressure was measured with a pressure transducer (Senstronics Storm ST00223). After exiting the regulator, the air was sent through a precision choked flow orifice (O'Keefe Controls – Monroe, CT); calibration for the flow through the

orifice was performed using a Bios Defender 510 primary flow calibrator (Bios International Corporation – Butler, NJ).

A cooling coil positioned in the sintered bronze enabled water to circulate through the burner and cool the burner surface. At the surface of the burner, the water removed heat from the flame, causing the flame to stabilize off of the burner surface as discussed in section 1.5. A low-flow miniature gear pump was used to circulate water through the cooling coil during experiments. The water traveled from the pump to a rotameter (Omega Engineering, Inc. – Stamford, CT – Model FL-2504-V), which was used to measure and control the flow, and then entered the channel in the burner. For the propane flames, water was circulated at a rate of 100 mL/min. For the MB flames, water was circulated at a lower rate of 25 mL/min, to avoid condensation of the vaporized fuel inside of the burner.

Measurements at different heights were obtained by moving the burner relative to the sampling probe or thermocouple. The burner was mounted on a motorized linear motion stage (VELMEX, Inc. – Bloomfield, NY - model BiSlide series), controlled by a programmable stepper motor. The device allowed for vertical movement with steps of 0.005 mm, with a range of 127 mm. The repeatability of the device returning to its initial position was +/-2 μm.

The burner was housed inside of a stainless steel vacuum chamber with various flanges and feedthroughs constructed specifically for this experiment. Feedthroughs were manufactured to accommodate the fluid and gas inputs/outputs of the burner as well as for temperature measurements, sample extraction, and power and control lines for the translation stage. A photo of the chamber can be seen in figure 2-2.

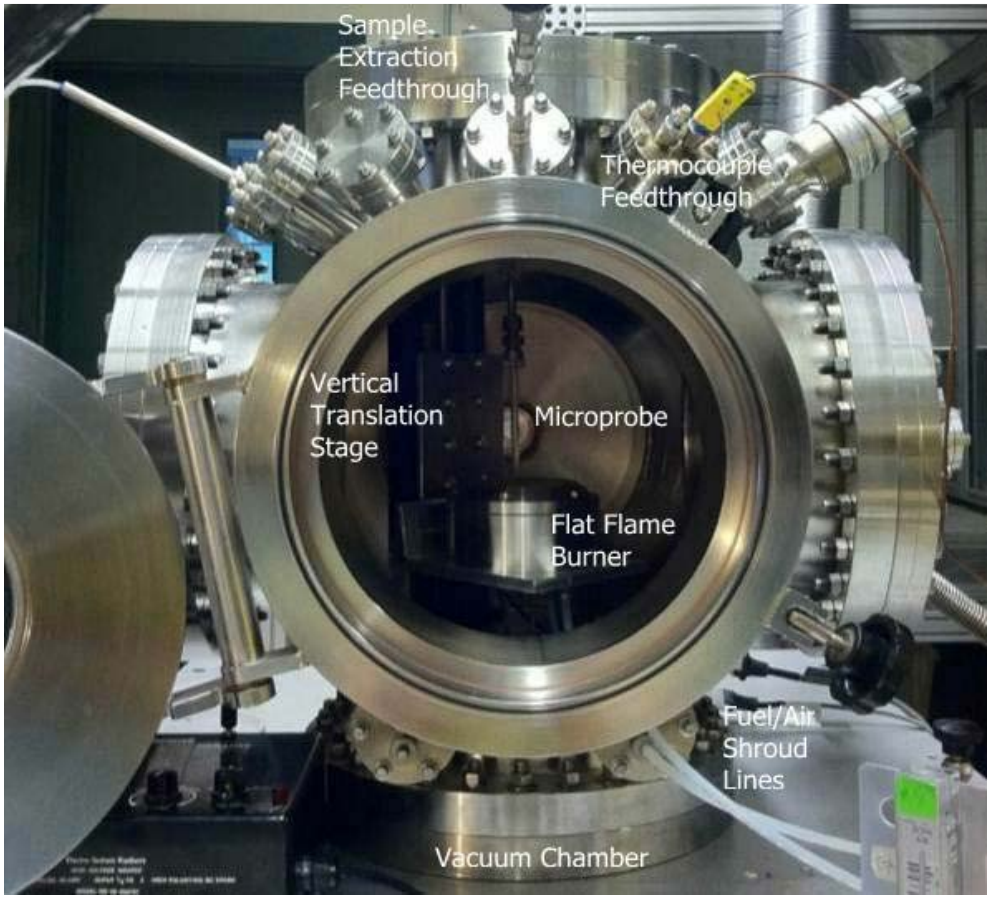

Figure 2-2: Vacuum Chamber.

Vacuum chamber pressure was measured near the exhaust line of the vacuum chamber with a capacitance manometer pressure gauge (MKS Instruments – Andover, MA – Model 722A) The pressure was maintained by a rotary vane vacuum pump (Edwards – Model E2M30) located downstream of the exhaust line on the chamber, and was adjusted with a manually actuated bellows sealed valve. Further refinement of the pressure was achieved with a separate, smaller, stainless steel bellows valve, situated in the exhaust line and open to the atmospheric surroundings. A molecular sieve foreline trap was also located in the exhaust line to extract

excess water out of the exhaust before reaching the vacuum pump. The molecular sieve also helped to prevent any oil originating from the pump to reach the vacuum chamber.

Species samples were extracted from the flame using a quartz microprobe without a cooling water jacket. The probe was approximately 350 mm in length and was constructed with 6.0 mm OD, 3.8 mm ID quartz glass tubing tapering to an orifice diameter between 47 and 250 μm. All sample data presented was extracted with a 47 μm diameter orifice probe. The probe was mounted in a horizontal orientation in the chamber and connected by a Swagelok ultratorr fitting to a stainless steel tube where the sample was carried through and out of the vacuum chamber to a heated sample line.

Figure 2-3: Quartz Microprobe used in experimentation, orifice diameter 47 μm.

In earlier experiments, the gas samples were extracted at a pressure of 20 torr by a pump situated downstream of the FTIR gas cell, and would flow directly out of the vacuum chamber and into the evacuated gas cell. However, the resolution of the FTIR at this low pressure is substantially reduced, and the ability to detect species, especially in relatively small quantities was found to be exceedingly difficult. Accordingly, to increase the pressure of the sample flowing to the gas cell, the gas sample system was redesigned to incorporate a dry scroll vacuum pump (Edwards – Model XDS 35i) to deliver the gas sample to the FTIR at a higher pressure.

The scroll pump was chosen due to its ability to deliver a clean sample to the FTIR. The pressure in the sampling system was controlled with a bellows valve upstream of the vacuum pump. The pressure downstream of the probe was kept at 6 +/-1 torr in order to guarantee choked flow through the probe orifice. Choked flow is necessary to quench the products of combustion before the sample is sent to the FTIR. This technique has been widely discussed and performed by many researchers and will be discussed in more detail in section 2.1.4.

After exiting the exhaust of the scroll pump, the gas samples were sent through another heated sample line and into the evacuated FTIR gas cell. The gas cell was filled to the desired analysis pressure and an infrared spectrum of each gas sample was taken. A more detailed description of the FTIR and the software used in analysis are presented in section 2.1.4. Following analysis and before taking each subsequent sample, the gas cell was evacuated with a third vacuum pump, which was a rotary vane oil sealed pump (Leybold – Model Trivac D4A – Germany).

Figure 2-4 is a photograph showing an example of the extraction of gas samples from a lean, low pressure flat flame. A thermocouple is situated to the left of the microprobe to determine that the temperature in the flame remains steady during sampling. The thermocouple design is presented in the following section on physical probe temperature measurements. Figure 2-5 is a photograph of the sample lines exiting the vacuum chamber and flowing into the scroll vacuum pump for delivery to the FTIR. A schematic diagram of the overall gas sample system is included in Figure 2-6.

Figure 2-4: Lean (φ=0.8), low pressure (P=100 torr), methyl butanoate-air flat flame with simultaneous use of sample probe and thermocouple.

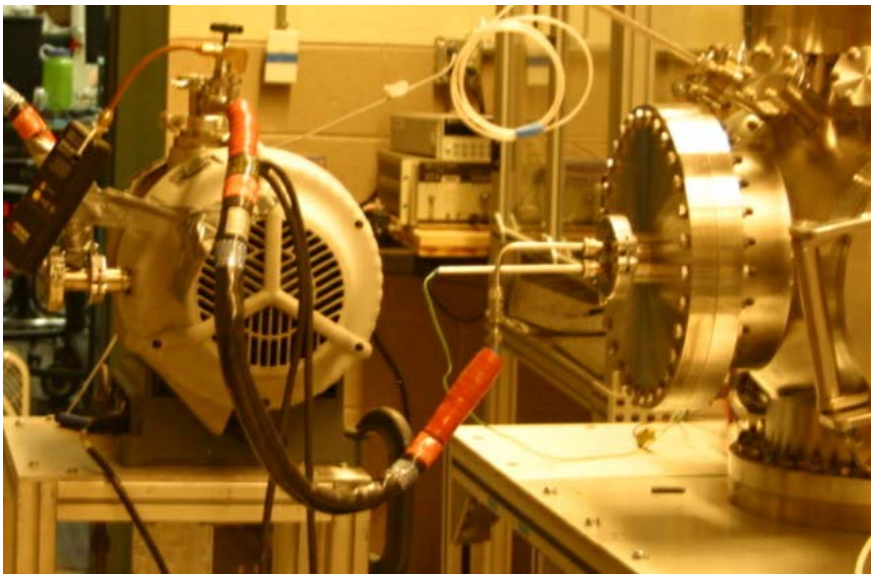

Figure 2-5: Sample lines exiting the vacuum chamber and flowing into the scroll pump for transfer to the FTIR.

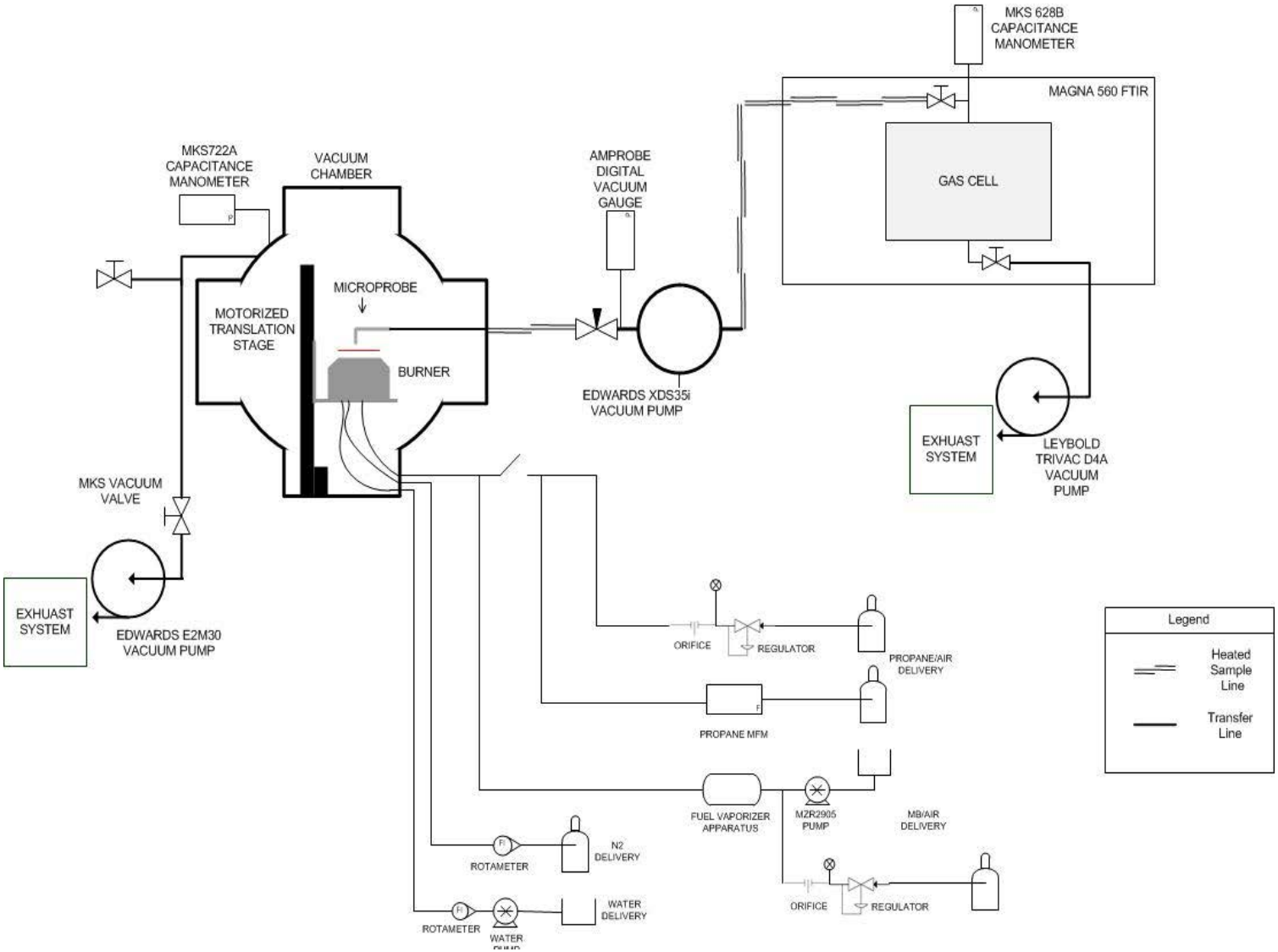

Figure 2-6: Schematic of experimental Setup.

2.1.2 **Temperature Measurements**

Direct temperature measurements were performed using a coated type R, Pt/Pt-13%Rh, thermocouple (Omega Engineering, Inc. – Stamford, CT – Model P13R-005). The measurements were corrected for radiation effects as discussed in section 2.3.3. The platinum-rhodium thermocouple was chosen due to its performance at the high temperatures seen in flame experiments. The physical thermocouple disturbance of the flame was minimized by selecting wire small enough to eliminate substantial effects. The bare wire used in the experiments had a wire diameter of 0.125 mm and a bead diameter of 0.395 mm. A photo illustrating the thermocouple engulfed in a low pressure propane flame is shown in figure 2-7.

The thermocouple design used in the experiments consisted of the two wire leads housed within a 1.2 mm diameter twin bore ceramic cylinder, which was housed within a4 mm O.D. quartz tubing for support. The ceramic and quartz were chosen because of manufacturer recommendations to avoid platinum wire contact with metal. A short section of the wires of approximately 7 mm in length, as well as the thermocouple bead remained exposed at one end of the probe. The leads and bead were shaped into a flat semicircular form. This design was based on that described in Ref. [43]. A diagram of the thermocouple design and photograph are shown in figures 2-7 and 2-8, respectively.

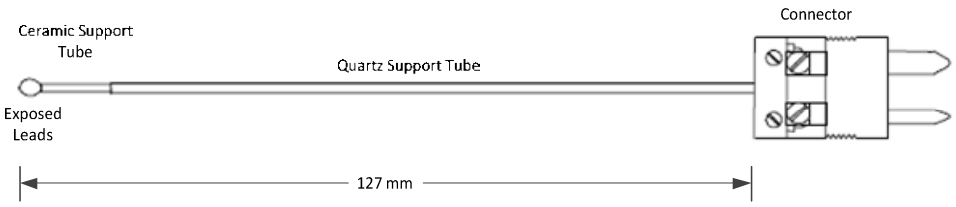

Figure 2-7: Thermocouple probe design.

To reduce the catalytic surface effects known to occur with platinum based thermocouples, a ceramic coating was applied. Catalytic reactions are known to produce inaccuracies in platinum-based thermocouples temperature readings. Alumina ceramic based Aremco Ceramabond 569 was chosen based on its performance described in the previous literature [43,44]. The Ceramabond ceramic coating is a fairly viscous mixture. However, a thin coating was applied using a fine tipped brush. The coating caused the wire diameter and bead diameter to increase to 0.30 mm, and 0.45 mm, respectively. The advantages to this coating are as follows: 1) it is non-toxic, unlike the typical beryllium-yttrium oxide coatings that are very common, 2) it adheres well to metals, and 3) it has a useful temperature range up to 1900 K. The coating also proved to be fairly resilient, having lasted through many hours of testing.

In addition to flame temperature measurements, the wall temperature of one of the inner surfaces of the chamber was measured throughout temperature sampling and used the thermocouple radiation corrections presented in section 2.3.3.3. These measurements were performed using a type K thermocouple with adhesive backing (Omega Engineering, Inc. – Model SA1-K-SC).

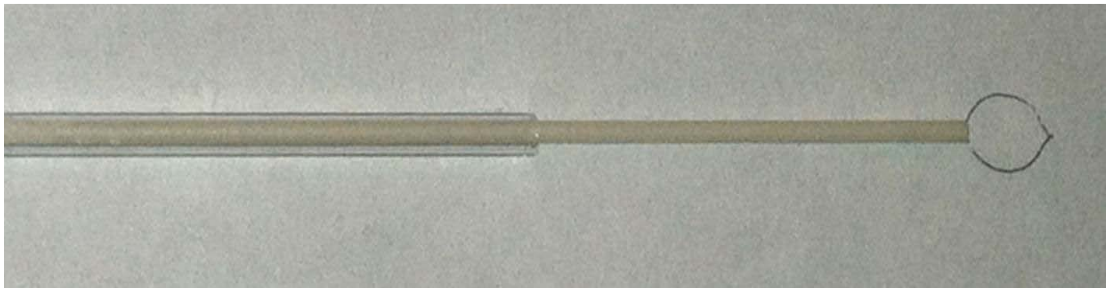

Figure 2-8: Uncoated thermocouple probe.

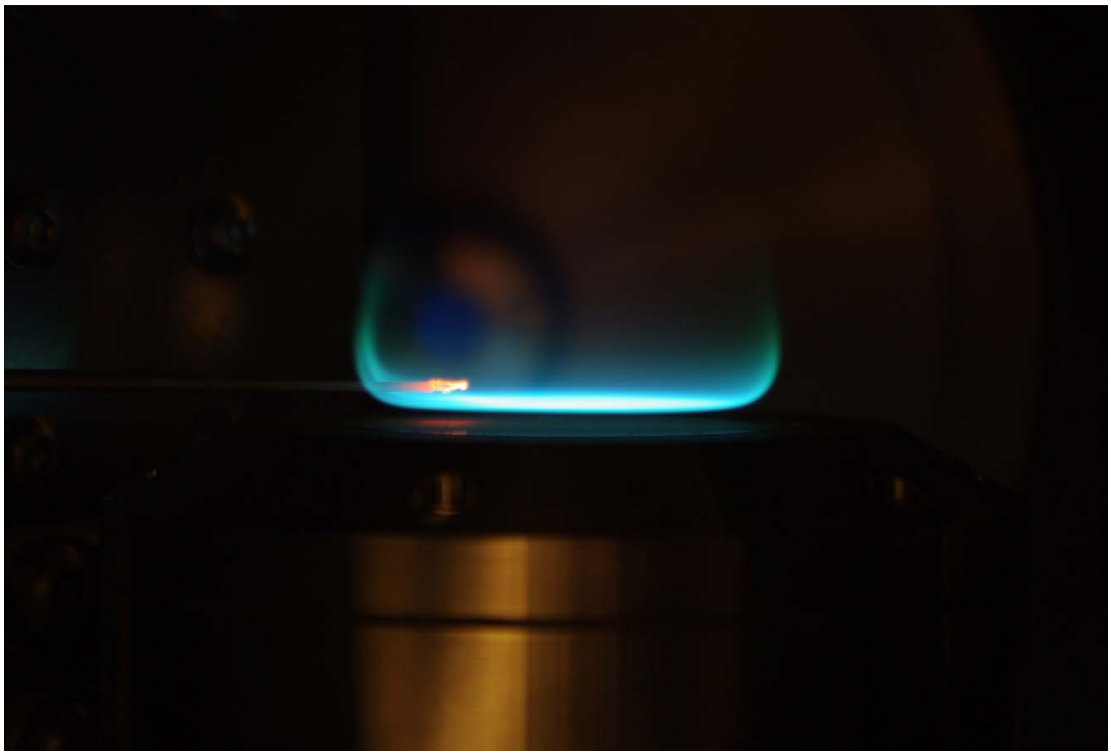

Figure 2-9: Photo illustrating a low pressure (P=100 torr) rich (φ=1.2) propane-air flat flame with Pt/Pt-13%Rh thermocouple probe in process of obtaining temperature measurements.

2.1.3 **Fuel Delivery and Vaporization**

The reactant stream that is fed through the burner consists of a mixture of the fuel and air. The physical properties of the two fuels used in these experiments are listed in Table 2-1. Here it can be seen that propane is in its gaseous form at room temperature, whereas methyl butanoate is a

liquid. The propane is stored in a compressed gas bottle in liquid form, but exits to the burner in its gaseous form. The fuels must be gaseous to premix with the air before being combusted. Therefore, it is necessary for the methyl butanoate fuel to undergo the vaporization process.

Table 2-1: Fuel Properties.

Fuel	Molecular Weight (g/mol)	Phase at STP	Boiling Point at 1 atm (°C)
Methyl Butanoate	102.13	Liquid	102
Propane	44.1	Gas	-42

A schematic of the fuel vaporization apparatus is shown in figure 2-10. A MZR2905 microannular gear pump (HNP Mikosysteme GmbH- Germany) was used to supply a known volume of fuel to the stream entering the vaporization chamber; for each revolution, 3 μl of fuel is displaced. The equivalence ratios of the propane flames were calculated using the flow rates of the air and fuel set by the user and the feedback from the mass flow meter and pressure gauge. For methyl butanoate, the pump speed set point determined the fuel equivalence ratio. The pump speed was controlled with a LabVIEW virtual instrument (VI). Using the VI, the user prescribed the desired equivalence ratio, and set a value for the volumetric flow rate of air. The mass flow rates of the fuel and air were calculated and used to set the speed of the pump (in revolutions per minute) to achieve the equivalence ratio set point. The user was also required to input the molecular weight (g/mol), density (kg/m3), and stoichiometric combustion coefficient for the fuel being used.

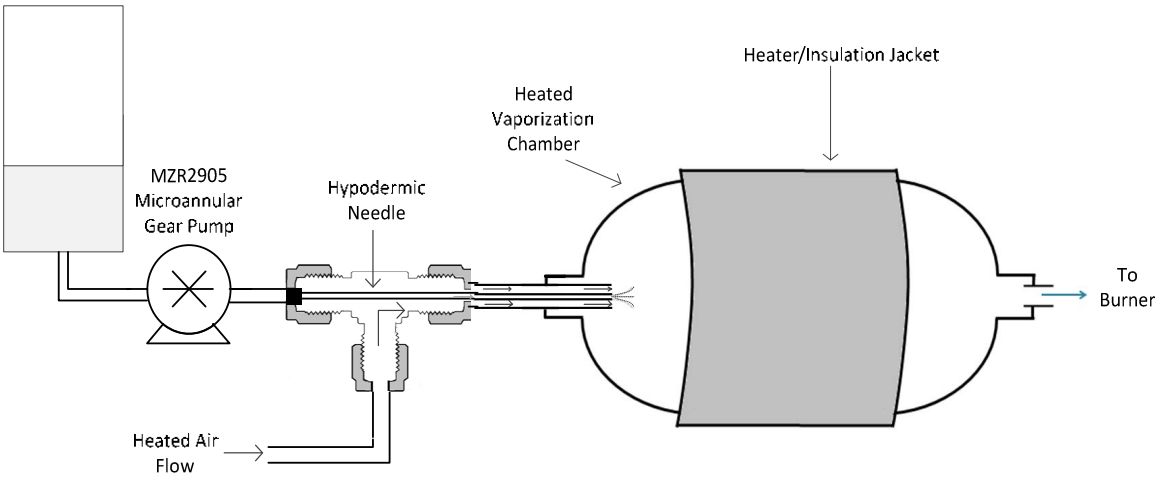

Figure 2-10: Schematic of Fuel Vaporization System (not to scale).

The fuel traveled from the pump through 1.5875 mm (1/16th inch) stainless steel tubing to a 3 inch long 22 gauge hypodermic needle. The beveled tip of the needle was removed to prevent the needle from fouling, which was proven to be very effective. The needle was situated inside of a tee followed by 25 mm of 1.5875 mm diameter tubing, where heated air at 175°C (448 K) was flown around the outside of the needle. The tip of the needle and end of the piece of tubing were very nearly flush with one another.

As the fuel exited the needle, the air flow along the outer surface of the needle exited at a velocity high enough to shear off the individual droplets and turn them into a fine fuel spray. This technique allows for faster vaporization of the fuel once inside of the vaporization chamber, also heated to 175°C. Downstream of the vaporization chamber, a needle valve was used to increase the residence time of the mixture in the chamber, which created a more even, steady flow entering the burner. To prevent fuel condensation, the lines carrying the mixture of fuel and air to the vacuum chamber, as well as the burner itself, and the nitrogen shroud flow were heated to a temperature of 175°C.

Various difficulties arose in implementation of the fuel vaporization system. The setup began with only heated air lines and vaporization chambers, which proved to create a problem with condensation. In this initial configuration, condensation of the fuel occurred in the delivery lines, and on the cooler walls of the burner, thereby creating an unacceptable level of variability in the fuel equivalence ratio. The condensation caused the equivalence ratio to fluctuate rapidly from fuel rich to fuel lean. The effect was very visible, causing the luminous portion of the flame to go from a bright green (rich) to an almost purple color (lean). The condensation also led to large instabilities in the flame, making it difficult to produce a low pressure flame for long enough periods to conduct any gas sampling.

Heaters were added to the delivery lines and around the body of the burner, making the condensation effect less problematic. However, the flame stability was still unacceptable. Many other alterations were made to the vaporizer to try to negate this effect and the most effective change involved incorporating a needle valve downstream of the vaporization chamber to increase the residence time in the chamber and ensure that all fuel was in vapor form and flowing at a more consistent rate into the chamber. The flame would drift to a lower equivalence ratio over time, and the valve had to be adjusted to maintain the same characteristics throughout experimentation. The downside to the final alteration was that it was nearly impossible to obtain a completely accurate equivalence ratio for the flames. Due to time constraints and lack of sufficient equipment, the equivalence ratio was obtained by visual inspection and simultaneous temperature measurements in the flame. The thermocouple probe was introduced to the flame below the microprobe and out of the flow from which the microprobe was sampling. Much effort was made to ensure that the temperatures were held constant at the various locations during sampling. It is believed that the accuracy of the equivalence ratio is known to within +/- 0.1.

Recommendations on how to improve the vaporization apparatus are provided in the future work section of this report in chapter 5.

2.1.4 **Fourier Transform Infrared Spectrometer**

FTIR spectrometry has been shown to be a quick and precise measurement technique for quantitative species concentration measurement. The FTIR spectrometer used to identify and quantify species in the present study was a Thermo Nicolet Magna-IR 560 equipped with a 2 m gas cell and liquid nitrogen cooled MCT-A detector with ZnSe windows. Gas samples were analyzed using Nicolet's OMNIC QuantSetup/QuantPad software.

Measurements were obtained in the spectral range of 500 to 4000 cm^{-1}. The resolution was set to 0.5 cm^{-1} and the signal gain was set to 1. The gas samples were analyzed in a 200 mL volume gas cell, with a 2 m pathlength. All calibration spectra and sample spectra were analyzed at a pressure of 550 torr, temperature of 121.1 °C. For each gas and calibration sample, 256 scans were taken.

The principles of FTIR spectroscopy incorporated into the Nicolet Magna IR- 560 spectrometer are described herein. The optical bench consists of an infrared radiation source (broadband light source), interferometer, and several optical mirrors. The source emits the infrared radiation across a range of frequencies, this light is deflected off of a mirror and directed into and interferometer where the beam is split into two optical beams. The first beam reflects off of a fixed, flat mirror and returns to the interferometer to merge with the second beam. Meanwhile, the second beam reflects off of a flat, movable mirror which oscillates back and forth, then is reflected back to the beamsplitter to merge with the first beam. The recombined beam then passes through the sample compartment. When the interference between the two

beams of light is observed by the detector, the resulting signal is an interferogram. The interferogram is generated by recording the amount of radiation going to the detector over a period of time. To convert the signal into a spectrum, the computer software applies a Fourier transform to the interferogram. The sample is placed in the beam path and the chemical makeup can be determined from the frequencies at which the infrared radiation is absorbed.

When the beam passes through the sample, the infrared radiation causes vibrational and rotational excitation of the molecular bonds in the material. Intensities of vibrations increase when infrared radiation is absorbed. Radiation is absorbed by a molecule only if the frequency of the radiation provides energy in the precise amount required by one of the bonds in the molecule. Strong molecular vibrations absorb more energy, producing larger peaks in the resulting spectrum. A single molecule may have peaks that show up in multiple locations in the spectrum, depending on the number of ways that the molecule can move.

In the present work, the infrared spectra of combustion gases were analyzed. There are various factors that affect the ability of a FTIR to detect certain species of gases. In a given volume of gas, there are less absorbing molecules than in a more condensed phase sample (i.e. liquids, solids), so a greater sample thickness is required to record the infrared spectrum. Long path gas cells provide this ability, and typically range anywhere from 10 cm to several hundred meters in length [45]. Low pressures also affect the ability of the FTIR to detect absorbing molecules, due to the fact that at lower pressures there are fewer molecules present, and the chances for interaction are low. Therefore, analysis must be performed near atmospheric pressure. Attempts were made in the present experiment to try to analyze pure gas components at approximately 20 torr, with concentrations as low as 50 ppm. In these trials the signal

intensity was so low that the peaks produced by the samples were indistinguishable from the noise produced in the spectrum.

It is important in FTIR spectroscopy to get the best signal-to-noise ratio possible, particularly when measuring gases that exist in small quantities in the sample. This factor is controllable by specifying the number of scans that the instrument takes of the sample. When the instrument performs multiple scans it uses a technique called “signal averaging”. The scans are added together and their average is found to produce a spectrum. This method improves sensitivity and, in general, increases the signal-to-noise ratio. Increasing the number of scans increases the time it takes to analyze each sample. However, the instrument performs the analysis fairly fast (approximately 1 second per scan).

Resolution is another user controlled parameter that can increase the accuracy of the resulting spectrum. Resolution refers to the minimum distance between two sequential peaks and determines how close two peaks can be to one another and still be identified as individual peaks in the spectrum. Gases tend to produce narrower bands in the infrared spectra than solids or liquids. So, ideally, the resolution needs to be set to a higher value.

Composition analysis by absorption spectroscopy is based on three premises. First, the components of the mixture must absorb light in the range of frequencies measurable by the instrument. This is satisfied for all but elemental substances in the infrared region, and the amount of absorption varies between species. Second, each component in a mixture has a different amount of light absorbed as a function of frequency or wavelength. Finally, the amount of light absorbed for a given species increases with concentration, as expressed as Beer’s Law:

$$A = \varepsilon b C \qquad (2.1)$$

where A is the absorbance which is derived from the transmittance, T of the sample:

$$A = -\log T \qquad (2.2)$$

ε the molar absorptivity/extinction coefficient, which is dependent on the particular component and frequency of light, b the path length, and C is concentration of the substance [46]. For some species, equation 2.1 fails at higher concentrations, becoming a nonlinear function of concentration. Corrections for this sort of deviation are discussed in section 2.3.2.1.

2.2 Experimental Materials

Chemicals used as reactants were as follows: C_3H_8 (100%), breathing air (76.5-80.5% N_2, 19.5-23.5% O_2) purchased from Airgas, Inc. and used in the experiments as is. Methyl butanoate was purchased from several different suppliers due to its limited availability in the quantities needed for the experiments. A >98.0% grade solution was purchased from all suppliers which included Sigma Aldrich, Alfa Aesar, and TCI America. The N_2 shroud gas used in the experiments was supplied by the house nitrogen tank, also purchased from Airgas, Inc.

Various gases were used to prepare standard calibration curves for FTIR quantitative analysis and to check the validity of their spectra. The following gases from Scott Specialty Gas were used: NO (50.2 ppm-balance N_2), CO_2 (12% CO_2-balance N_2, 8% CO_2-balance N_2, 4% CO_2-balance N_2), CO (10,000 ppm-balance N_2, 1204 ppm-balance N_2, 250 ppm CO-balance N_2), C_3H_8 (30.70 ppm C_3H_8-balance N_2), CH_4 (2508 ppm CH_4-balance N_2, 251 ppm CH_4–balance N_2). Distilled water produced at the lab was used in calibration for H_2O.

2.3 Experimental Methods

This section describes the procedures used in collecting samples and temperature data, as well as the various flame conditions used in the experiments. The method for how different species were analyzed and quantified is also discussed.

2.3.1 **Burner and FTIR**

Experiments involved comparing the species profiles obtained from both methyl butanoate-air and propane-air flames for lean, stoichiometric and rich conditions. The equivalence ratios selected were 0.8, 1.0, and 1.2. The experimental conditions were chosen to produce a stable flat flame at vacuum pressure. The air flow rates were selected such that a stable flat flame was achieved for each of the equivalence ratios. The propane experiments had reactants entering the burner at ambient temperature (300 K), while the methyl butanoate flame reactants entered the burner at a temperature of 448 K, due to the need to keep the fuel vaporized. Ideally, the inlet temperatures of the mixtures should have been held at the same temperature and varied in order to keep the flame temperatures constant for each stoichiometry for both the methyl butanoate and propane flames. However, due to time constraints, results were not obtained for these conditions and it is recommended they be performed as future work for further research in Chapter 5. The flame conditions for methyl butanoate are presented in table 2-2 and propane in table 2-3. The air flow rates were kept constant for the different flame stoichiometries.

Table 2-2: Methyl Butanoate Flame Conditions.

Equivalence Ratio	Air Flow Rate (sLPM)	Fuel Mass Flow Rate (kg/s)	Pressure (torr)	Initial Gas Temperature (K)
0.8	6.0	$0.9(10^{-5})$	100	448
1.0	6.0	$1.1(10^{-5})$	100	448
1.2	6.0	$1.3(10^{-5})$	100	448

Table 2-3: Propane Flame Conditions.

Equivalence Ratio	Air Flow Rate (sLPM)	Fuel Mass Flow Rate (kg/s)	Pressure (torr)	Initial Gas Temperature (K)
0.8	5.6	$4.67(10^{-6})$	100	300
1.0	5.6	$5.85(10^{-6})$	100	300
1.2	5.6	$7.075(10^{-6})$	100	300

Flame ignition was performed using a generic disposable lighter. The various flames were ignited at atmospheric pressure for conditions differing from those used in the experimentation. At atmospheric conditions, the flames require a higher flow rate of air and fuel due to the slower flame speed than that of a flame at a vacuum pressure of 100 torr. Although the initial conditions vary, the conditions used for starting were relatively stable, making it easier to keep the flame burning while pulling the chamber down to vacuum. For propane, the flame was started with an air flow rate of 14 liters per minute (LPM) or more, and an equivalence ratio near 1.0. The methyl butanoate flame initial conditions were an air flow rate near 10 LPM and a stoichiometry of 1.0.

A thermocouple was placed at the outer edge of the flame during sampling to observe when the flame was stable. Stabilization was achieved when the temperature became a nearly steady value.

To determine the zero height of the probes, the burner was slowly raised to the very tip of the probe so as not to damage it. The burner was lowered on the linear translation stage to achieve the various sampling heights used in the experiments.

After each flame was ignited, the vacuum chamber was sealed by closing the access door and then pulled down to the sampling pressure of 100 torr. The flow rates of air and fuel had to be adjusted very carefully to the sampling conditions as the pressure was lowered to avoid flame extinction. The flame was allowed to stabilize and then sampling could be performed.

The FTIR had to undergo several preparations before allowing the sample to flow into and fill the cell. The gas cell and optical bench have N_2 purges running continuously to avoid any residue or condensation build up on the optics. The N_2 gas is delivered from a dewar and lines running throughout the laboratory. First, the N_2 purge that flows through the optical bench was increased to 30 SCFH for the duration of the sampling period, and the gas cell purge was increased by further opening the valve located in the N_2 line. Then, the liquid N_2 used to cool the detector was dispensed into the cooling chamber of the optical bench. The detector had to cool for approximately 30 minutes before the FTIR could be used. Heaters located at the entrance to the gas cell, and the gas cell heater were activated and allowed to reach the sampling temperature of 121.1 °C (250 °F).

After approximately 20 minutes, the gas cell purge was switched over to ultra high purity (UHP) N_2, delivered from a compressed gas bottle. The gas cell was closed off from atmospheric pressure, and the vacuum pump for evacuating the gas cell was then turned on and allowed to pull the purge through the gas cell. The pressure in the gas cell was metered with two needle valves located on the entry port and exit port of the cell, respectively. After running the

UHP purge for 30 minutes at near atmospheric pressure, the pressure was decreased to the sampling pressure of 550 torr.

The sampling pressure in the gas cell was selected due to the reduced sensitivity of the FTIR to quantify low concentration species. Scans of a combustion gas sample were taken at pressures ranging from 20 torr up to atmospheric pressure. After approximately 350 torr, the FTIR shows much less sensitivity and is able to closely quantify the actual concentration levels. In order to try to eliminate these problems as well as shorten the sampling time, the sampling pressure was chosen to be 550 torr.

The optical bench was aligned before use each day. Then, a background scan was taken at the sampling pressure and temperature. The background scan was necessary for accurate quantification of species since it provides a baseline of what the empty gas cell spectrum looks like before taking a species sample. The FTIR was set to a resolution of 0.5 cm^{-1} and a gain of 1.0 for all analysis. The number of background scans performed was set to 256, so as to reduce the signal to noise ratio as much as possible. Once a background scan was performed, the combustion gas sample could be introduced into the gas cell.

The combustion gas samples were withdrawn from the flame at the various sample heights with a downstream pressure in the probe of 6 +/- 0.5 torr, created by the dry scroll vacuum pump. The probe used in all sampling had a 47 μm diameter orifice. The pressure downstream of the orifice was maintained at a pressure low enough to prevent water condensation as well as guarantee choked flow at the probe orifice. The sample exited the vacuum chamber through a piece of stainless steel tubing, and was then introduced to a heated Teflon sampling line controlled to 100°C. The boiling point of water is substantially reduced at the low pressure of the experiment. Therefore, the temperature in the sample line between the

probe and the vacuum pump did not need to be kept quite as high as the others. The sample then entered the dry scroll pump and exited out the exhaust. The exhaust was connected to another heated sample line held at 121.1 °C to prevent water condensation. The combustion gas sample then traveled from the subsequent heated sample line into the heated gas cell for analysis.

To completely fill the FTIR gas cell with combustion gas sample, the FTIR gas cell was first evacuated to 5 +/-5 torr. The combustion gas sample was then introduced into the gas cell continuously for approximately 10 minutes with the valve on the exit open to the vacuum pump. Then, the gas cell was allowed to fill to the sampling pressure of 550 torr with the combustion gas sample. The total duration of this procedure was between 90 and 180 minutes a depending on which flame was being sampled. The lean flame samples required the longest amount of time for collection. Once the sampling pressure was reached, the FTIR was set to do an analysis of the combustion gas sample in the cell. The samples were analyzed at the same conditions as the background scan, and also took 256 scans per sample.

Due to concerns of sample contamination, the gas cell was evacuated of the previously collected combustion products. The needle valve at the exit of the gas cell was opened and the pressure was reduced down to approximately 5 torr. Then, the inlet valve is opened to enable a purge of UHP N_2, which was allowed to flow for 15 minutes to purge the gas cell. Then, the procedure for sample collecting was repeated for the next location in the flame.

The time scale involved during the sample flow through the probe, sample lines, and gas cell is long compared with the amount of time it takes for radicals to react with the surfaces or other species[47]. Therefore, with this method, only stable species can be identified.

2.3.2 **Calibration Methods and Gases**

To quantitatively measure the concentrations of the analyzed gases, calibration standards for the various species had to be performed. A schematic diagram of the setup used for calibration is shown in figure 2-11. The gases were injected into the gas cell via syringe or directly from a compressed gas bottle. Gases from the compressed gas bottles were allowed to run continuously through the heated gas cell during sampling. Several runs were done with the gas cell closed off from flow to determine if there was any difference in the spectra, but results showed that results were consistent with the continuous flow samples. For continuous flow samples, pressure was held at 550 torr with the Trivac D4A vacuum pump and temperature was controlled to 121.1 °C.

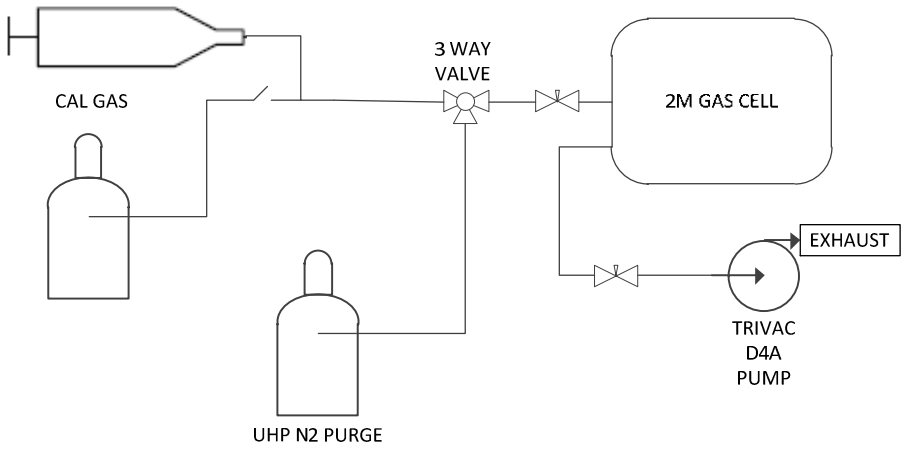

Figure 2-11: Schematic of calibration gas analysis.

A syringe was used to deliver gases when the concentrations in the compressed bottles were higher than the desired sampling concentration. The law of partial pressures was used to calculate the volume of gas needed at atmospheric conditions to achieve the necessary concentrations at the desired volume. The gas cell was filled with the appropriate volume of gas

in order to reach atmospheric pressure. The pressure was then drawn down slowly using a needle valve and then closed once the sampling pressure of 550 torr was reached.

2.3.2.1 Quantification Method

Using the Omnic QuantPad software, a method was compiled using the calibration spectra that were used for quantification of species concentrations. The concentrations for the standard spectra were chosen based on the expected maximum concentration of that particular species. The quantification regions were chosen based on criteria set in the software manual [46] including: the absorbance value had to be less than 1.0 absorbance units, the peaks of interest had to occur in a spectral region where the species is known to exist, and there existed no known interferences from other components. Table 2-2 shows the concentrations used for the calibration spectra as well as the regions chosen for quantification.

Table 2-4: Calibration gases used in experiments and their concentrations.

Calibration Gas	Concentration (PPM)	Quantification Region (cm-1)
Nitric Oxide (NO)	50.20	1911.3-1932.2
Carbon Monoxide (CO)	10,000, 1204	2049.2-2087.2 2090.2-2133.2
Carbon Dioxide (CO_2)	120,000	732.2-766.0
Water (H_2O)	200,000	3211.5-3372.0
Propane (C_3H_8)	30.70	2850.0-3002.0
Methane (CH_4)	2508	2894.5-2999.8

Additional scans of gases with known concentrations of the various species were done to validate the accuracy of the method. Among the validation spectra were various concentrations

of NO, CO, CO_2, and H_2O. C_3H_8 and CH_4 were not validated due to limited access to higher concentration calibration gases, and thus are not presented in the results.

Corrections for nonlinearity at higher concentrations were applied for CO and H_2O. Several points of known concentration were analyzed and used in creation of a calibration curve. In the calibration curve, the known concentration is plotted against the measured concentration and a curve is fit to the points. The equation for the resulting curve is used to correct the deviation from linearity.

In other cases, corrections may be needed to correct for interferences between components that exist in the same region of the spectrum. For example, strong H_2O peaks exist in the quantification region for NO, and can affect how accurately the NO is measured. To determine if a correction was necessary, several scans of mixtures of known concentration of NO and H_2O were performed. The water did not appear to interfere with NO, as the concentrations calculated by the method agreed with the actual concentration. No other interference corrections were considered.

2.3.3 **Temperature Measurements and Thermocouple Corrections**

A thermal analysis of premixed methyl butanoate flames and propane flames was included in this study. Experiments applied the use of a type R, Pt/Pt-13%Rh, thermocouple coated with a ceramic layer to prevent catalytic reactions from occurring on the surface. The temperature measurement methodology was similar to that used in the flame sampling. The burner was raised until the thermocouple insulation tube was at the burner surface. The lowest measurement that could be determined was 0.5 mm above the burner surface due to the interference of the ceramic insulation tube. Therefore, actual measurements began at 0.5 mm and increased up to

20.5 mm. The zero measurement was taken to be the inlet temperature of the gases at the burner. As with sampling, the burner was moved vertically relative to the thermocouple probe to achieve the various results at different positions in the flame.

It is well known that the temperature measured by a thermocouple in a flame may differ from the actual gas temperature. This is true for various reasons including radiation and conduction losses, non-uniform thermocouple heating, catalytic effects, and the effect of thermocouple probe intrusion on the flame [43]. The contribution of these various effects depends on the properties of the thermocouple, as well as the gas phase properties, and the steady or transient conditions of the flame. To achieve a more accurate temperature measurement, various corrections for some of the aforementioned factors must be applied.

2.3.3.1 Heat Transfer Modes

According to Shaddix, thermocouples are the simplest and most common experimental diagnostic used in high temperature and combustion research. However, the quantitative interpretation of the thermocouple measurements in high temperature environments is hampered by the need to account for important heat transfer mechanisms associated with the thermocouple wire and junction, especially thermal radiation [48]. To accurately determine the local gas temperature, a good understanding of the heat transfer modes involved is required. Figure 2-12 shows a schematic diagram of a thermocouple and the various heat transfer modes involved in performing an accurate temperature measurement. For the most general case, the energy balance for the thermocouple is described by equation 2.3:

$$\dot{Q}_{cat} + \dot{Q}_{conv} + \dot{Q}_{rad} + \dot{Q}_{cond} = \rho c_p V \frac{dT_{tc}}{dt} \qquad (2.3)$$

which includes heat transfer from surface induced catalytic reactions, convection between the gases and the thermocouple, radiant heat transfer between the thermocouple and its surroundings, conduction along the thermocouple wires, and transient heating or cooling of the thermocouple.

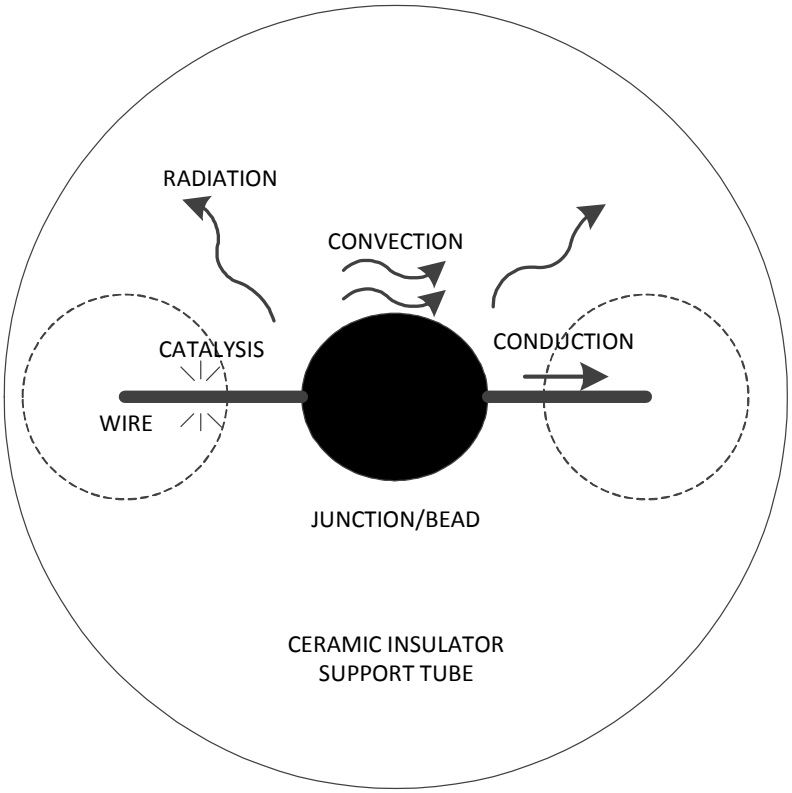

Figure 2-12: Schematic of thermocouple probe displaying the various modes of heat transfer involved in correcting temperature measurements.

Because the thermocouple is used to determine the local gas temperature, the convective heat transfer term dominates over the other effects associated with the thermocouple wire and junction. Transient effects are not applied in the present study due to the steady nature of the premixed low pressure flat flames, and the time taken to allow the thermocouple to reach a steady temperature before measurements were taken. Catalytic and conduction effects are difficult to quantify, so steps were taken to minimize these terms.

Heating due to catalysis has been attributed to the effects of radical recombination on the surfaces of the thermocouple [49]. A quantitative evaluation of catalytic effects is difficult to perform due to the uncertainty in magnitude of the effects and the conditions under which they are important. The primary means of reducing or eliminating these effects is accomplished by applying a non-catalytic surface coating. In the present experiments, a non-catalytic coating was applied to the exposed thermocouple as discussed previously.

According to Shaddix [48], rapid thermal conduction along the thermocouple wires can result in significant heat loss from the thermocouple junction to the lead wire and the thermocouple support. A second consideration is the effect of temperature gradients in the gas phase on the measured temperature. Due to these effects, this heat transfer mechanism is typically negated by aligning the thermocouple along an isotherm. This was accomplished by aligning the thermocouple in a horizontal orientation along the isotherms of the flame.

With catalytic, conduction, and transient effects deemed negligible in the present study, the energy balance reduces to the following equation:

$$\dot{Q}_{conv} + \dot{Q}_{rad} = 0 \qquad (2.4)$$

Radiation from the thermocouple to its surroundings is expected to be the largest contributor to temperature measurement error in this study, and corrections for this effect, as well as convection are discussed in the following sections.

2.3.3.2 Convection

Convection heat transfer about a thermocouple is extremely complicated to calculate. The two factors that make this analysis difficult are the estimation of the properties of the gas mixture surrounding the thermocouple, most notably thermal conductivity, and the selection of the

appropriate Nusselt number correlation for use in modeling the convective heat transfer[48]. The following equation describes the heat convected from the gas to the thermocouple:

$$\dot{Q_{conv}} = hA_s(T_g - T_b) \qquad (2.5)$$

where A_s is the bead surface area, T_g the gas temperature, T_b the temperature of the thermocouple bead and h is the convective heat transfer coefficient of the flow over the thermocouple junction, which is defined as $h = kNu/d$, where k is the thermal conductivity of the gas, Nu is Nusselt number, and d is bead diameter [43].

The Nusselt number correlation is typically chosen based on the geometry of the thermocouple bead, either spherical or cylindrical, or a qualitative evaluation of the diameter of the bead relative to the wire. Spherical correlations are typically used because this ratio is typically 1.5 to 3.0. For cylindrical geometry correlations from Collis and Williams [50], Kramers [51], and Andrews et al. [52] are commonly applied. For spherical geometry, the correlations given by Ranz and Marshall [53], as well as Whitaker [54] are the most commonly applied. In the present work, the spherical correlation of Ranz and Marshall was chosen. The thermocouple was observed under a microscope and the nature of the geometry was very clearly spherical with a bead diameter of approximately 1.5 times the diameter of the wire.

The Ranz and Marshall correlation is given by equation 2.6 and is valid for Reynolds numbers between 0 and 200 with gas properties are evaluated at the gas temperature, T_g:

$$Nu_{d,sph} = 2.0 + 0.60 Re_d^{1/2} Pr^{1/3} \qquad (2.6)$$

Estimation of the properties of the gas surrounding the thermocouple is an important factor in accurate calculation of the gas temperature from the thermocouple measurements[43]. Local gas properties including viscosity, density, specific heat, and thermal conductivity are all

required for the calculation of the Nusselt number. Properties of air or nitrogen are typically used to approximate the gas properties[48]. In the present study, properties of air were employed at the local thermocouple temperature.

For the local gas property calculations, a binary mixture of O_2 and N_2 was assumed. The specific heat was calculated using a polynomial fit of data from the JANAF tables for temperatures between 300 and 3000 K. The viscosity and thermal conductivity were calculated using the collision integral equations described in by Law [55]. Density was calculated using the ideal gas law. Flow velocity was calculated from the mass flow rate of the fuel and air, as well as the mixture density and area of the burner surface ($\dot{m} = \rho v A_b$). These properties were essential in the calculation of the Nusselt number and the convective heat transfer coefficient *h* given by:

$$h = Nuk/d_b \qquad (2.7)$$

where, d_b is the diameter of the thermocouple bead.

2.3.3.3 Radiation

In flames, the temperature measured by a thermocouple is highly affected by radiative heat exchange between its outer surface and its surroundings[43]. The equation for the amount of radiation heat transfer is given as follows:

$$\dot{Q_{rad}} = \varepsilon A_b \sigma (T_b^4 - T_{wall}^4) \qquad (2.8)$$

where σ is the Stefan-Boltzmann constant (σ = 5.67 x 10^{-8} W/m^{2}K^4), *A* the surface area of the thermocouple bead, ε the emissivity of the thermocouple surface, T_b the temperature of the junction, and T_{wall} is the temperature of the surrounding surfaces. The wall temperature is measured using a type K thermocouple adhered to one of the inside surfaces of one of the

vacuum chamber flanges. No corrections are necessary for this temperature as they are relatively low, as compared with the temperatures in the flame.

Radiation losses are the most significant cause of error in measured thermocouple temperature data, especially at temperatures above 1000 K [56]. After assuming negligible conduction loss, and catalytic effects, the energy balance in equation 2.4 becomes valid and can be expressed in terms of equations 2.5 and 2.8, then rearranged to solve for the gas temperature:

$$T_g = T_b + \frac{\epsilon\sigma}{h}(T_b^4 - T_{wall}^4) \qquad (2.9)$$

Overall, performing the radiation corrections is not an easy task. As discussed in section 2.3.3.2, the local gas properties must be determined to enable calculation of the Nusselt number and associated convective heat transfer coefficient, *h.* Radiation corrections are also highly dependent on the size of the thermocouple and the emissivity, a radiative property of the thermocouple surface that is strongly dependent on the surface characteristics, such as material and finish.

Emissivity is also strongly dependent on temperature and wavelength[57]. Heitor and Moreira found that in the range of 600-900°C, the emissivity of a Pt-Rh wire can change as much as 40% [49]. Limited data on ceramic coated thermocouple emissivity is available. However, Ghoddoussi utilized a Ceramabond 569 coated type R thermocouple and performed a study to determine the emissivity of the thermocouple[43]. The thermocouple was heated at vacuum conditions using a DC current from a power supply. An infrared camera was used to image the thermocouple surface and determine the peak temperature. To match the temperature value on the IR camera and the temperature feedback system, the emissivity value was adjusted. The adjustment in the emissivity value was considered to be the emissivity of the thermocouple. The experiment found that over a temperature range of 600-1600 K the emissivity value varied

from 0.7 to 0.4. To utilize the emissivity data of Heitor and Moreira in the present experiment, the data from [43] was linearly interpolated across the given range of temperatures. The resulting polynomial fit was used to determine the emissivity value for the measured thermocouple temperatures.

2.3.3.4 Computation of Radiation Corrections

Computation of radiation corrections were carried out using an iterative MATLAB algorithm created for this project. A function is used in the calculation of the properties of the gas, as well as the flow velocity, with the methods discussed previously. This information is then called into a script with inputs including the measured thermocouple bead temperature, wall temperature, and an emissivity value produced from the linear interpolation. An initial temperature guess for the actual gas temperature is also input, and used to calculate the properties of the gas, Reynolds number, and Prandtl number. These are then used to calculate the Nusselt number and convective heat transfer coefficient. This information is then put into the final equation used to calculate a gas temperature. The difference between the initial guess and the calculated temperature is defined as an error, and a tolerance for acceptable error is defined. In this case a value of 0.01 was used because this is a relatively low value compared to the actual temperature value. If the error is above the defined tolerance the first initial guess is then adjusted to the previously calculated value and the process iterates through once again. This process continues until the error between the guess value and the calculated temperature value is below the error tolerance.

As discussed previously, correction for radiation effects is a difficult task, and accounting for the other heat transfer modes would add to the complication of the process. This is why it is

best to try to eliminate conduction, catalysis, and transient effects that occur when using a thermocouple probe. The results for temperature measurements with radiation corrections are presented in section 4.1.

2.3.4 **Probe Induced Disturbances: Thermocouple Probe and Quartz Microprobe**

This section presents the mechanisms for which disturbances may occur in flames when using thermocouple probes and quartz microprobes. When physical probes cause disturbances, substantial errors in flame measurements may exist. Therefore, it is important to understand the possible causes of these disturbances.

2.3.4.1 Thermocouple Disturbances

According to Fristrom [56], thermocouple intrusion into a gas stream may cause the measured temperature to differ from that of an undisturbed stream. The thermocouple probe has an aerodynamic effect on the flame that produces a velocity-deficient wake that distorts the flame. This phenomenon causes the thermocouple to read temperatures that are further downstream than the actual position, resulting in a temperature reading higher than that characteristic of the undisturbed flame. To reduce this amount of error, the size of the thermocouple must be minimized. Given the small size of the thermocouple probe utilized in the present work, it is believed that these distortions were negligible.

2.3.4.2 External Microprobe Induced Distortions

Microprobes have been used extensively for many years as a diagnostic tool for studying flame composition. However, microprobes are notorious for introducing distortions to the flame that

can result in differences between the composition of the withdrawn sample and the undisturbed flow. This section discusses the possible perturbations that microprobes can cause in flames and how they might have affected the measured concentration profiles in the present work. The topic of microprobe induced distortions has been presented and studied by researchers including Fristrom [56] and many others [47,58–60]. Fristrom [56] categorizes the perturbations caused by microprobes into two categories including external and internal distortions.

External distortions are those that occur upstream of the probe orifice and along the outer surface of the probe. In one-dimensional premixed flames, two main contributors exist, which lead to external distortions. These contributors include the tendency of the probe surface to catalyze flame reactions, and the effect of suction at the sampling orifice[56]. At typical flame temperatures, quartz is a highly catalytic surface acting as a sink for radicals in the flame [47]. The reduction in radicals affects the structure of the flame, and produces a concentration of species different from those present in undisturbed flames[61]. The pre-heat zone of the flame is affected most because the probe presence reduces the flow of radicals from the reaction zone to the burner surface. The post flame zone is not affected because the probe is no longer located between the sampling point and radical source.

The degree to which catalysis occurs is most heavily dependent on probe geometry. The geometry, along with equivalence ratio and system pressure all affect the degree to which radical destruction occurs. According to Fristrom [56], the effect decreases as the angle of the microprobe decreases, the pressure of the system increases, and the closer the equivalence ratio becomes to stoichiometric. For well stabilized flames, even relatively blunt probes have been used successfully, such as the 80° angle probe used in the work of Cattolica and coworkers[62]. In the present work, a well stabilized flame is utilized, and the sampling probe is drawn out to a

low profile external angle (~11°) and is of rather small size. Therefore, this effect is not expected to have played a role in variation of the flame and measured concentrations of species.

In microprobe sampling, the pressure downstream of the orifice is much lower than that of the reacting flow stream to achieve choked flow at the orifice. The choked probe withdraws a sample just slightly upstream of the probe position. This suction effect accelerates the reactant molecules and brings them to the probe more quickly than molecules outside of the suction region [47]. This phenomenon results in what is called an apparent profile shift. Specifically, the molecules extracted from the flame are characteristic of a position a short distance upstream of the probe tip. The apparent profile shift is discussed in the literature and is typically found to be on the order of 1 to 3 orifice diameters for probe sampling [60,63,64]. This effect is much more substantial with the use of molecular beam mass spectrometry than for microprobes. Except very near the burner surface an upstream shift of experimentally determined profiles will result in good agreement between molecular beam mass spectrometry (MBMS), microprobes, and less intrusive optical measurements for stable species[56].

Closer to the burner surface, an overlap exists between the upstream region sampled by the probe and the burner surface. Here, the probe effectively pulls the sample from inside of the burner as well as in regions above the probe tip. As a result, reactants will be measured at levels below actual concentration, and intermediates and products will be measured at levels above their actual values[59]. Further, if sampling occurs even nearer to the surface, a lack of pores in the sintered bronze plate may block flow to the sampling probe, causing the sample to come from regions downstream of the probe tip. However, if the probe is aligned with a pore, the sample will originate from the flow inside of the burner.

Yi and Knuth [64] performed numerical calculations to address the phenomena responsible for the profile shift. A model of a MBMS probe immersed in a nonreactive binary mixture flow stream was used to visualize the streamlines and concentration contours in the flow. Yi and Knuth found that near the orifice the perturbation caused by acceleration of flow resulted in a concentration profile shift of 1 to 2 orifice diameters upstream of the location in the undisturbed flow. Based on these results, it is expected that the profile shift associated with a microprobe is not significant. They postulated that when mass convection dominates conditions at the orifice, the following equation can be used to calculate the apparent profile shift:

$$\frac{\delta}{d} = 0.19(ReSc)^{1/2} = 0.19\left(\frac{cd}{D_{AB}}\right)^{1/2} \qquad (2.10)$$

where *Re* is the Reynolds number, *Sc* the Schmidt number (ratio of viscosity to mass diffusion rate), *d* the diameter of the orifice, δ the apparent profile shift, *c* the sound speed at the orifice, and D_{AB} is the binary diffusion coefficient at the orifice. The equation is valid when the upstream region sampled by the probe does not overlap with the burner surface.

In the present work, for conditions at the orifice and a binary mixture of air and carbon dioxide, the apparent profile shift was found to be less than one orifice diameter. Therefore, the effect of suction was assumed to have a nearly negligible effect on the measured gas sample compositions and positions in this study

2.3.4.3 Internal Microprobe Distortions

Distortions that occur once the sample enters the probe orifice are considered internal distortions. In microprobes, these typically result from a failure to quench chemical reactions properly. Chemical reactions are quenched in two ways, including, reducing the concentration of radicals

in the sample and by substantially lowering the temperature. Radical removal is adequate if only looking for stable species, and if successful, higher temperatures can be tolerated within the probe. When radicals are removed, reaction rates are severely reduced and stable species are preserved.

Radical destruction occurs on the internal probe walls and Fristrom suggests that a good microprobe should have dirty, catalytically active inner walls, contrary to what is necessary on the external walls of the probe for preventing catalytic effects. However, it is difficult to obtain sufficient radical removal at a fast enough rate to be a satisfactory quenching mechanism. Probes are typically designed so that the sample gas undergoes a rapid expansion after the orifice, introducing a high cooling rate to the gas. Consequently, for microprobes, a combination of this aerodynamic and convective cooling and radical removal occur.

To achieve sample preservation gas temperatures must be lowered abruptly. This objective can be achieved by ensuring sonic conditions at the probe orifice. With the orifice choked, supersonic expansion occurs in the probe tip, greatly reducing temperatures of the gases. Viscous effects that occur within the probe promote a shock wave. The sample is heated by compression and can again reach temperatures where chemical reactions become important, but ideally enough radical loss or heat transfer has occurred to effectively quench combustion reactions. A return back to subsonic flow typically occurs downstream in the probe body, but for small enough probes with higher viscous losses it can occur in the diverging entrance of the probe.

Because convective cooling and wall radical loss are relatively slow processes, Fristrom [56] suggests that it is important to minimize viscous losses as much as possible to delay subsonic flow by using as large of a diameter orifice as is practical and keeping the probe flow

area constant and straight as long as possible. However, this is only effective if the back pressure on the probe is maintained low enough to achieve quenching. As the channel size decreases, viscous losses increase, and the lower the back pressure needs to be to achieve quenching.

Chemical reactions within the probe can occur if quenching is not achieved or if gas temperatures in the probe become high enough to restart those reactions. Therefore, it is important to design the probe and use conditions in which this cannot occur. Using the following equation it is possible to calculate the maximum back pressure required for choked flow [47]:

$$\frac{p_g^*}{p_{g,0}} = \left(\frac{2}{\bar{k}+1}\right)^{\frac{\bar{k}}{\bar{k}-1}} \qquad (2.11)$$

where $p_{g,0}$ is the pressure of the gas stream (e.g.100 torr), $\bar{k}$ the average ratio of specific heats (assumed to be 1.4), and p_g^* the pressure at choked conditions. For the present experiment, the maximum back pressure value required for choked flow is 52.8 torr.

Viscous effects may reduce the pressure from the probe inlet to the probe outlet, implying that choked conditions may not be achieved at 52.8 torr[58]. To avoid this problem, the back pressure is reduced beyond this value to 6 torr. For the current work, the FTIR sensitivity to pressure is not a concern because the sample flows at a higher pressure from the exit of the dry scroll vacuum pump than the pressure in the probe.

It is also important to understand the effect that residence time in the probe has on the gas sample. Kaiser [65] suggests that it is possible to check for gas reactions occurring inside of the probe by collecting samples at different probe back pressures, but otherwise identical conditions. This effect could be especially important in the pre-flame zone, as well as the flame zone nearer

the burner surface, because the samples that are extracted by the microprobe have not yet passed through the hottest part of the flame. The concern is that if the temperatures are hot enough and the residence time is long enough then homogeneous gas phase reactions could begin once again.

The choked mass flow rate into the probe is dependent only on the probe orifice diameter and the upstream conditions. Contrarily, the gas residence time depends on the gas velocity, which is in turn dependent on the back pressure in the probe. The residence time of gases in the probe in the high temperature regions of the flame is reduced by reducing the back pressure. If reactions occur in the high temperature zone of the probe, then changes in species concentration measurements would be observed when the back pressure is varied.

Nogueira [47] performed an experiment in which the pressure downstream of the probe orifice was varied to determine if reactions occur. A methane flat flame at just below atmospheric pressures and a microprobe was used that was very similar in design that used in the present work. Quantitative results of CO and CO_2 concentration measurements were presented at varying back pressures between approximately 5 and 250 torr. When the sampling pressure was below 60 torr, the CO and CO_2 concentrations no longer varied. This result was consistent with the results of Seery and Zabielski [66], who performed a comparison between probe and optical laser adsorption species measurements. Nogueira also found that in the pre-heat flame zone and flame zone none of the quantified species were sensitive to a reduction in residence time. However, in the post-flame zone, some of the CO is converted into CO_2. But, as stated before, once the back pressure was reduced to below 60 torr, this effect no longer occurs.

While these results may not correlate directly with the present experiment conducted at low pressure, it is believed that similar results can be achieved and that the back pressure should

be sufficiently low to reduce the residence time in the probe to prevent further reactions from occurring. This will be revisited with the presentation of results in Chapter 4.

3. Modeling Approach

The objective of this chapter is to introduce the conditions and chemical mechanisms employed in computational analysis for comparison with experimentally measured species concentration and temperature profiles. Modeling for both methyl butanoate and propane were completed using existing chemical kinetic mechanisms. In the case of the methyl butanoate mechanism, the addition of NO_x chemistry was added and is discussed. The CHEMKIN software (Reaction Design – San Diego, CA) was chosen to perform the necessary tasks involved in the numerical approach.

3.1 Motivation for Numerical Analysis

Internal combustion engines employ a complex procedure involving fuel atomization, fuel-air mixing, ignition, and combustion. This process is highly unsteady, heterogeneous, 3-dimesional and is difficult to analyze computationally[67]. Simulations that re capable of combining the complex phenomena involved in the engine combustion processes are computationally intensive and/or must employ simplifications in chemistry and/or fluid mechanics. To reduce the computational complexity of this problem, both experiments and modeling are typically performed using a simplified geometrical configuration such as the premixed laminar flame configuration employed herein. This technique allows for the researcher to understand the effects of molecular structure on combustion and emissions by considering full, detailed chemical kinetics.

The many processes involved in engine combustion are non-equilibrium processes that depend on the rate of each individual chemical reaction which are defined by the temperature

and concentration of reactants. The rate at which reactant species are consumed and product species are produced is governed by the law of mass action which states that the rate at which reactants are consumed is proportional to the product of the concentrations of each reacting chemical species, raised to its stoichiometric coefficient. The equation used in calculation of k_f, the forward rate coefficient, is given in the Arrhenius form:

$$k_f = AT^{\beta} e^{\frac{-E_a}{RT}} \qquad (3.1)$$

where A is the pre-exponential factor, E_a the activation energy, T is temperature, and R is the universal gas constant. The chemical kinetic mechanism is essentially list of the chemical reactions and their reaction rate constants required for accurately predicting the combustion processes involved in a system. A chemical kinetic mechanism can be validated using a wide range of experimental data obtained from laboratory experiments.

3.2 Mechanism for Computational Analysis

The chemical mechanisms used in this study include the detailed mechanism for methyl butanoate combustion compiled by Gail et al [38] and the most recent small hydrocarbon mechanism of Konnov [30]. The existing available mechanisms for methyl butanoate such as the Gail mechanism did not contain the chemistry required for NO_x formation. Therefore, it was necessary to combine the two mechanisms. For propane analysis, the Konnov mechanism was sufficient as it contained a detailed NO_x mechanism.

The Gail mechanism consists of 295 chemical species and 1498 chemical reactions, as well as thermochemical data and transport properties for each species. The model has been validated with various experiments including a jet-stirred reactor, opposed-flow diffusion flame, and a variable pressure flow reactor, with results showing that the model was in good agreement with

the experimental results from these studies. The mechanism does not include reactions involving nitrogen, and thus, NO_x chemistry.

The Konnov mechanism for small hydrocarbon combustion has been used widely in computational research for many years. It consists of 130 species and 1231 reactions, thermochemical data, and transport data, including nitrogen chemistry. The Konnov mechanism was used for analysis of the propane flat flame model, and the NOx sub-model of Konnov was added to the Gail methyl butanoate mechanism to compare predicted NO_x production between the two fuels.

Because the focus of this study is NO formation in methyl butanoate flames, it was necessary to combine the two mechanisms due to the lack of NO_x chemistry in the Gail mechanism. Although many chemical kinetic mechanisms exist that include NO_x chemistry, the Konnov mechanism has been recently modified and tested against a variety of data sets [29] on the combustion of small hydrocarbons (CH_4, C_2H_6, C_3H_8) in flat flame burners similar to the experiments presented herein. Therefore, the Konnov mechanism was deemed to be suitable for this study.

Combining the two chemical kinetic mechanisms does not necessarily constitute a proper approach for model development, as the various models may have been derived in an inconsistent manner[17]. However, due to the lack of methyl butanoate models that contain NO_x submechanisms, the aforementioned models were combined to provide an appropriate analysis tool for the present work.

3.3 CHEMKIN Code for Computational Analysis

The computational code used to perform flame calculations for the present work was the CHEMKIN-PRO Release 15112 software package. With this software, the user inputs the chemical kinetic files as well as initial conditions and species information. The information is used to compile a set of differential equations for solution of the problem. A detailed explanation of the governing equations for burner-stabilized premixed laminar flames can be found in the CHEMKIN Theory Manual [68], and are presented in the following information.

In order to appropriately perform a numerical computation of the premixed flat flame burner experiments employed in this study, the premixed laminar burner-stabilized flame simulation available in CHEMKIN-PRO was chosen. This model assumes 1-dimensional flow with uniform inlet conditions. The conservation equations of mass, energy, species, and the ideal gas law equation of state are solved are solved in order to determine species concentrations and temperatures produced in the flame. The conservation of mass equation, or rather, continuity equation for the 1-D flame used in the calculations is as follows:

$$\dot{m} = \rho u A \qquad (3.2)$$

where $\dot{m}$ is the mass flow rate, ρ the mass density, u the velocity of the fluid mixture, and A the cross sectional area of the stream tube encompassing the flame. The cross sectional area normally increases due to thermal expansion that occurs in the combustion process, however, in the model this area is taken to be constant. This equation describes the flow of mass in and out of the system, and is essential in understanding the mass properties at differing locations in the flame.

The conservation of energy equation is shown in equation 3.2 and includes the terms for mass transfer, conductive heat transfer, diffusion effects, convective heat transfer, and radiative heat transfer.

$$\dot{m}\frac{dT}{dx} - \frac{1}{c_p}\frac{d}{dx}\left(\lambda A\frac{dT}{dx}\right) + \frac{A}{c_p}\sum_{k=1}^{K}\rho Y_k V_k c_{p,k}\frac{dT}{dx} + \frac{A}{c_p}\sum_{k=1}^{K}\dot{\omega}_k h_k W_k + \frac{A}{c_p}\dot{Q_{rad}} = 0 \qquad (3.3)$$

Conservation of species is determined using the following:

$$\dot{m}\frac{dY_k}{dx} + \frac{d}{dx}(\rho A Y_k V_k) - A\dot{\omega}_k W_k = 0 \qquad (3.4)$$

where T is the temperature, c_p the specific heat, λ the thermal conductivity of the mixture, Y_k the mass fraction of the kth species, V_k the species diffusion velocity, c_{pk} the species specific heat, $\dot{\omega}_k$ the net chemical production rate from gas phase reactions, h_k the specific enthalpy, and W_k the molecular weight of the species. The mass of each individual species varies with time in chemically reacting flow systems because species are created and destroyed through chemical reaction and are also transported via molecular diffusion in the presence of concentration gradients. The equation of state is the ideal gas law in equation 3.4 where P is the pressure, $\bar{W}$ is the mean molecular weight of the mixture, and R is the ideal gas constant. This auxiliary equation is essential in solving the complete set of governing equations.

$$\rho = \frac{P\bar{W}}{RT} \qquad (3.5)$$

In the model, these governing equations in their differential form, are numerically integrated to generate concentration profiles for reactants, intermediates, and products, as well as temperature profiles[69]. Three files describing the elementary gas phase reactions involved in the chemical mechanism, thermochemical properties of the species, and transport properties are required to solve the burner-stabilized flame problem.

The chemical kinetic file identifies the species present and the mechanism for the production and consumption of species. The chemical kinetic mechanism describes each reaction that takes place and the corresponding reaction rate parameters in the Arrhenius form detailed in equation 3.1. The rate coefficients used in the chemical mechanism of this study originate from previously published computational and experimental results, as well as comprehensive databases such as the NIST Chemical Kinetics Database [70].

Thermochemical data are required for each species in the chemical kinetic file to calculate thermodynamic properties, thermal transport properties, and reaction equilibrium constants. The properties included in this file are species name, elemental composition, electronic charge, and phase, as well as coefficients used to fit polynomials for constant pressure heat capacity ($C_p°$), molar enthalpy of formation ($\Delta H°$) and molar entropy of formation ($S°$) for all temperatures. From this information CHEMKIN is able to calculate constant volume heat capacity, internal energy, Gibbs free energy, and Hemholtz free energy. The molecular weight is used to convert molar properties to mass properties. Thermochemical data are derived similarly to the kinetic data, originating from previous results as well as the NIST Chemistry WebBook [71].

Generally speaking, combustion is represents a combination of chemical kinetic processes (production and destruction of species) and transport properties (convection, diffusion, and conduction)[67]. Some combustion applications are kinetically rate controlled and transport processes are less important. . However, for cases such as the laminar premixed burner flame (as well as diffusion flames) the rates are controlled by transport processes, and it is necessary to determine molecular transport of species, momentum, and energy of the gas mixture. The transport properties are evaluated from diffusion coefficients, viscosities, thermal conductivities,

and thermal diffusion coefficients. These flow properties are determined from the standard kinetic theory, and gas properties are determined using mixture averaging in CHEMKIN.

3.4 Model Parameters

As discussed previously, the laminar burner-stabilized flame problem was used to simulate the methyl butanoate and propane flat flames utilized in experimentation. For methyl butanoate, the Gail methyl butanoate mechanism was combined with the Konnov mechanism to include NO_x chemistry. For propane flame simulations, the Konnov mechanism was used without modification. The thermochemical and transport data provided with both mechanisms was also utilized in analysis. For the methyl butanoate cases, the data from each mechanism also had to be combined. The various files were uploaded into the CHEMKIN project file and pre-processed to organize the included information, and then boundary and initial conditions were entered.

Both the fixed gas temperature and energy equation solutions were used in calculations. The computations were first performed for the fixed gas temperature case with an input temperature profile. The temperature profiles used were those measured from the flames and subsequently corrected for radiation effects. Both the mixture-averaged transport and correction velocity formalism options were selected. To verify that the results were consistent, the energy equation solution was performed as well. The energy equation solution was carried out as a continuation of the initial solution, using the information from the latter as an initial guess.

Various operating conditions for the burner had to be specified in the analysis. The provided temperature profiles consisted of the experimentally measured data as well as the location where they were measured in the flame. The pressure was set to the experimental

pressure of 100 torr, while all other reactor physical properties were kept to the default values as specified in the CHEMKIN manual.

The computation grid describes the spatial region used in computational analysis. The region is described by axial position in the flame, which in this case is the vertical position in the flame. The area of analysis included heights from 0 mm, at the burner surface, to 20.5 mm, well above the burner surface. The other grid parameters were held to defaults. Species specific properties were generated using the auto-populate option.

Burner inlet parameters were also required to be included for analysis, including the cold flow velocity and equivalence ratio of each flame. The cold flow velocities were calculated from the mass flow rates and properties (pressure, inlet temperature, mixture density, burner area) recorded from the experiments. The mole fractions of each reactant species involved (C_3H_8 or $C_5H_{10}O_2$, O_2, N_2) in the experiments were calculated from the various equivalence ratios used: 0.8, 1.0, and 1.2. All solver properties were kept at the default values, and no sensitivity analyses were performed.

After the continuation for a solution to the energy equation was entered, an input file was created, and then the model was ready for analysis. The computational time required for each simulation is dependent on the complexity of the mechanism used. Therefore, the methyl butanoate studies required substantially longer computational times in comparison to propane. After each simulation was completed, species and temperature data were exported from the post-processor and further post processing was performed in excel. Results are presented in Chapter 4 along with the experimental results for direct comparison.

4. Results and Discussion: Experiments and Numerical Modeling

The goal of this chapter is primarily to compare and discuss experimental results obtained from the temperature probe and microprobe sampling of propane and methyl butanoate flames. It is well-known that nitric oxide emissions from the combustion of methyl ester fuels are generally found to be higher than that of similar chain length hydrocarbon fuels when these fuels are burned in diesel engines. However, as discussed above, the mechanisms by which biodiesel results in increased NOx formation are complex and multiple. NO_x emissions contribute to atmospheric pollution issues, such as smog, that cause adverse human health effects.

This chapter seeks to compare the experimental results found from the methyl butanoate and propane flames, as well as the computational results which were performed as described in Chapter 3. The first section details the temperature profiles obtained using the thermocouples made in the laboratory. Second, the species concentration profiles obtained from the microprobe are presented and discussed. Finally, the experimental and modeling results are presented for comparison.

4.1 Temperature Profiles

The technique used in obtaining temperature profiles involved the use of a Pt/Pt13%Rh, type R, thermocouple. The bare wires of the thermocouple were placed in a ceramic insulator tube with a double bore configuration, and then attached to the correct thermocouple connector. The thermocouple bead and lead wires exposed to the flame were coated with an alumina ceramic based paste, Ceramabond 569. Corrections for radiation effects were performed and discussed in section 2.3.3. These corrections account for heat lost from the thermocouple to the surroundings,

in this case the temperature of reference was obtained from the wall of the vacuum chamber. Temperature values were obtained for lean ($\varphi = 0.8$), stoichiometric ($\varphi = 1.0$), and rich flames ($\varphi = 1.2$) at vacuum conditions, P = 100 torr. Sampling locations ranged from 0 mm at the surface of the burner to 20.5 mm above the burner surface, providing a detailed profile of the temperatures in the flame. Plots of experimentally obtained temperatures for the various stoichiometry flames are depicted in figures 4-1, 4-2, and 4-3 and present a comparison of the methyl butanoate and propane flames. The temperature values were found to be repeatable, as repeat temperature measurements were obtained for the propane flames and temperatures were only found to vary by approximately 20 K.

Each graph illustrates the experimentally obtained temperature profiles for both a methyl butanoate and propane flame of the same equivalence ratio. Figure 4-1 illustrates the results from the stoichiometric methyl butanoate-air and C_3H_8-air flames. The methyl butanoate temperatures were found to be higher than those of the stoichiometric propane flame, which was expected given difference in gas temperatures exiting the burner. Specifically, the unheated propane reactants exited the burner at a lower temperature than the MB reactants, causing lower initial temperatures and a later peak.

The temperature increases rapidly as the probe approaches the luminous zone at approximately 3 mm. The maximum temperature for the methyl butanoate, 1803 K, flame occurred at a position 4.5 mm above the burner surface, while the propane maximum, 1676 K, was found at 5.5 mm, both downstream of the most luminous zone of the flame. After the peak locations the temperatures begin to decrease although not substantially. Far downstream, at a location of 20.5 mm above the burner surface, the temperatures only differ from the maximum by about 200 K.

Figure 4-2 shows the results from the lean methyl butanoate-air and C_3H_8-air flames. As expected, the overall temperatures measured are lower than the temperatures of the stoichiometric flames. The lean flames have the same general profile as the stoichiometric, beginning with the unburned gas temperature and an abrupt increase in flame temperature as the thermocouple nears the luminous zone. Again, the maximum temperatures occur after the luminous zone of the flame at a location of 5.5 mm for both the MB and propane flames. The maximum temperatures were 1696 K and 1532 K for the methyl butanoate and C_3H_8, respectively.

The temperatures obtained from the rich methyl butanoate and C_3H_8 flames are shown in figure 4-3. Again, the data follow a curve characteristic of both the stoichiometric and lean flames. The methyl butanoate and C_3H_8 temperatures are much closer to one another in this instance than in the previous flames, with the maximum temperatures only varying by 57 K. The peak temperatures occur at a location of 4.5 mm for both rich flames, and were found to be 1868 K for MB, and 1811 K for C_3H_8. Overall, the rich flame temperatures were higher than that of the stoichiometric flame. Generally, a flame that has a stoichiometry just above 1.0 will result in the highest flame temperatures. Because of these results, it is believed that the "hottest" stoichiometry occurs near the mixtures used in the rich flames. As mentioned before, due to discrepancies with the fuel vaporizer, the equivalence ratio was only known within about +/- 0.1, so the temperatures for the methyl butanoate flames could vary from the experimentally obtained values presented here. Although, it is believed that the information presented is characteristic of lean, near stoichiometric and rich MB flames.

Figure 4-4 shows a further comparison of all the temperature data obtained, displaying results for each of the 6 flames. It further shows the temperature differences between the lean, rich, and stoichiometric flames of the two fuel types.

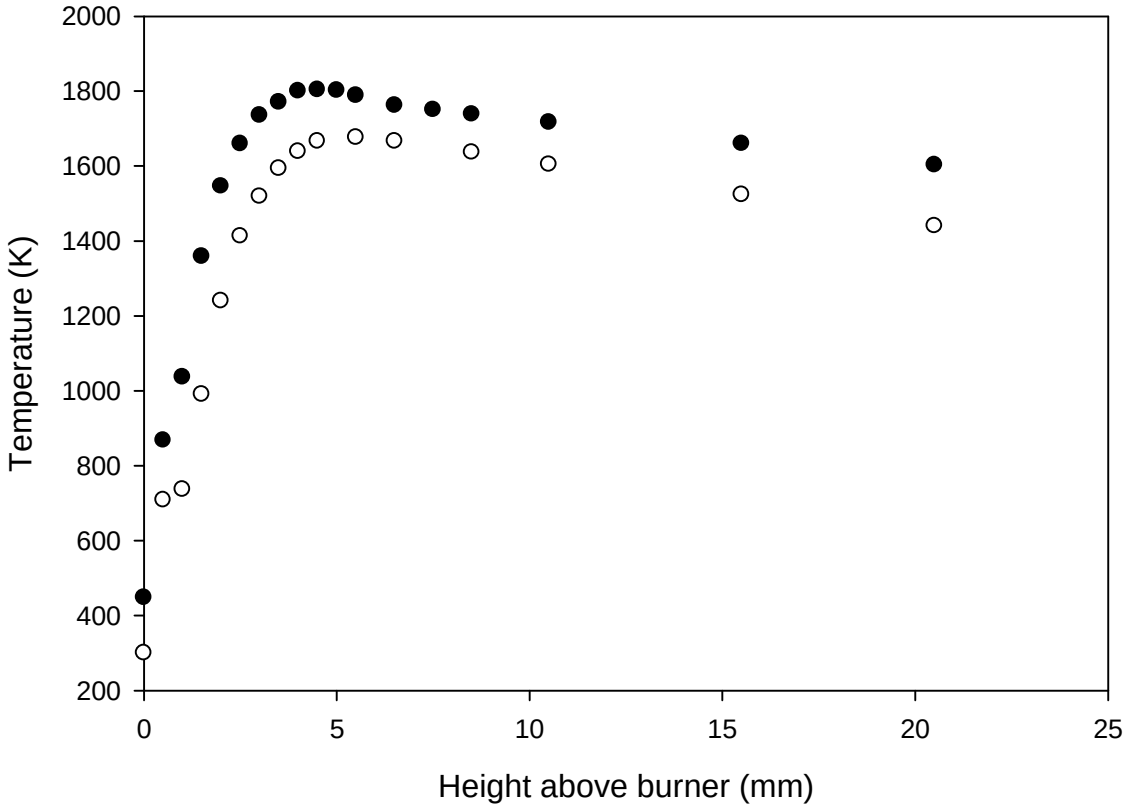

Figure 4-1: Temperature profiles for ø=1.0 $C_5H_{10}O_2$-air and ø=1.0 C_3H_8-air flames. The filled in circles (•) represent the methyl butanoate data, while the empty circles represent the propane data.

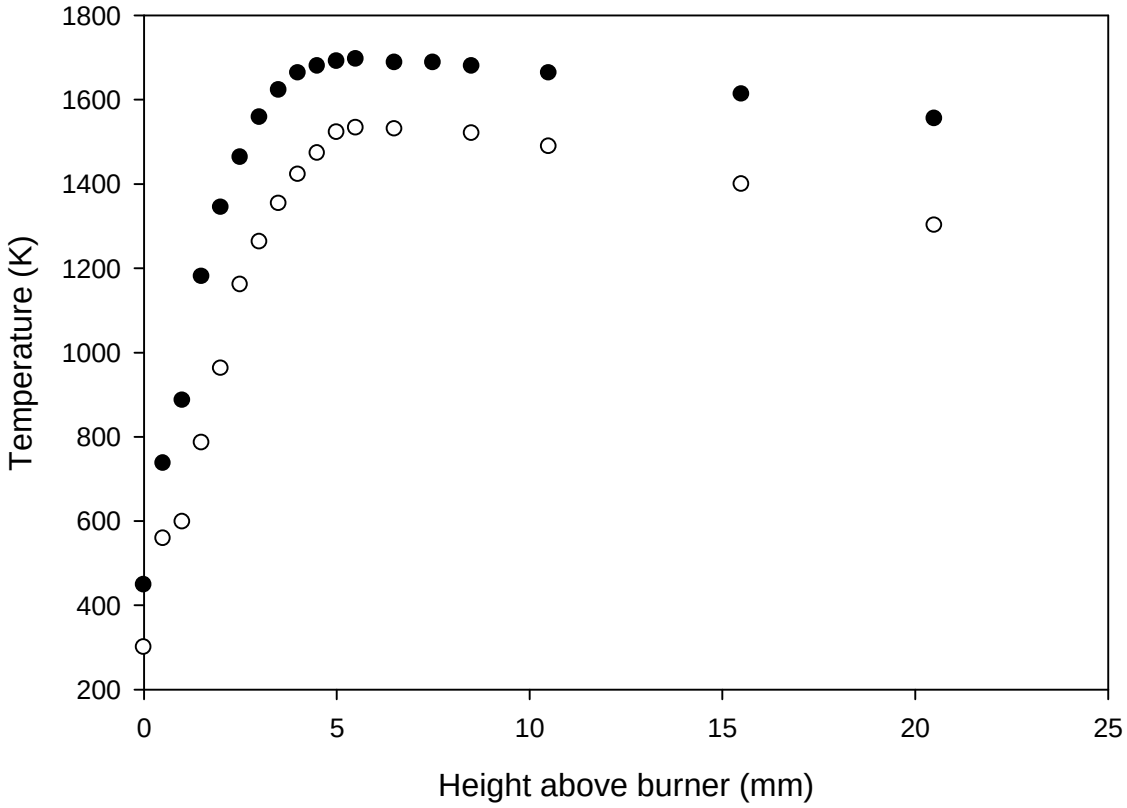

Figure 4-2: Temperature profiles for ø≈0.8 $C_5H_{10}O_2$-air and ø=0.8 C_3H_8-air flames. The filled in circles (•) represent the methyl butanoate data, while the empty circles represent the propane data.

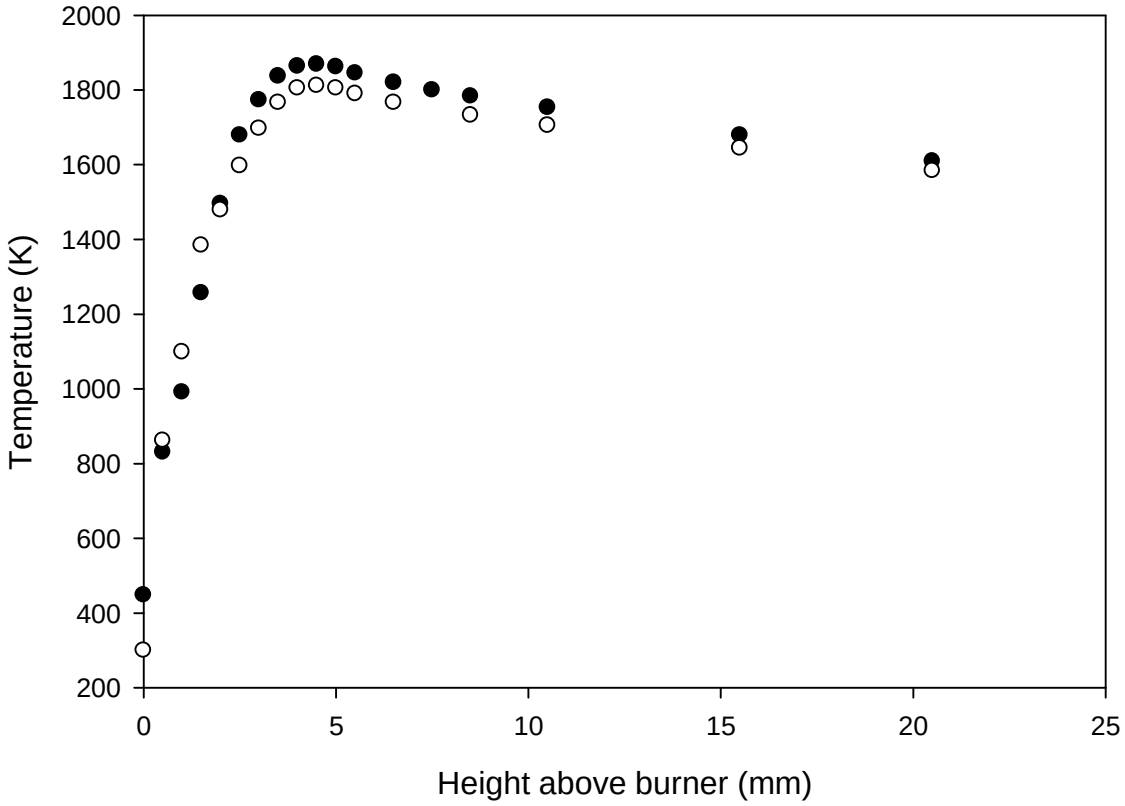

Figure 4-3: Temperature profiles for ø≈1.2 $C_5H_{10}O_2$-air and ø=1.2 C_3H_8-air flames. The filled in circles (•) represent the methyl butanoate data, while the empty circles represent the propane data.

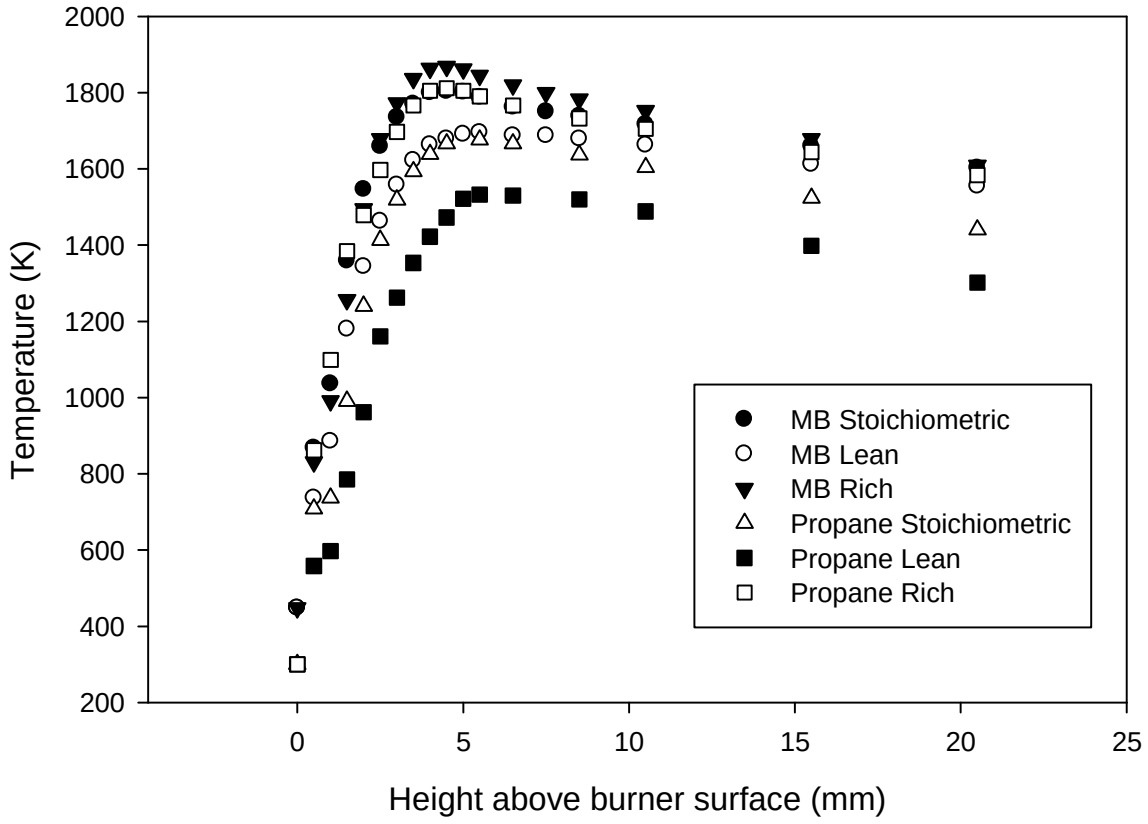

Figure 4-4: Plot of the temperature profiles obtained from the present study for φ=1.0, 0.8, and 1.2 $C_5H_{10}O_2$-air and C_3H_8-air flames, corrected for radiation losses.

4.1.1 **Temperature Data Validation**

In this section, a comparison of propane temperature data from the present study and data taken from a similar experiment conducted by Westblom et al [72] is presented. Westblom and coworkers performed OH laser induced fluorescence of a rich, φ = 1.15, propane-air flame with and without a manganese fuel additive. For the purposes of this study, only the additive free propane-air flame information is presented. The burner used was a 6-cm diameter, water-cooled sintered brass McKenna burner mounted in a vacuum chamber. The pressure was held 40 torr,

lower than the present experiment which was conducted at 100 torr. Although the experiments are not exactly the same, it is felt that there are enough similarities to perform a comparison and illustrate that the temperature measurements taken with the type R thermocouple and corrected for radiation effects are in line with results previously presented by others. Figure 4-5 below shows the temperature data for the two experiments.

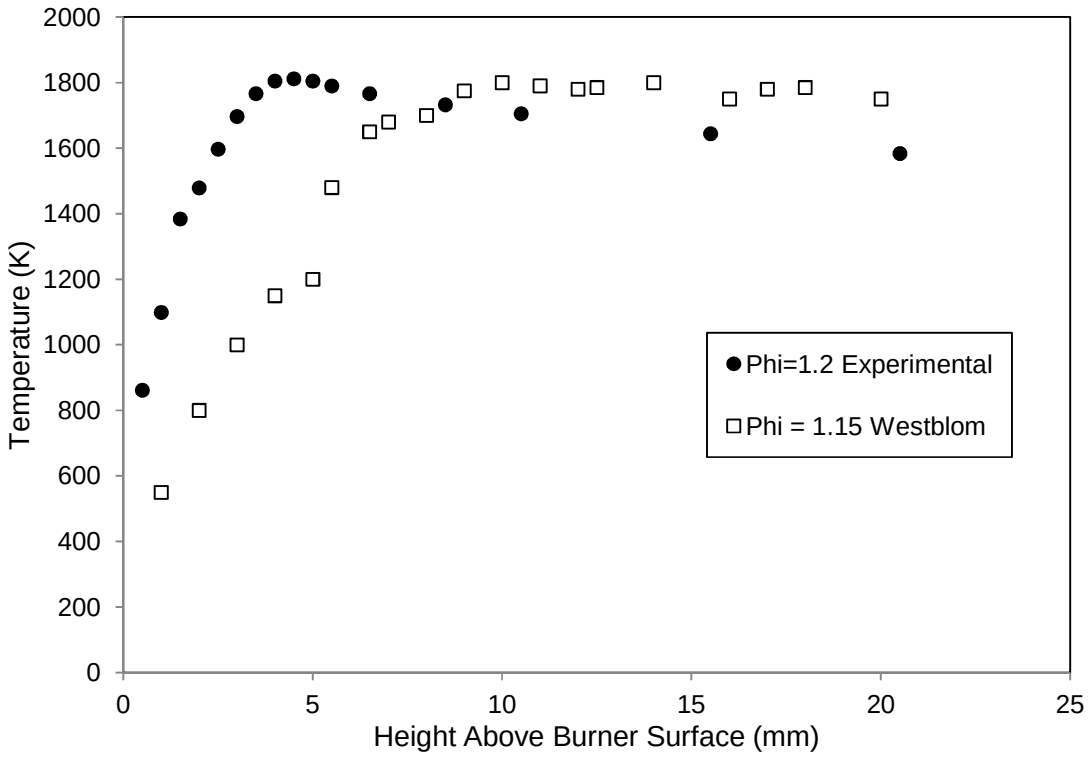

Figure 4-5: Temperature data comparison for φ=1.20 C_3H_8-air flame and Westblom's φ=1.15 C_3H_8-air flame. The filled in circles (•) represent the data from the present experiment, while the empty squares represent the data taken from the OH LIF experiment by Westblom et al. [72]

The temperature results from the rich, φ=1.2, propane-air flame from the present experiment are plotted with Westblom's φ=1.15 low pressure flame. The lower pressure of Westblom's experiment results in a flame that sits higher off of the burner surface than the

present experiment, so the maximum measured temperature occurs at a point further downstream. The experimental temperature profile follows the same general shape an also reaches a maximum temperature nearly identical to that presented in Westblom. The maximum temperature recorded in the present work was 1811 K, while the Westblom data present a maximum of approximately 1800 K. This comparison suggests that the temperatures taken with the thermocouple and corrected for heat transfer effects are consistent with data provided from previously performed experiments.

4.2 Species Concentration Profiles

In the present section, the species concentration profiles obtained from the quartz microprobe sampling and subsequent analysis by FTIR spectroscopy are presented. Data were taken for 6 different flames including stoichiometric, lean, and rich (φ=1.0, 0.8, 1.2) methyl butanoate-air and C_3H_8-air flames. The results for methyl butanoate and C_3H_8 are displayed on the same plots to establish a comparison between the two fuels. Temperature data were previously compared and discussed in section 4.1.

The species concentrations presented in the following include NO concentration levels as well as CO and CO_2 mole fractions. Concentrations for other species were measured but, due to limited calibration capabilities, they are not presented here. The measured concentrations of these species including H_2O, C_3H_8, and CH_4 are included in the Appendix.. Also, the standard error information for the data are presented in sections 4.3.2 and 4.3.3 rather than this section in order to more clearly see data taken at the same locations in the flame. This information is also tabulated in the Appendix.

4.2.1 **Nitric Oxide**

Figures 4-6, 4-7, and 4-8 show the species concentrations of NO found for the 6 low pressure flat flames using the quartz microprobe sampling technique. The plots show the concentrations in parts per million (ppm) as a function of height above the burner surface in mm. For the methyl butanoate flames, 8 samples were taken from locations of 0 mm to 8 mm above the burner surface. For the propane flames, 12 sample points were taken in the same range of 0 mm to 8 mm. Fewer points were obtained for the methyl butanoate flames because of the limited fuel supply and time constraints. The sampling locations used for the methyl butanoate flames were chosen based on the profiles obtained for propane and sufficiently represent similar trends.

Figure 4-6 presents the data for the stoichiometric methyl butanoate and C_3H_8 flames. The two fuels appear to follow the same trend, beginning with a sharp increase to about 1.5 mm then decreasing down to lower concentration levels after 2 mm. Maximum concentrations were 67.5 ppm (at 1.5 mm) for C_3H_8 and 65.9 ppm (at 1.0 mm) for methyl butanoate. The concentration level appears to steady out once the luminous zone of the flame is reached and samples continue downstream. Here the concentrations reach levels on the order of 10 ppm or less. In this instance, the two fuels appear to produce NO concentration levels that are very nearly the same. The only obvious dissimilarities exist at 0 mm and 2 mm. At 0 mm the C_3H_8 initially has higher NO concentration, but then virtually matches the concentrations for methyl butanoate. At 2 mm, in the zone where the concentrations dip back down to lower levels, NO was found to exist in a higher concentration for the methyl butanoate flame.

For the lean methyl butanoate flame, shown in figure 4-7, the concentrations obtained for NO are much lower that measured for the C_3H_8 flame near the burner surface from 0 mm to 2

mm. Again, higher concentrations of NO exist in the region upstream of the luminous zone of the flame, followed by a rapid decrease from 2.0 mm to 2.5 mm. The measured NO profile for the lean C_3H_8 flame increases between 2.5 mm to 3 mm, and then decreases in small amounts as the sampling location becomes further downstream. After 3 mm, the measured NO concentrations for the lean methyl butanoate flame levels out to between 3 and 5 ppm. The highest recorded concentration for the MB flame was 37.4 ppm, while for propane the maximum was 76.9 ppm.

The NO concentrations found for the rich flames are shown in figure 4-8. The rich methyl butanoate results begin at higher concentrations and reach a larger maximum NO concentration in comparison to the propane flames. The maximum concentration found for the rich methyl butanoate flame was 50.6 ppm at 1 mm, while the propane reached 46.1 ppm at 1.5 mm. The concentrations again follow a curve similar to that shown for the stoichiometric and lean flames. The highest levels occur prior to the luminous zone, decrease once in the luminous zone, then level out in the post flame region. The methyl butanoate samples taken in the luminous zone and post-flame region show NO concentrations lower than propane.

All concentration profiles for NO in figures 4-6, 4-7, and 4-8 begin with relatively high concentrations near the burner surface. The location of this occurrence is difficult to explain because it is expected that the highest NO concentrations to occur further downstream in the flame where the hottest temperatures occur. Even if the prompt NO_x mechanism were dominant, it would result in a rapid increase in NO at the reaction zone (which is located well above the burner surface, near the location of maximum temperature). Accordingly, it is highly likely that the microprobe cannot effectively collect samples in this region of the flame. As mentioned in section 2.3.4.2, various experimenters have stated that taking samples below the luminous zone

of the flame can lead to discrepancies in concentration measurements. Such results are caused by both external and internal effects.

External effects such as the apparent profile shift, and overlap between the probe and burner surface could be contributing to the early concentrations of NO. However, it is believed that due to the geometry of the probe, internal distortions have more of an effect. It is possible that in the pre-heat zone the sample is being effectively quenched. However, the sample has yet to go through the hottest region of the flame. Once it passes through this region, temperatures may be hot enough to encourage reactions to occur once again. If this occurs downstream of the choked flow region, where flow has returned to a subsonic state, the reactions may have a substantial amount of time to react, leading to higher measured concentrations of NO. This effect may be better combated using a cooled microprobe, or by simply measuring downstream of the pre-heat zone.

In the reaction zone and post-flame zone the trends seem to be much less irregular. The C_3H_8 results show a slight increase from the luminous zone to the post flame zone, and then it slowly decreases further downstream. This is more prevalent in the lean and rich results, but the stoichiometric flame appears to nearly follow this trend. It is believed that the methyl butanoate NO concentrations also follow a similar trend, but there are not enough data points for a visible comparison. As mentioned previously, inadequate fuel availability and time constraints limited the amount of samples that could be obtained for the methyl butanoate flames.

Ignoring the high values of NO concentration near the burner surface, the results of the experiments conducted in this study suggest that there is not a substantial difference in NO formation between the C_3H_8 and methyl butanoate flames. Concentrations for propane are slightly higher in the reaction zone and early post flame zone. Further downstream, the

concentrations for methyl butanoate are nearly the same and are larger by about 0.4 ppm in the rich flame, lower by 1.2 ppm in the stoichiometric flame and lower by 2 ppm in the lean flame. The results for NO are tabulated in the appendix with the rest of the measured concentrations.

It is difficult to determine solely from the experimental results, the contribution of the different pathways which form NO_x. To differentiate between the various mechanisms, more reliable data is needed in the pre-heat region of the flame, and for the different species that lead to NO formation (e.g. prompt NO precursors). The technique used in the present work may not be the ideal method to determine the formation pathways to NO_x since prompt NO precursors are radicals such as CH, C_2 and possibly C_2O. Accordingly, laser induced fluorescence (LIF) is one such technique that could be useful in this determination, because of its ability to take information from the flame without incurring any disturbances and the ability to measure radicals such as CH, C_2 and C_2O. LIF experiments are currently be conducted by our research group at CSU and will be the subject of future studies. Section 4.3.4 briefly discusses the contribution of thermal NO to the overall concentration in the numerically modeled results.

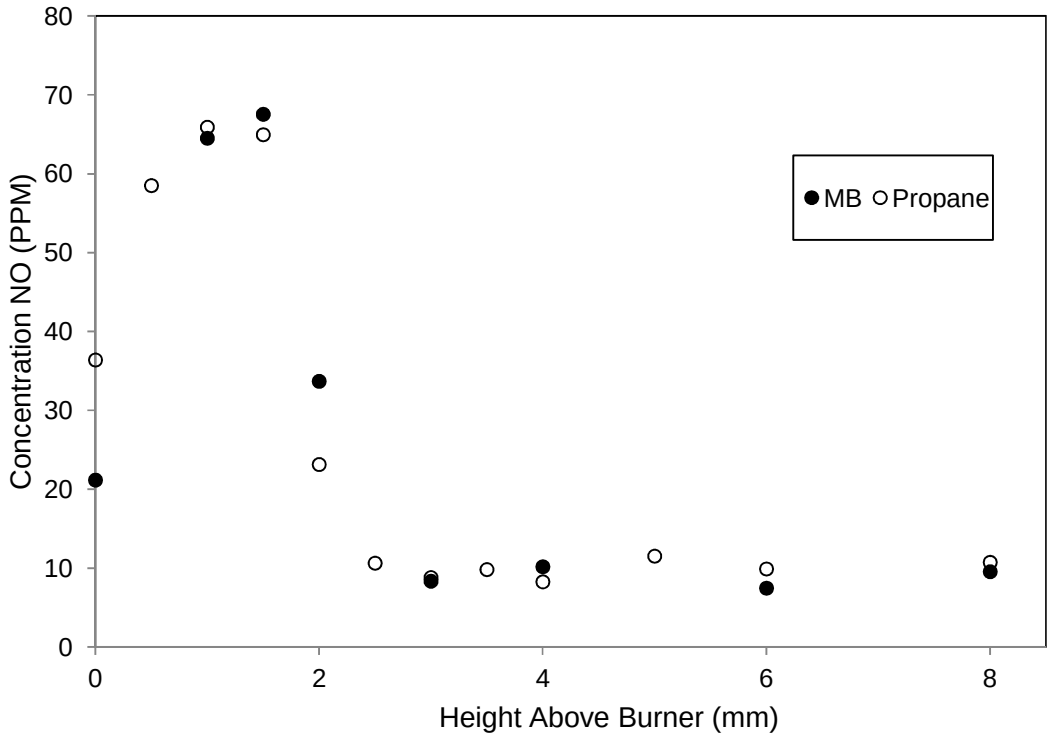

Figure 4-6: NO concentration measurements for the stoichiometric (φ=1.0) $C_5H_{10}O_2$-air and C_3H_8-air flames. The filled in circles (•) represent the data for MB, while the empty circles represent propane results.

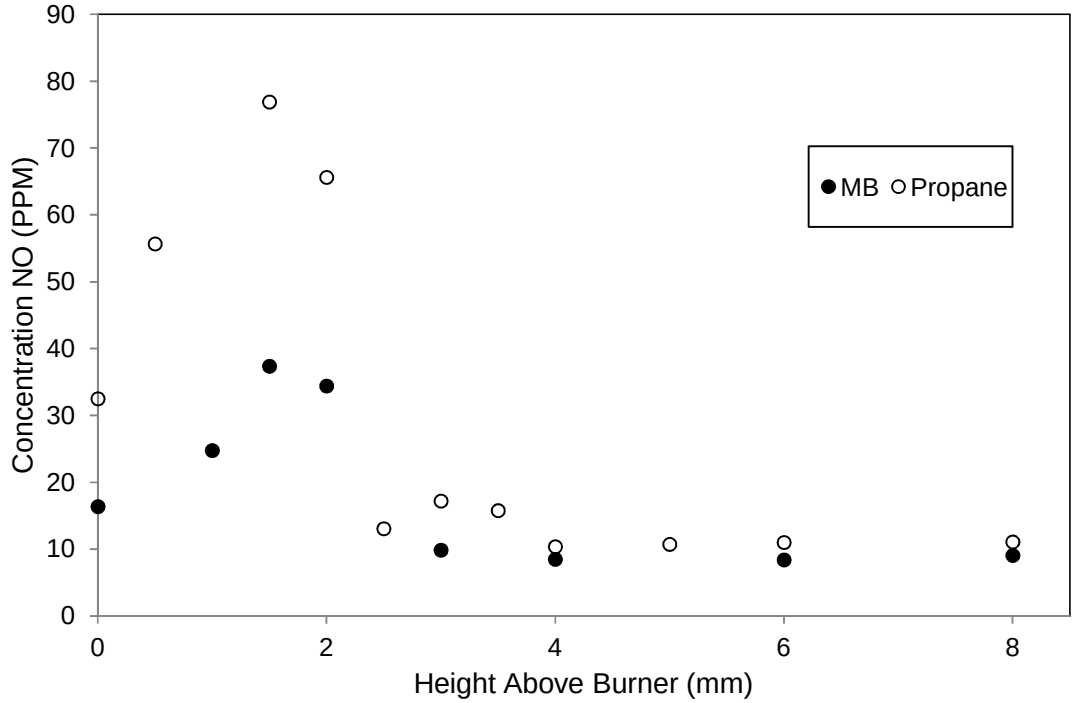

Figure 4-7: NO concentration measurements for the lean (φ=0.8) $C_5H_{10}O_2$-air and C_3H_8-air flames. The filled in circles (•) represent the data for MB, while the empty circles represent propane results.

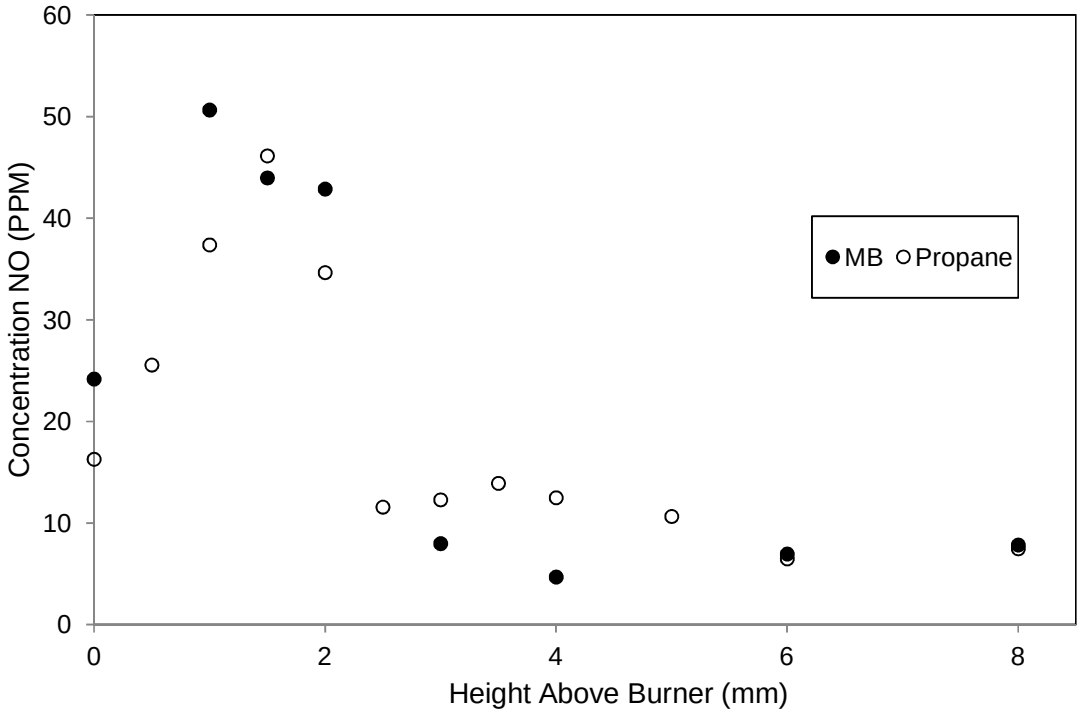

Figure 4-8: NO concentration measurements for the rich (φ=1.2) $C_5H_{10}O_2$-air and C_3H_8-air flames. The filled in circles (•) represent the data for MB, while the empty circles represent propane results.

4.2.2 **Carbon Monoxide and Carbon Dioxide**

The measured results for CO and CO_2 species concentrations obtained by FTIR spectroscopy are presented in figures 4-9 through 4-14. Results for propane and methyl butanoate are plotted together for comparison. Although the main focus of this experiment is a comparison of NO concentrations between the two fuels, CO and CO_2 are important factors in the emission of methyl ester fuels and thus are included in the study. Moreover, CO and CO_2 are useful for direct comparison against numerical modeling.

The stoichiometric results for CO and CO_2 are given in figures 4-9 and 4-10 and are presented as mole fractions versus height above the burner surface in mm. The CO results begin

at lower concentrations near the burner surface, and then increase to a maximum in the reaction zone of the flame. Once in the post-flame zone, the mole fractions begin to decrease as samples are taken further downstream. These results are consistent with that which is expected for CO measurements in premixed laminar flames. The highest levels of CO should be reached in the reaction zone before being converted to CO_2 in the post-flame zone. Surprisingly, the measured CO for the stoichiometric methyl butanoate flame was higher than that for the propane flame. Typically methyl esters produce less CO than typical hydrocarbon flames. It is believed that this result arises from a discrepancy in the equivalence ratio of the methyl butanoate flame. Specifically, the higher CO levels indicate that the methyl butanoate flame might have been slightly richer than stoichiometric.

Measured CO_2 levels were also higher in this instance for the stoichiometric methyl butanoate flame, which also suggests an uncertainty in the equivalence ratio for the methyl butanoate flames. The CO_2 curve begins at its lowest concentration levels and increases steadily until reaction zone. Once at the reaction zone the CO_2 levels sharply increase and continue to increase at locations further downstream. It is expected that once reactions start to diminish the CO_2 mole fraction eventually levels out. From the data, it appears that this begins to occur at approximately 6 mm above the burner surface.

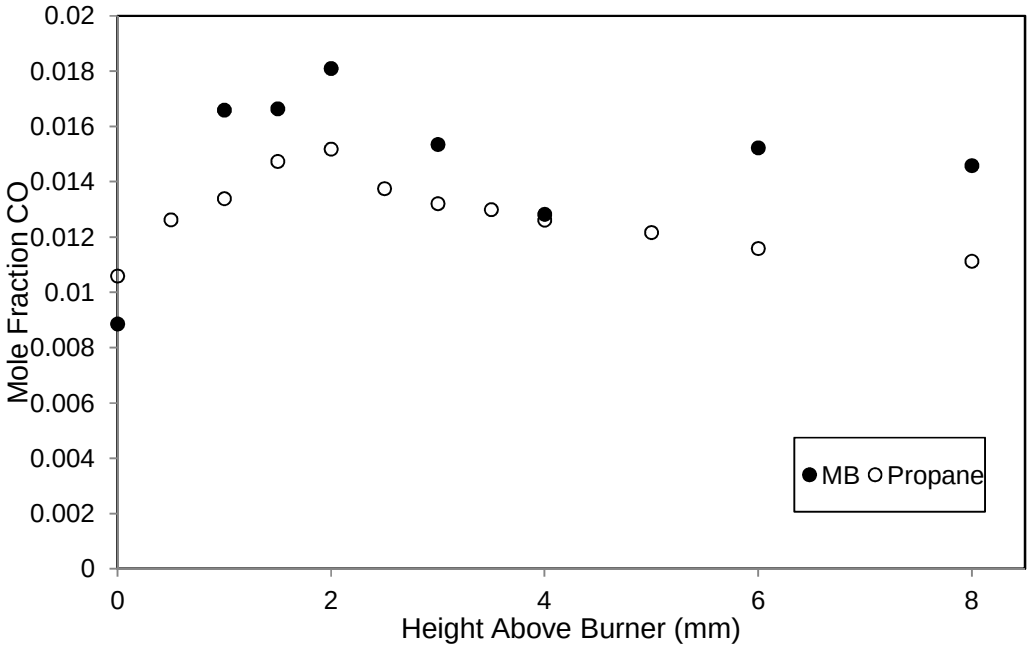

Figure 4-9: Carbon monoxide species concentrations for stoichiometric (φ=1.0) $C_5H_{10}O_2$-air and C3H8-air flames. The filled in circles (•) represent the data for MB, while the empty circles represent propane results.

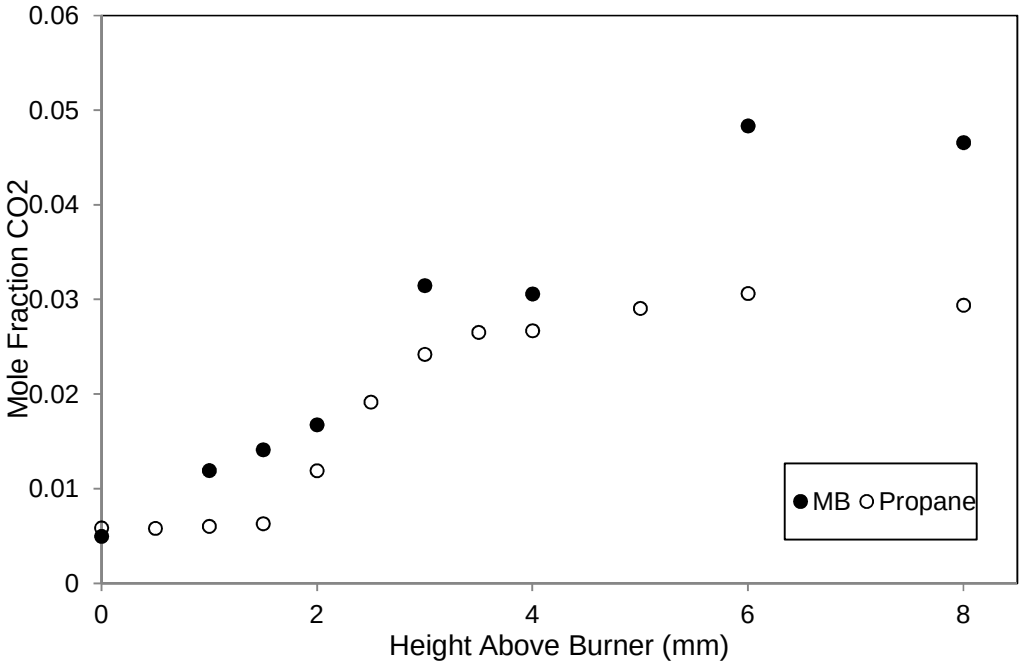

Figure 4-10: Carbon dioxide species concentrations for stoichiometric (φ=1.0) $C_5H_{10}O_2$-air and C3H8-air flames. The filled in circles (•) represent the data for MB, while the empty circles represent propane results.

Figures 4-11 and 4-12 depict the experimentally obtained results for CO and CO_2 mole fractions in the lean flames. The lean data curves for CO follow the same general shape as the stoichiometric results, beginning at the lowest levels nearest the burner surface, then increasing to a maximum in the reaction zone and early post-flame zone, then tapering off once reactions die down and temperatures decrease in the post-flame zone. Overall the CO concentrations for the lean flame are lower than the stoichiometric results. Also, the methyl butanoate produces slightly less CO than the propane flames in the lean case. The CO_2 curves also follow a similar pattern to the previous results, beginning at lower mole fractions in the pre-heat zone, and then significantly increasing in the reaction zone followed by a slow leveling out far downstream of the burner surface. Here CO_2 results for the methyl butanoate flame begin at a lower concentration than the propane flame, but in the post-flame zone the mole fraction for CO_2 produced by methyl butanoate is higher by a mole fraction of 0.004, or 4,000 ppm.

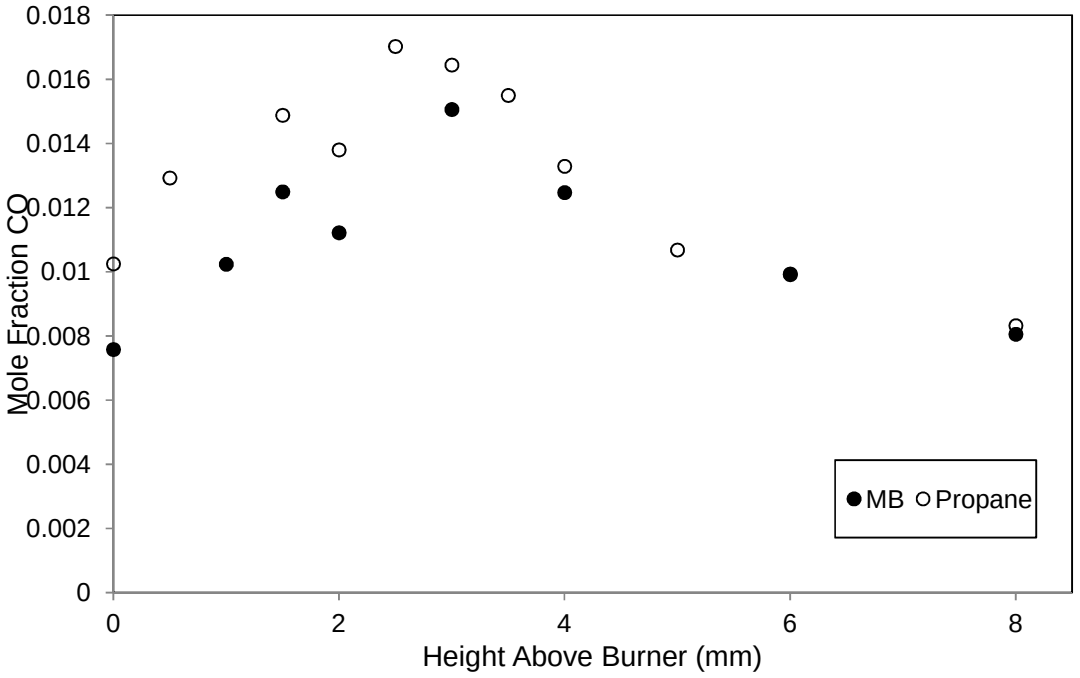

Figure 4-11: Carbon monoxide species concentrations for lean (φ=0.8) MB-air and $C_5H_{10}O_2$-air flames. The filled in circles (•) represent the data for MB, while the empty circles represent propane results.

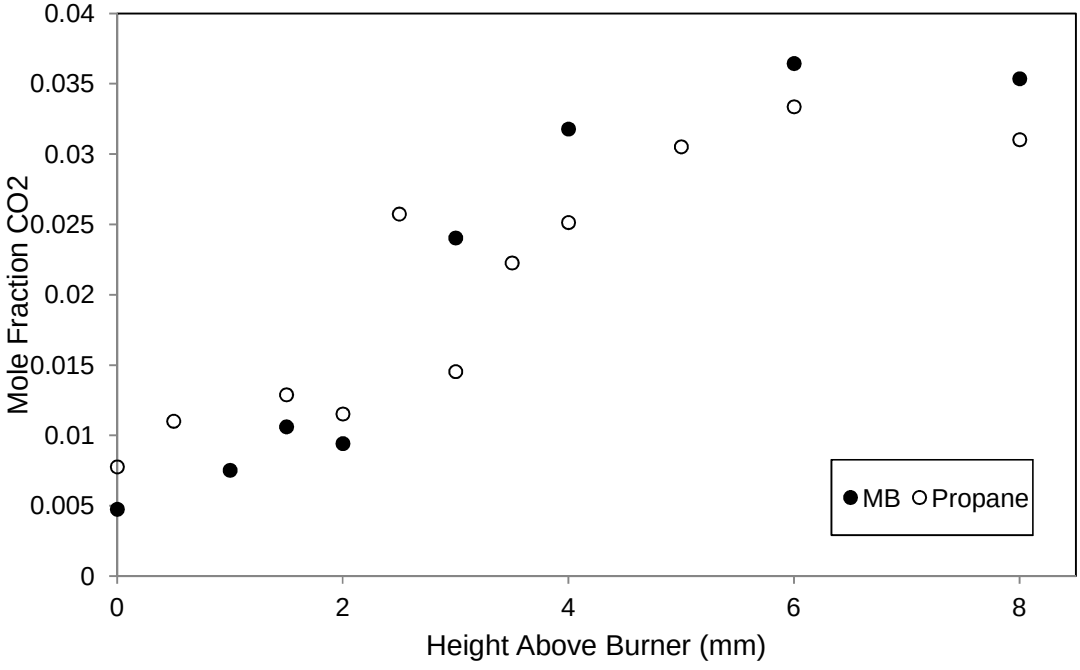

Figure 4-12: Carbon dioxide species concentrations for lean (φ=0.8) $C_5H_{10}O_2$-air and C3H8-air flames. The filled in circles (•) represent the data for MB, while the empty circles represent propane results.

The rich flame results depicted in figures 4-13 and 4-14 again follow curves similar to the previously presented information. CO levels increase as the reaction zone is reached, and decrease once in the post-flame zone. The methyl butanoate CO mole fractions begin at higher concentrations than propane, but decrease more substantially in the post-flame zone, resulting in final lower CO mole fractions. Again, CO_2 increases most substantially in the reaction zone, and then begins to stabilize further downstream. The measured CO_2 for the methyl butanoate flame was found to be higher than that of the propane flame. In the methyl butanoate flame, from the beginning of the reaction zone throughout the post flame zone, the measured value for CO_2 is nearly twice that for propane. This result may originate from an uncertainty in equivalence ratio as mentioned previously; the MB flame could actually be slightly less fuel rich than the propane flame due to issues with the fuel vaporizer. This would lead to more complete concentrations and higher quantities of measured CO_2.

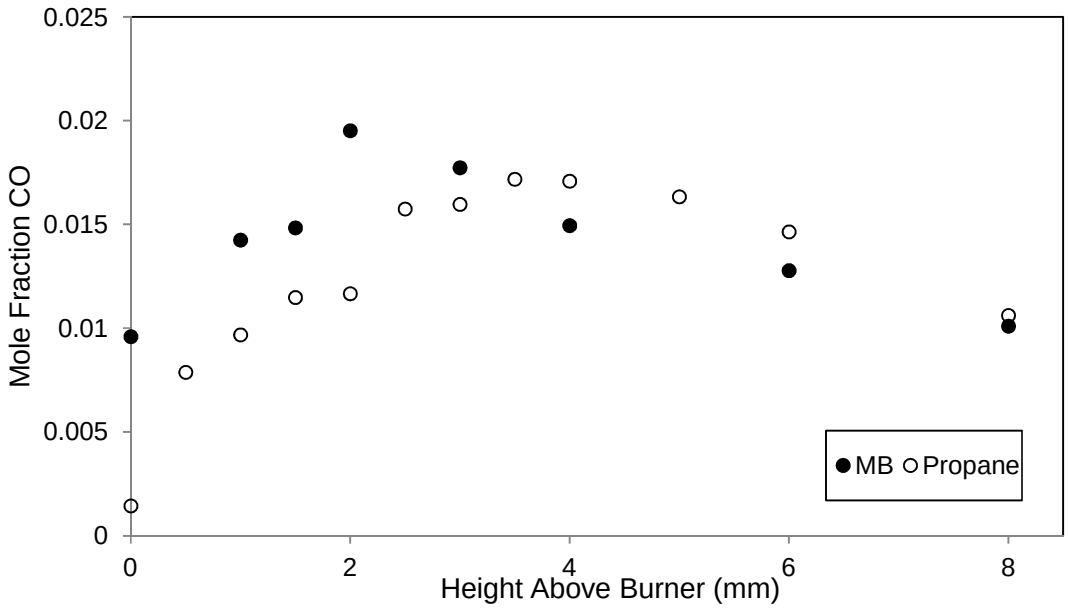

Figure 4-13: Carbon monoxide species concentrations for rich (φ=1.2) $C_5H_{10}O_2$-air and C3H8-air flames. The filled in circles (•) represent the data for MB, while the empty circles represent propane results.

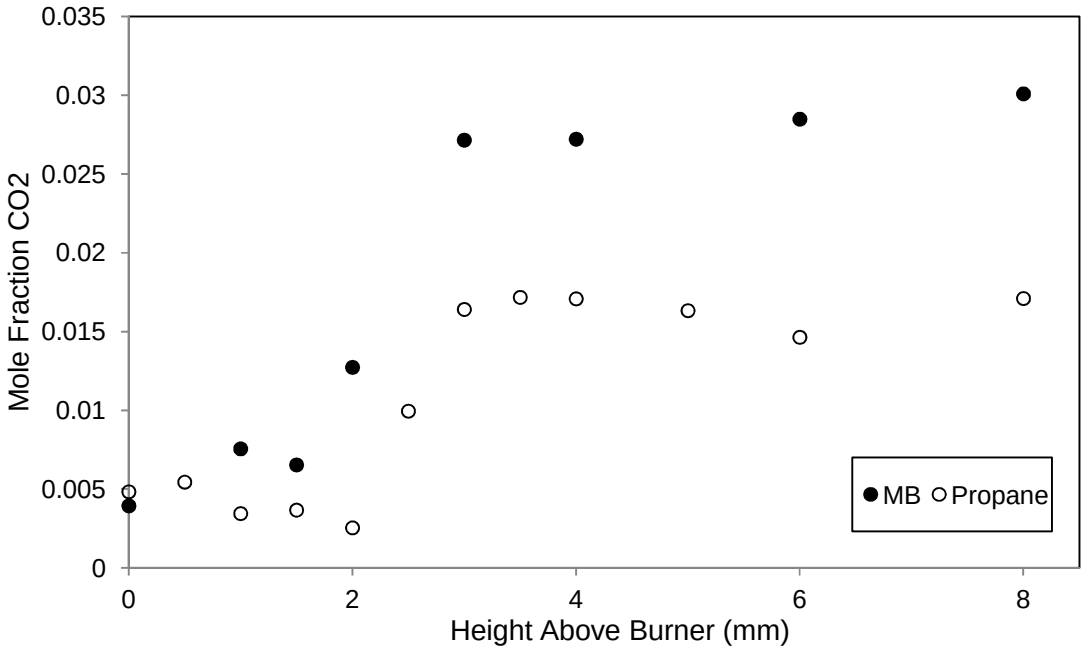

Figure 4-14: Carbon dioxide species concentrations for rich (φ=1.2) $C_5H_{10}O_2$-air and C3H8-air flames. The filled in circles (•) represent the data for MB, while the empty circles represent propane results.

4.3 Comparison of Experimental and Modeling Results

This section presents the calculated results from simulations performed using CHEMKIN (described in chapter 3) along with comparisons against the experimental results. Propane numerical calculations were performed using the small hydrocarbon chemical kinetic model of Konnov [30] which included NO_x chemistry. Numerical calculations for methyl butanoate were performed using a combined mechanism that consisted of the methyl butanoate mechanism of Gail et al and the NOx submechanism of Konnov. The computations were conducted by solving the gas energy equation in all cases except the rich methyl butanoate flame. First, the experimentally obtained temperatures were used as inputs to the fixed gas temperature solution. Then a continuation was run that used the results from the fixed gas temperature solution as an

initial solution to the energy equation, which was then solved numerically. CHEMKIN was unable to find a solution to the gas energy equation for the rich MB flame, so the Gail-Konnov combined model was solved only with the fixed gas temperature option.

First, temperature data are presented and compared, followed by results for concentrations of NO and mole fractions of CO and CO_2. The species results are grouped into methyl butanoate results and propane results, then predicted NO concentrations for all of the flames are presented simply as a comparison between the models. The species data is presented herein with results of standard error calculated from the spectroscopic results. In the FTIR OMNIC software, the standard error for each spectrum is calculated as 1.96 standard deviations from the mean for 256 scans per point. In the current work, the error displayed represents 1 standard deviation (1σ) from the calculated mean value.

4.3.1 **Temperature Data**

As can be seen in figures 4-15, 4-16, and 4-17, the experimental temperatures do not vary substantially from those predicted by the models. For stoichiometric conditions, the results follow the curve characteristic of the temperature profile, beginning at the unburned gas temperature, then increasing rapidly as the reaction zone is approached, reaching a maximum slightly downstream of the reaction zone, then tapering off in the post-flame zone. The MB and propane experimental results peak slightly further from the burner surface and at higher temperatures than the calculated results. The initial rise of the methyl butanoate flame matches the slope of the calculated result almost identically, while the slope for the experimental propane temperatures is not as steep as the calculation. The experimental results decrease slightly as the

height above the burner increases, while the calculated results level off. Overall, the stoichiometric flame temperatures are in good agreement with the model.

Something to note in the temperature curves of the model is the lack of heat loss in the post-flame region. This can be attributed to the exclusion of heat loss in the gas phase in the numerical analysis. The experimental results illustrate a slight decrease in temperature in the post-flame region of the flame. The temperature results are input as a first guess for the gas energy solution, and CHEMKIN iterates for an adiabatic solution to the problem. Because of this, the experimental data maxes out at a higher temperature then slowly drops off due to heat losses, while the adiabatic solution shows lower maximum temperatures with no heat loss in the post-flame region. If the fix gas energy solution had been used, this characteristic reduction in temperature would have been shown by the model. However, the intent of solving the energy equation was to provide a comparison of both temperature and species results generated by the model. With the fix gas temperature solution, the model simply uses the input temperature profile to calculate a solution and the resulting temperature profile is the same. As mentioned, the intent was to compare both temperature and species results. This issue can be further addressed in by performing calculations using both types of solutions in CHEMKIN; the results for the fixed gas temperature solution are presented for the lean and rich cases at the end of this section.

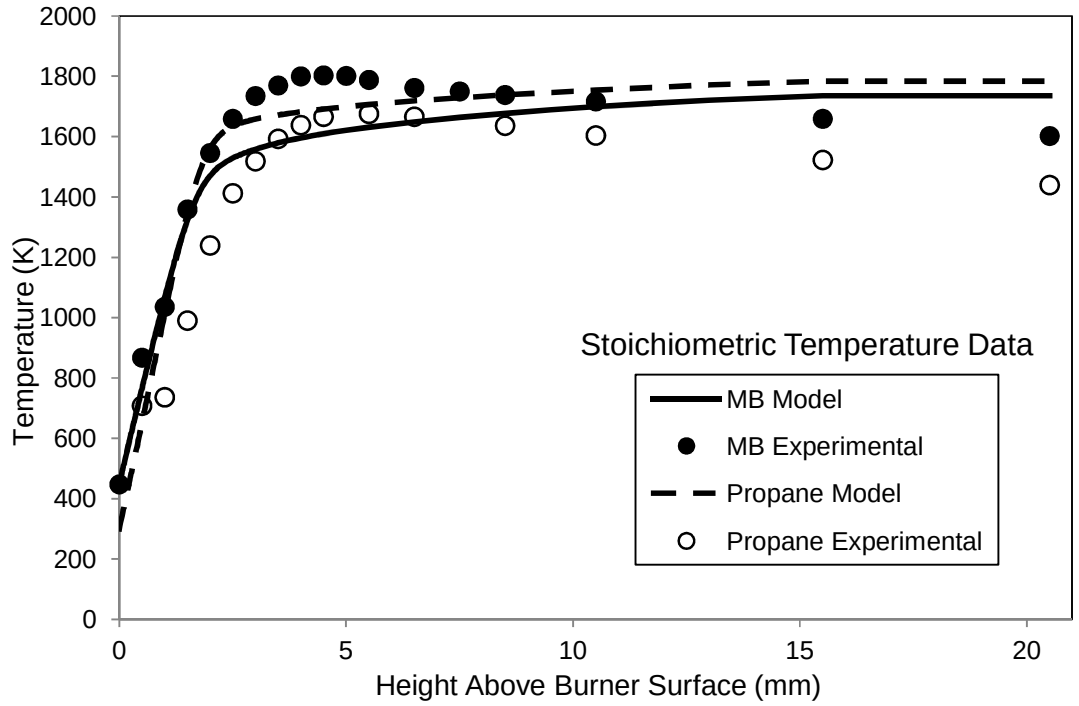

Figure 4-15: Comparison of experimentally obtained temperatures and calculated temperatures from the chemical kinetic mechanism. This plot shows the results for the STOICHIOMETRIC (φ=1.0) $C_5H_{10}O_2$-air and C3H8-air flames. The filled in circles (•) represent experimental data for MB, empty circles represent propane experimental results, the solid line shows calculated temperatures for MB, and the dashed line indicates propane calculated temperatures.

For the lean flames shown in figure 4-16, the methyl butanoate experimental results peak at a slightly higher temperature than the calculated results. Again, the slope of the initial temperature increase is agreeable between the model and experimental results. At the location of the experimental propane peak, the model and the experimental results show nearly the same temperature value. However, the slope of the initial temperature increase does not occur as abruptly as that predicted by the model. Again the experimental temperatures taper off in the post-flame zone, while the calculated temperatures stabilize.

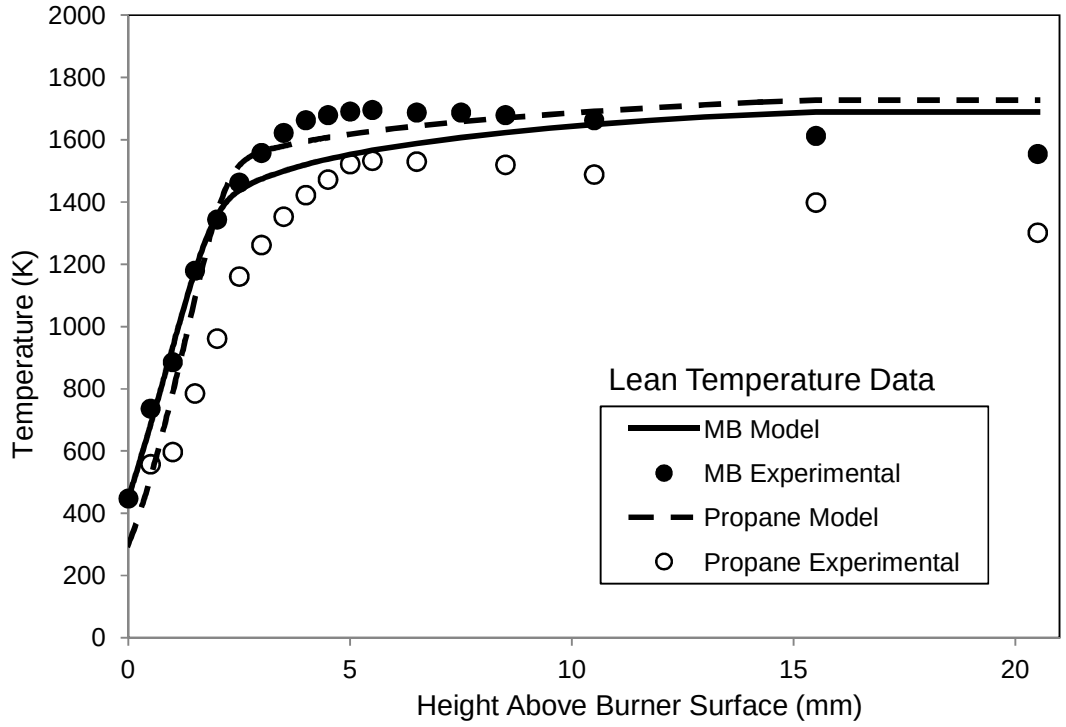

Figure 4-16: Comparison of experimentally obtained temperatures and calculated temperatures from the chemical kinetic mechanism. This plot shows the results for the LEAN (φ=0.8) $C_5H_{10}O_2$-air and C3H8-air flames. The filled in circles (•) represent experimental data for MB, empty circles represent propane experimental results, the solid line shows calculated temperatures for MB, and the dashed line indicates propane calculated temperatures.

For the rich methyl butanoate case, shown in figure 4-17, CHEMKIN was unable to provide a solution to the gas energy equation. Instead, results from the fixed gas temperature model are presented, and the experimental and calculated results line up perfectly. While this result is good, it does not offer a good comparison between the model and experimental temperature data, as all of this information is the same in both cases. The experimental propane temperatures, also shown in figure 4-17, follow the calculated results more closely than in the stoichiometric and lean flames. The slopes are more comparable, and the peak location is nearly the same at about 5 mm above the burner surface. Again, the experimental temperatures

decrease in the post-flame zone while the calculated results do not; this is due to the model performing the calculations in the adiabatic gas phase, as mentioned previously.

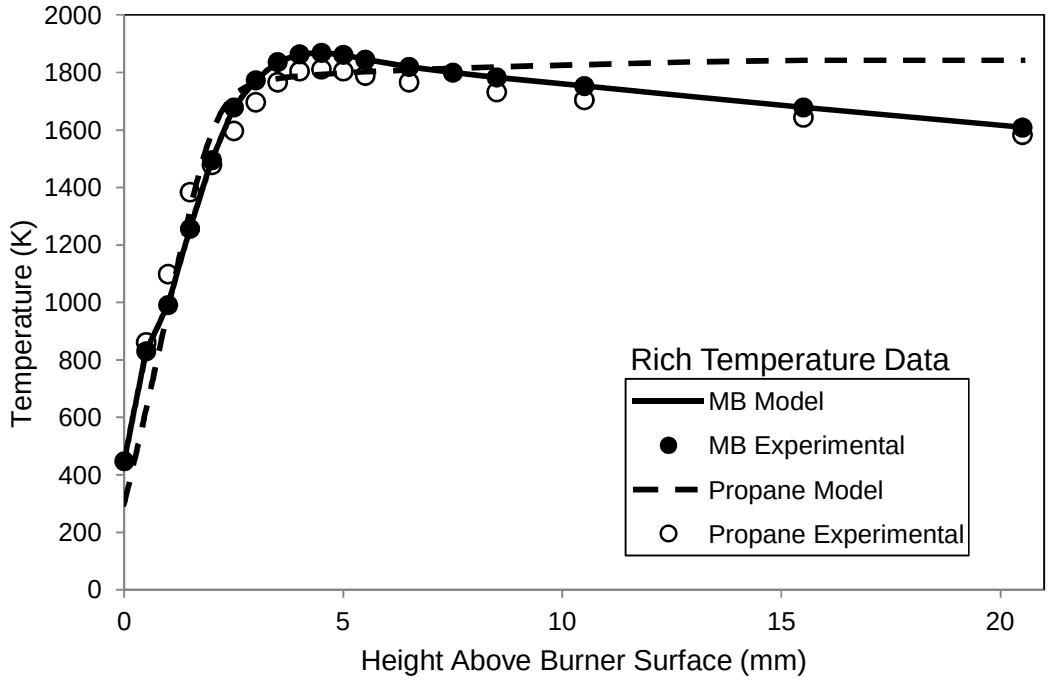

Figure 4-17: Comparison of experimentally obtained temperatures and calculated temperatures from the chemical kinetic mechanism. This plot shows the results for the RICH (φ=1.2) $C_5H_{10}O_2$-air and C3H8-air flames. The filled in circles (•) represent experimental data for MB, empty circles represent propane experimental results, the solid line shows calculated temperatures for MB, and the dashed line indicates propane calculated temperatures.

The decrease in experimental temperatures is a result of heat loss to the flame's surroundings. In the CHEMKIN model, heat loss in the post-flame is not included in the model, which results in the flame temperature increasing monotonically toward a final value. Overall the temperatures calculated from the Konnov mechanism and Gail-Konnov mechanism show good agreement with the experimentally obtained methyl butanoate and propane temperatures for all equivalence ratios tested.

The following figures illustrate the temperatures from fixed gas temperature solution for the lean and rich methyl butanoate and propane compared with the experimental results. It can

be seen that the temperatures for the model exactly follow the temperatures obtained from the experimental data for both lean and rich conditions. The model data follows so closely because the experimentally obtained temperature data was used as an initial input to the model in order to solve for species concentrations in the flame. The fixed gas temperature solution does not assume an adiabatic flame, and therefore shows signs of heat loss as locations higher above the burner surface are reached.

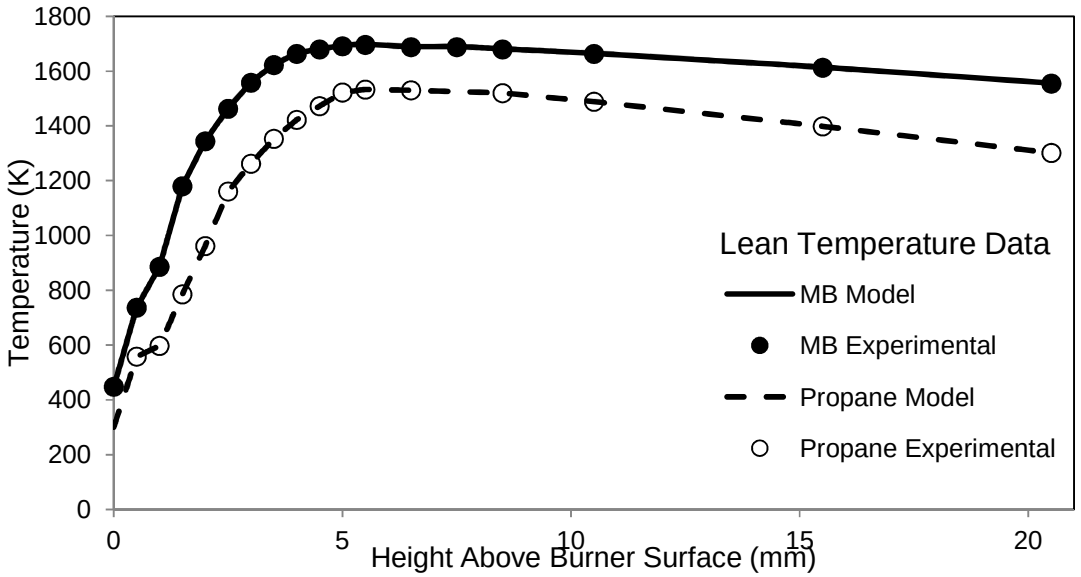

Figure 4-18: Comparison of experimentally obtained temperatures and calculated temperatures from the chemical kinetic mechanism. This plot shows the results for the LEAN (φ=0.8) $C_5H_{10}O_2$-air and C3H8-air flames. The filled in circles (•) represent experimental data for MB, empty circles represent propane experimental results, the solid line shows calculated temperatures for MB, and the dashed line indicates propane calculated temperatures. The results presented here are from the FIXED GAS TEMPERATURE solution.

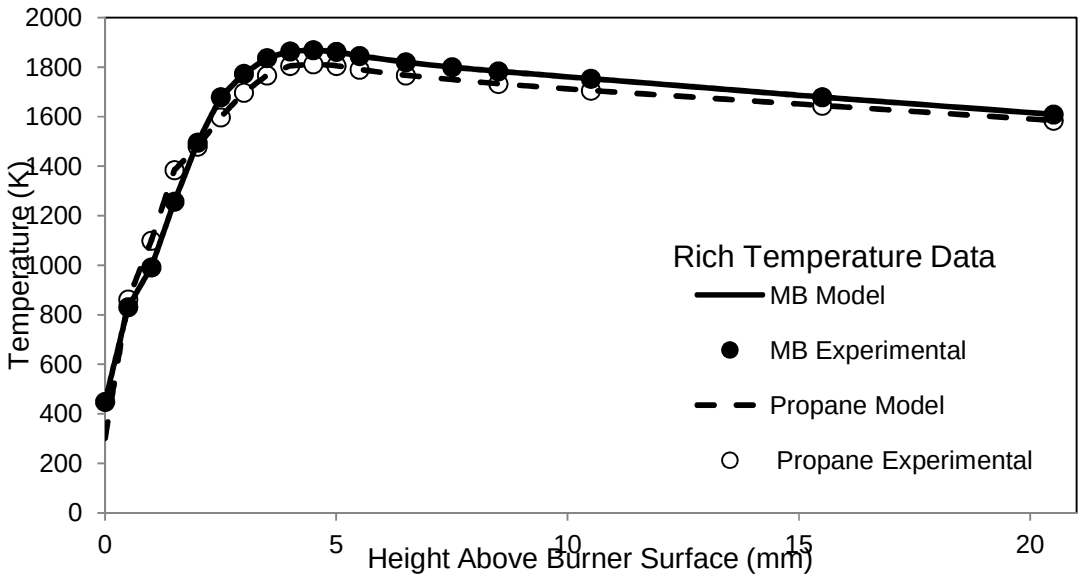

Figure 4-19: Comparison of experimentally obtained temperatures and calculated temperatures from the chemical kinetic mechanism. This plot shows the results for the RICH (φ=1.2) $C_5H_{10}O_2$-air and C3H8-air flames. The filled in circles (•) represent experimental data for MB, empty circles represent propane experimental results, the solid line shows calculated temperatures for MB, and the dashed line indicates propane calculated temperatures. The results presented here are from the FIXED GAS TEMPERATURE solution.

4.3.2 **Methyl Butanoate Species Data**

Figures 4-20, 4-21, and 4-22 show the comparisons between the experimental and calculated results for NO concentrations, and CO and CO_2 mole fractions for the stoichiometric methyl butanoate flames. The calculated data for the methyl butanoate flames resulted from solutions of the combined Gail-Konnov mechanism in CHEMKIN. The modeling data presented in this section results from the gas energy equation solution option in CHEMKIN. Some fixed gas temperature results are shown in section 4.3.4.

The NO concentrations for the experimentally obtained data are substantially larger than that predicted in the model in the pre-heat region of the flame. As discussed previously in section 4.2.1, this is believed to be a discrepancy that results from internal distortions occurring

in the quartz microprobe during sampling. However, as the reaction and post flame zone are approached, the model and experimental data are nearly in agreement. Due to the unreliability of data obtained in the pre-heat zone, between 0 mm to 3.0 mm above the burner surface, the concentrations for NO are not included in the present section for comparison with modeling results. However, the experimental NO concentrations obtained in the pre-heat zone of the flame are presented in the appendices in Tables A-1, A-3, and A-5. The predicted NO concentration from the model is very near the experimental results shown from 3mm to 8 mm above the burner surface. It is reasonable to suggest, that if more data points in the post flame zone were taken that they would also be in close agreement with the model.

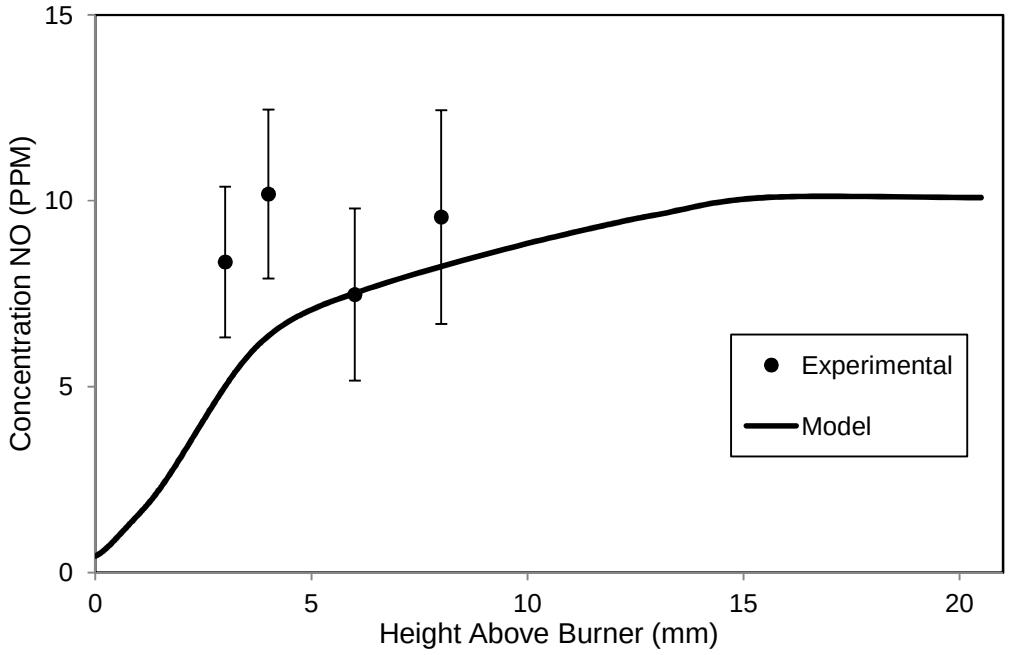

Figure 4-20: Comparison of experimental and calculated results of NO concentrations (PPM) for the stoichiometric (φ=1.0) $C_5H_{10}O_2$-air flame. The filled in circles (•) represent the experimentally obtained data, and the solid line shows the results calculated from the combined Gail-Konnov mechanism. Error bars on the experimental results show 1 standard deviation (1σ) from the mean for 256 scans in the FTIR.

Figures 4-21 and 4-22 show a comparison of the experimentally obtained data and calculated results from the model for CO and CO_2, respectively. In both cases, the mole fractions from the experimental results are substantially lower than what is predicted by the model. The CO data appear to follow a similar curve as the model with an increase from the burner surface to the reaction zone of the flame, followed by a decrease in the post-flame zone. The CO_2 results follow the model curve similarly as well, increasing quickly at the reaction zone and leveling off in the post-flame zone. The stark difference in mole fraction measurements between the model and experiment could result from several influences. Firstly, the model could simply over-predict the CO and CO_2 mole fractions, or it could be further issues occurring in the process of sampling of species, such as recombination on the inside walls of the probe, the absorption for the species could be drowned out by other constituents such as H_2O, or the location for sampling in the spectra may not be ideal. This outcome is present in the results for each of the methyl butanoate flames as well as the propane flames. Another thing to note is that the standard error for CO is relatively small compared to the measured mole fractions, because of this the error bars are so small they do not show up. This is true for all of the CO plots shown in section 4.3.2 and 4.3.3.

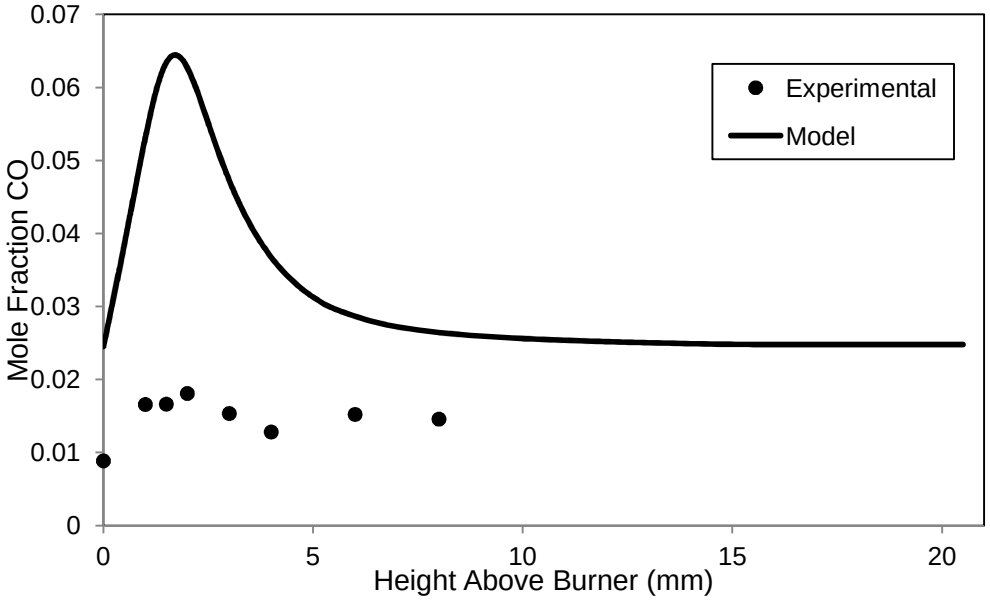

Figure 4-21: Comparison of experimental and calculated results of CO mole fractions for the stoichiometric (φ=1.0) $C_5H_{10}O_2$-air flame. The filled in circles (•) represent the experimentally obtained data, and the solid line shows the results calculated from the combined Gail-Konnov mechanism. Error bars on the experimental results show 1 standard deviation (1σ) from the mean for 256 scans in the FTIR.

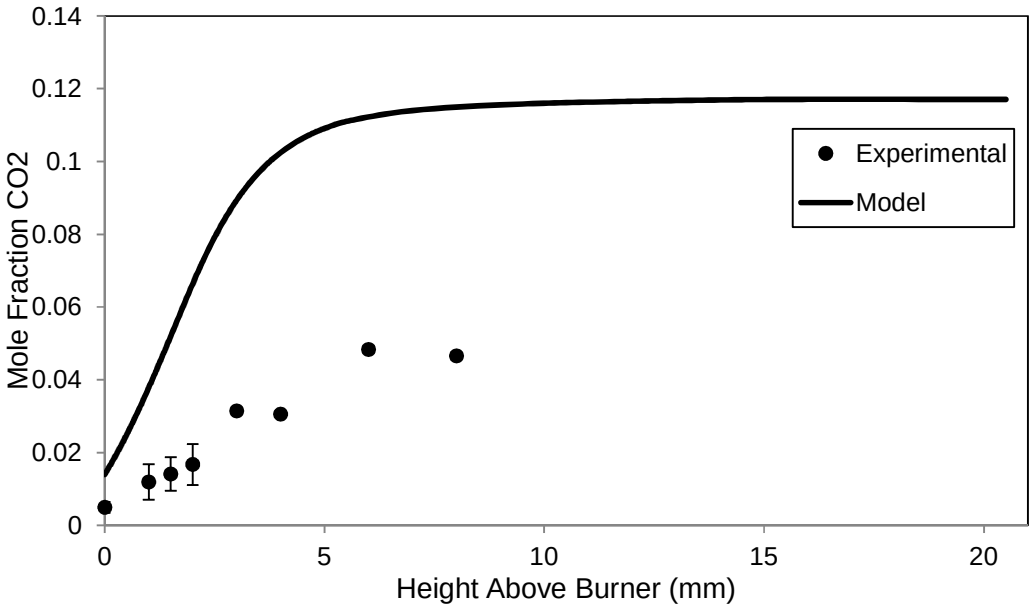

Figure 4-22: Comparison of experimental and calculated results of CO_2 mole fractions for the stoichiometric (φ=1.0) $C_5H_{10}O_2$-air flame. The filled in circles (•) represent the experimentally obtained data, and the solid line shows the results calculated from the combined Gail-Konnov mechanism. Error bars on the experimental results show 1 standard deviation (1σ) from the mean for 256 scans in the FTIR.

Figures 4-23, 4-24, and 4-25 compare the model and experimental results in the lean methyl butanoate flames for NO concentrations (ppm), CO, and CO_2 mole fractions, respectively. The results are very nearly the same as that presented for the stoichiometric flame. Again, the experimental NO is substantially higher than the concentrations predicted by the model in the pre-heat zone. However, the samples taken in the reaction zone and post-flame zone have better agreement with the results predicted by the model. The model appears to under-predict the NO present in the lean flame. CO again follows a similar curve with an increase to a maximum in the reaction zone, then decrease in the post flame zone. CO_2 also follows a curve comparable to the model results, with a quick increase in the reaction zone followed by steadying out in the post-flame zone. The plots again show a considerable difference in the predicted and experimental mole fractions for CO and CO_2.

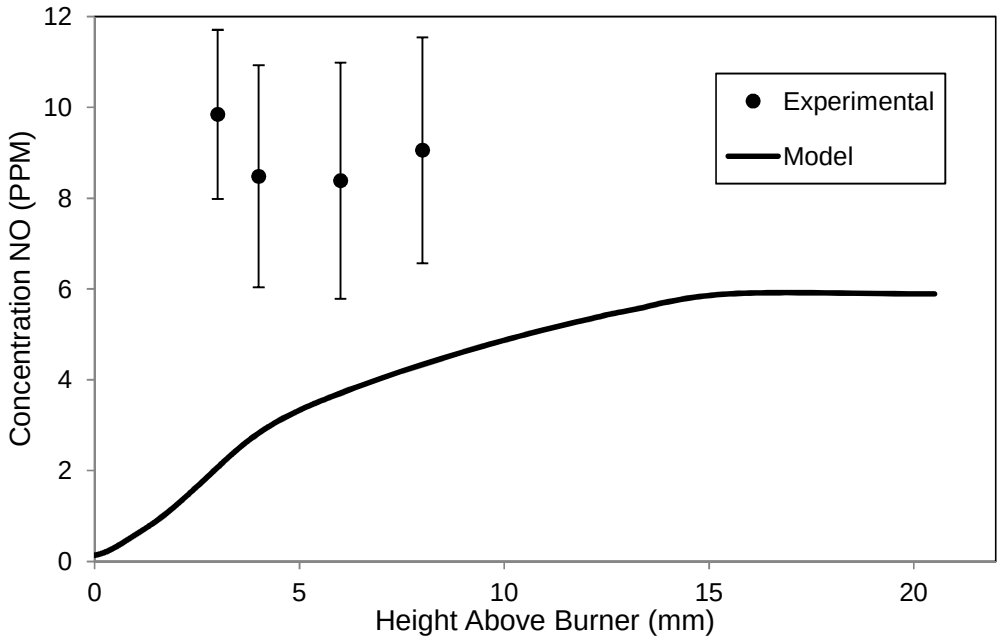

Figure 4-23: Comparison of experimental and calculated results of NO concentrations (PPM) for the lean (φ=0.8) $C_5H_{10}O_2$-air flame. The filled in circles (•) represent the experimentally obtained data, and the solid line shows the results calculated from the combined Gail-Konnov mechanism. Error bars on the experimental results show 1 standard deviation (1σ) from the mean for 256 scans in the FTIR.

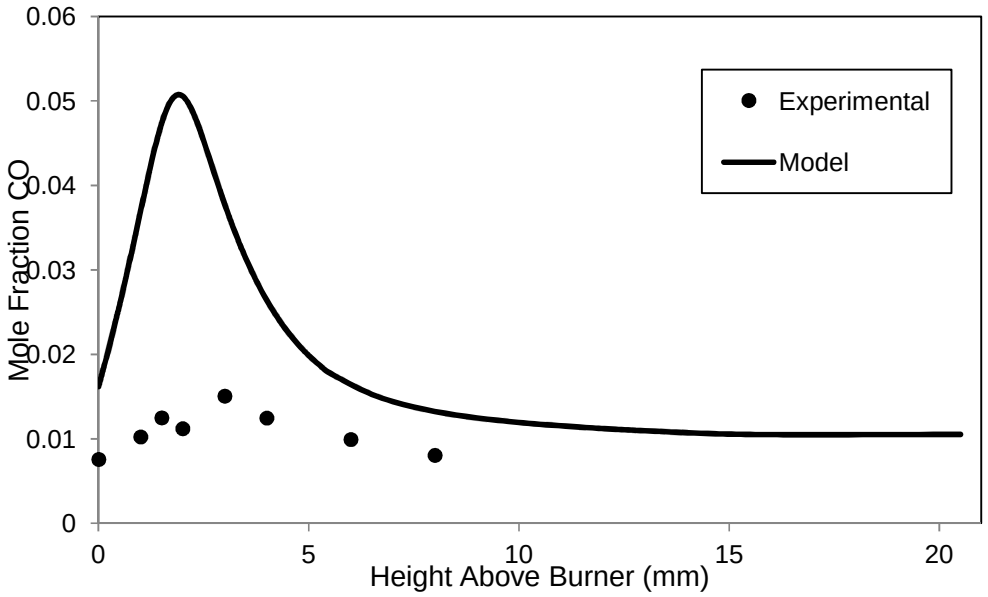

Figure 4-24: Comparison of experimental and calculated results of CO mole fractions for the lean (φ=0.8) $C_5H_{10}O_2$-air flame. The filled in circles (•) represent the experimentally obtained data, and the solid line shows the results calculated from the combined Gail-Konnov mechanism. Error bars on the experimental results show 1 standard deviation (1σ) from the mean for 256 scans in the FTIR.

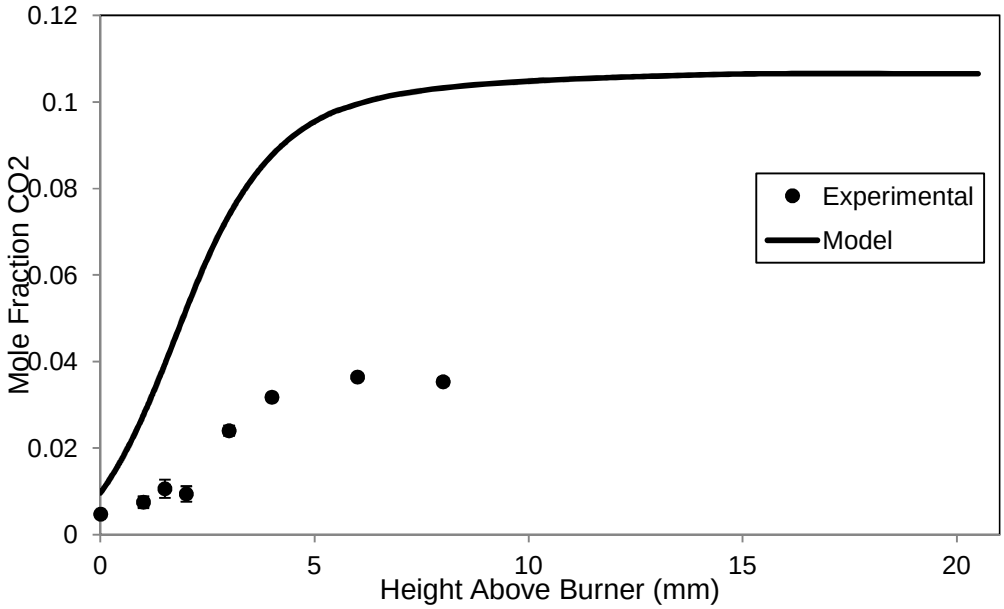

Figure 4-25: Comparison of experimental and calculated results of CO_2 mole fractions for the lean (φ=0.8) $C_5H_{10}O_2$-air flame. The filled in circles (•) represent the experimentally obtained data, and the solid line shows the results calculated from the combined Gail-Konnov mechanism. Error bars on the experimental results show 1 standard deviation (1σ) from the mean for 256 scans in the FTIR.

Figures 4-26, 4-27, and 4-28 compare the model and experimental results in the rich methyl butanoate flames for NO concentrations (ppm), CO, and CO_2 mole fractions, respectively. The experimentally measured NO is again higher than the model prediction in the pre-heat region. However, in this instance the experimental NO is over-predicted by the model in the regions further downstream. CO and CO_2 experimental results again follow curves similar to the calculated mole fractions, but are still substantially lower quantitatively, just as in the stoichiometric and lean methyl butanoate flames. It is somewhat surprising that the experimental results for CO_2 differ greatly from the model calculation for the fix gas temperature solution. It is believed that distortions caused by quartz microprobe may be to blame for these issues. As mentioned in Chapter 2, viscous losses in the probe may be reducing the effectiveness of the probe's ability to quench the combustion products effectively. If the chemical reactions are slowed too quickly, reactions can restart after the quenching process, leading to a completely different composition of species. If viscous losses are indeed the culprit, it is possible that the back pressure of the probe would have to be further reduced from that already employed in the experiment. A possible way to eliminate this type of effect would be to use a slightly larger orifice diameter microprobe for sampling.

Another issue that could potentially contribute to this discrepancy is interference of the species with H_2O in the absorbance spectrum. H2O is a strong absorber with absorbance peaks occur at multiple locations in the spectrum, oftentimes overlapping with peaks of other species including CO_2. It is possible that this could be contributing to the large difference seen between experimental and computational results.

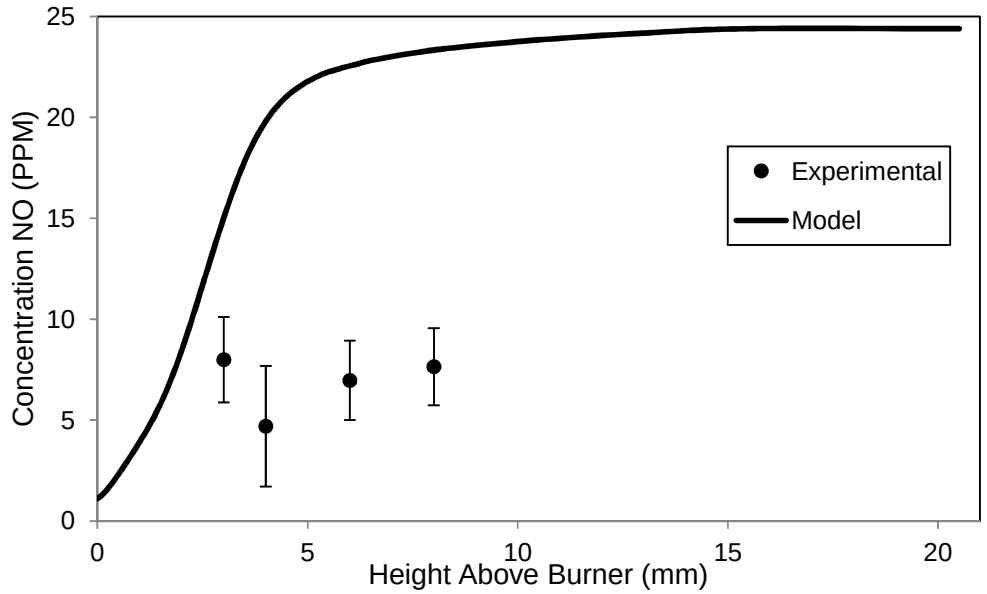

Figure 4-26: Comparison of experimental and calculated results of NO concentrations (PPM) for the rich (φ=1.2) $C_5H_{10}O_2$-air flame. The filled in circles (•) represent the experimentally obtained data, and the solid line shows the results calculated from the combined Gail-Konnov mechanism. Error bars on the experimental results show 1 standard deviation (1σ) from the mean for 256 scans in the FTIR.

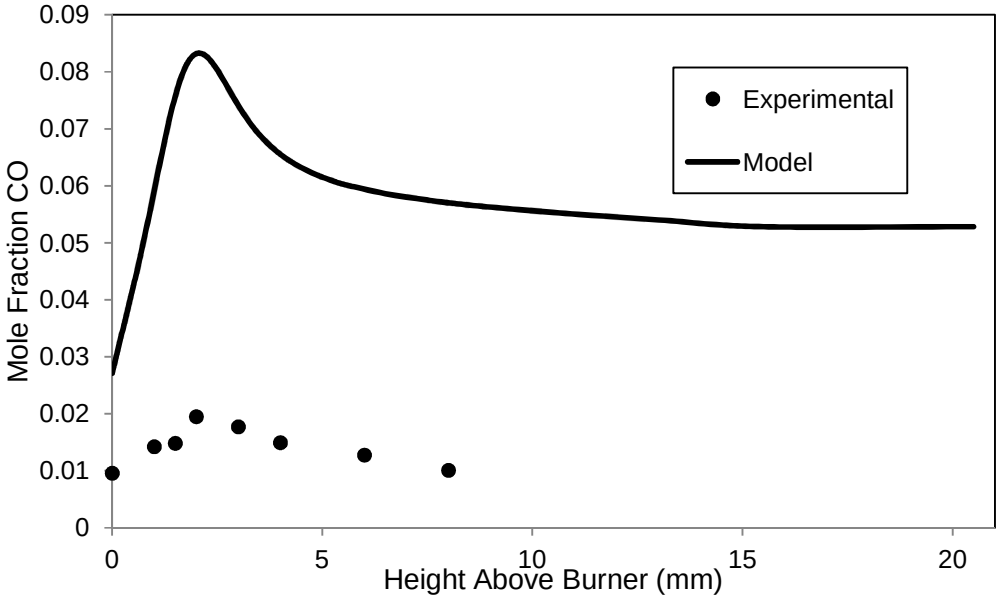

Figure 4-27: Comparison of experimental and calculated results of CO mole fractions for the rich (φ=1.2) $C_5H_{10}O_2$-air flame. The filled in circles (•) represent the experimentally obtained data, and the solid line shows the results calculated from the combined Gail-Konnov mechanism. Error bars on the experimental results show 1 standard deviation (1σ) from the mean for 256 scans in the FTIR.

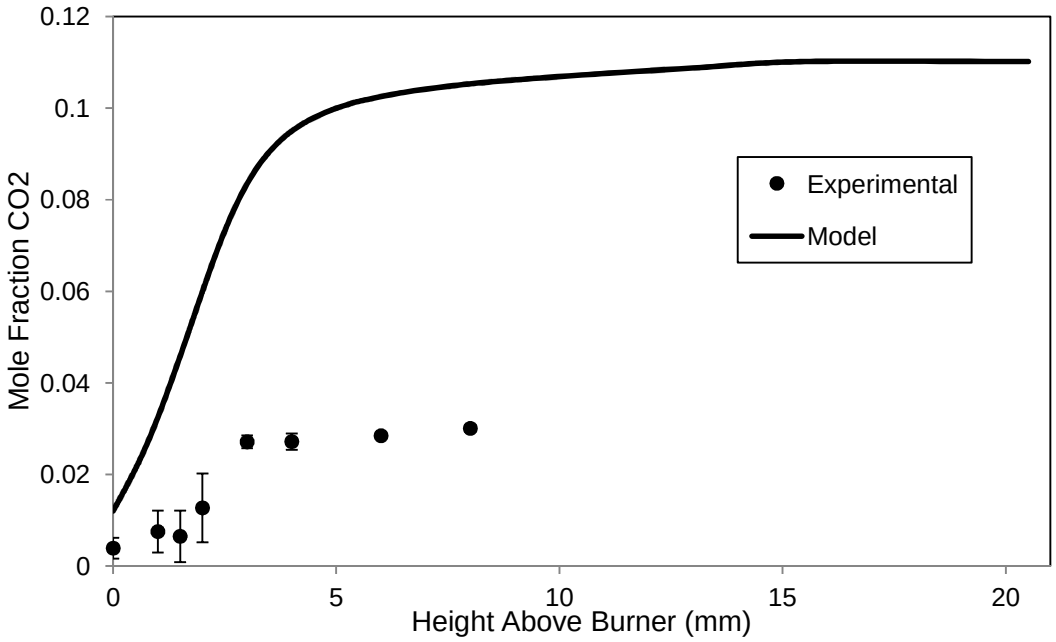

Figure 4-28: Comparison of experimental and calculated results of CO_2 mole fractions for the rich (φ=1.2) $C_5H_{10}O_2$-air flame. The filled in circles (•) represent the experimentally obtained data, and the solid line shows the results calculated from the combined Gail-Konnov mechanism. Error bars on the experimental results show 1 standard deviation (1σ) from the mean for 256 scans in the FTIR.

4.3.3 **Propane Species Data**

Figures 4-29, 4-30, and 4-31 show the comparisons between the experimental and calculated results for NO concentrations, and CO and CO_2 mole fractions for the stoichiometric propane-air flames. The calculated data for the propane flames resulted from solutions of the Konnov mechanism in CHEMKIN.

The stoichiometric results for NO can be seen in figure 4-27, the NO concentrations for the experimentally obtained data are substantially larger than that predicted in the model in the pre-heat region of the flame in the propane cases as well. This is believed to be due to the disturbances incurred by the microprobe. Again, due to the unreliability of data obtained in the pre-heat zone, between 0 mm to 2.5 mm above the burner surface, the concentrations for NO are

not included in the present section for comparison with modeling results. However, the experimental NO concentrations obtained in the pre-heat zone of the flame are presented in the appendices in Tables A-2, A-4, and A-6. As the location in the flame reaches the reaction and post flame zone, the model and experimental data are nearly in agreement. The predicted NO concentration from the model is very near the experimental results shown from 2.5mm to 8 mm above the burner surface. The propane results are consistent with the outcome of the stoichiometric MB model and experimental comparison for the MB flame.

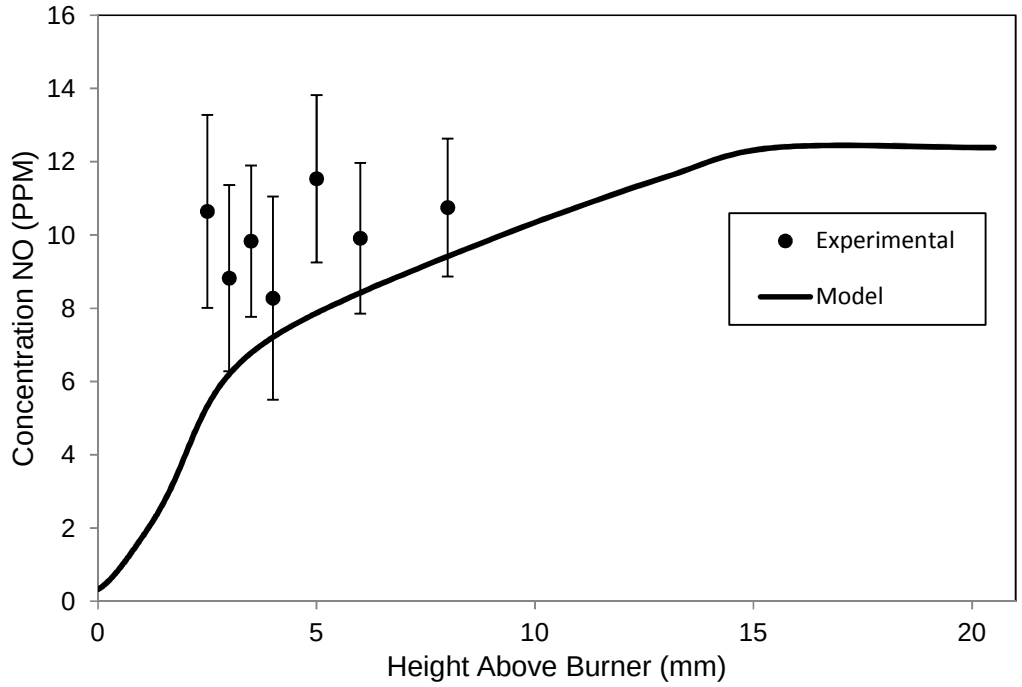

Figure 4-29: Comparison of experimental and calculated results of NO concentrations (PPM) for the stoichiometric (φ=1.0) C_3H_8-air flame. The filled in circles (•) represent the experimentally obtained data, and the solid line shows the results calculated from the Konnov mechanism. Error bars on the experimental results show 1 standard deviation (1σ) from the mean for 256 scans in the FTIR.

Figures 4-28 and 4-29 show a comparison of the experimentally obtained data and calculated results from the Konnov model for CO and CO_2, respectively. In both cases, the mole fractions from the experimental results are substantially lower than what is predicted by the

model. The CO data appear to follow a similar curve as the model with an increase from the burner surface to the reaction zone of the flame, followed by a decrease in the post-flame zone. The CO_2 results follow the model shape also, increasing quickly at the reaction zone and leveling off in the post-flame zone. The model may simply over-predict the mole fractions present in the flame, or an inconsistency arises in sampling.

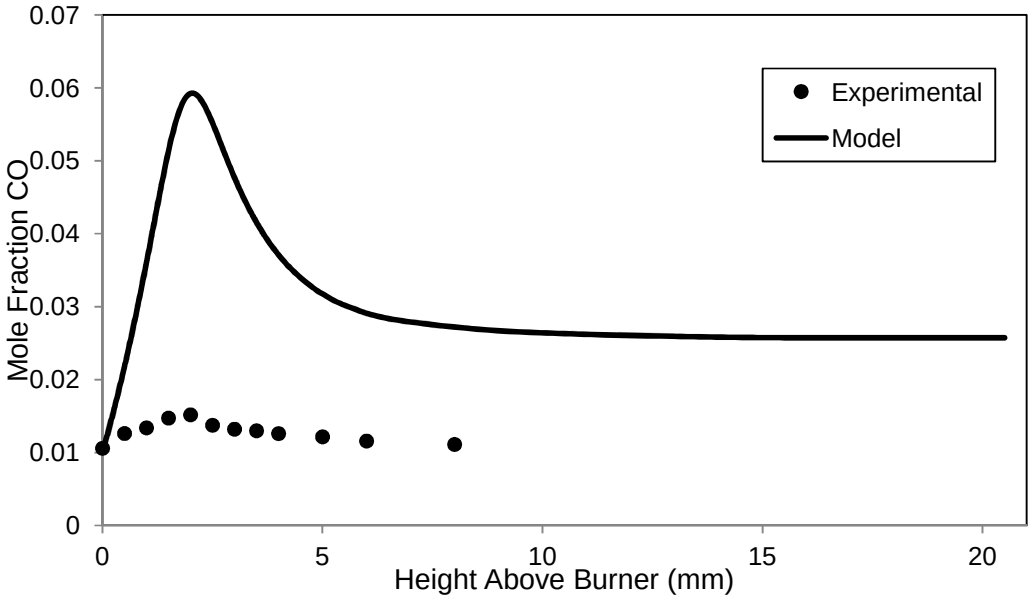

Figure 4-30: Comparison of experimental and calculated results of CO mole fractions for the stoichiometric (φ=1.0) C_3H_8-air flame. The filled in circles (•) represent the experimentally obtained data, and the solid line shows the results calculated from the Konnov mechanism. Error bars on the experimental results show 1 standard deviation (1σ) from the mean for 256 scans in the FTIR.

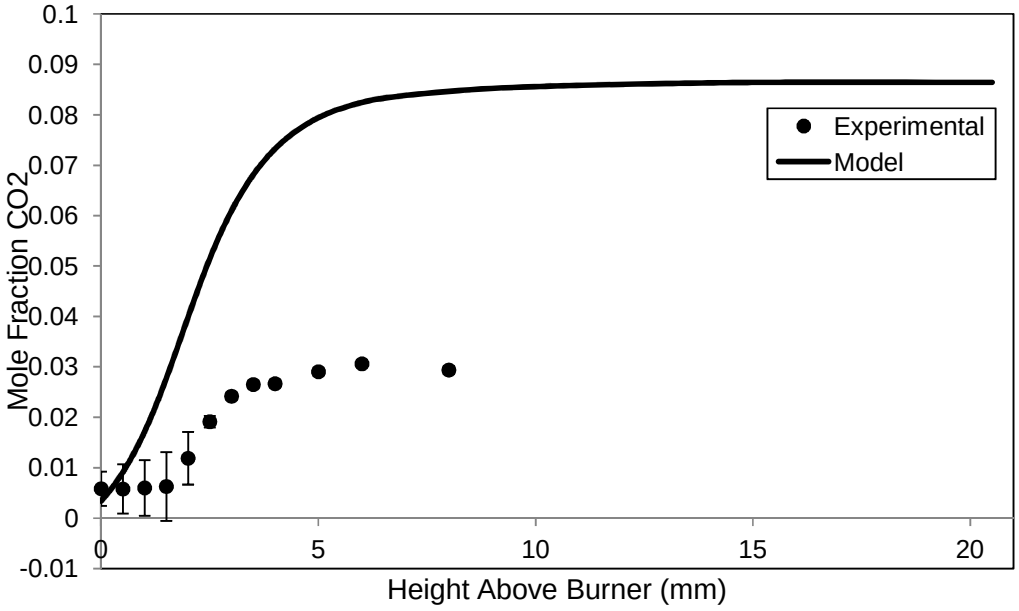

Figure 4-31: Comparison of experimental and calculated results of CO_2 mole fractions for the stoichiometric (φ=1.0) C_3H_8-air flame. The filled in circles (•) represent the experimentally obtained data, and the solid line shows the results calculated from the Konnov mechanism. Error bars on the experimental results show 1 standard deviation (1σ) from the mean for 256 scans in the FTIR.

Figures 4-32, 4-33, and 4-34 compare the model and experimental results in the lean propane flames for NO concentrations (ppm), CO, and CO_2 mole fractions, respectively. Again, the experimental NO is substantially higher than the concentrations predicted in the model in the pre-heat zone, but the samples taken in the reaction zone and post-flame zone have better agreement with the curve produced by the model. The model appears to under-predict the NO produced in the lean propane flame. CO again follows a similar curve with an increase to a maximum in the reaction zone, then decrease in the post flame zone. CO_2 also follows a curve comparable to the model results, with a quick increase in the reaction zone followed by steadying out in the post-flame zone. These plots again show a considerable difference in the predicted and experimental mole fractions for CO and CO_2.

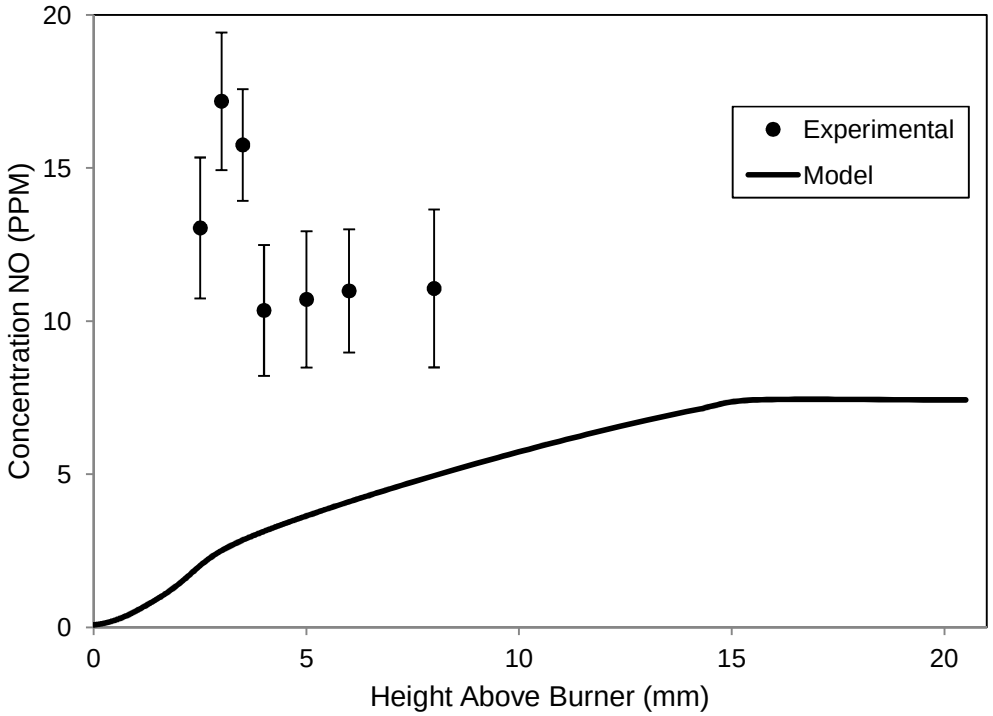

Figure 4-32: Comparison of experimental and calculated results of NO concentrations (PPM) for the lean (φ=0.8) C_3H_8-air flame. The filled in circles (•) represent the experimentally obtained data, and the solid line shows the results calculated from the Konnov mechanism. Error bars on the experimental results show 1 standard deviation (1σ) from the mean for 256 scans in the FTIR.

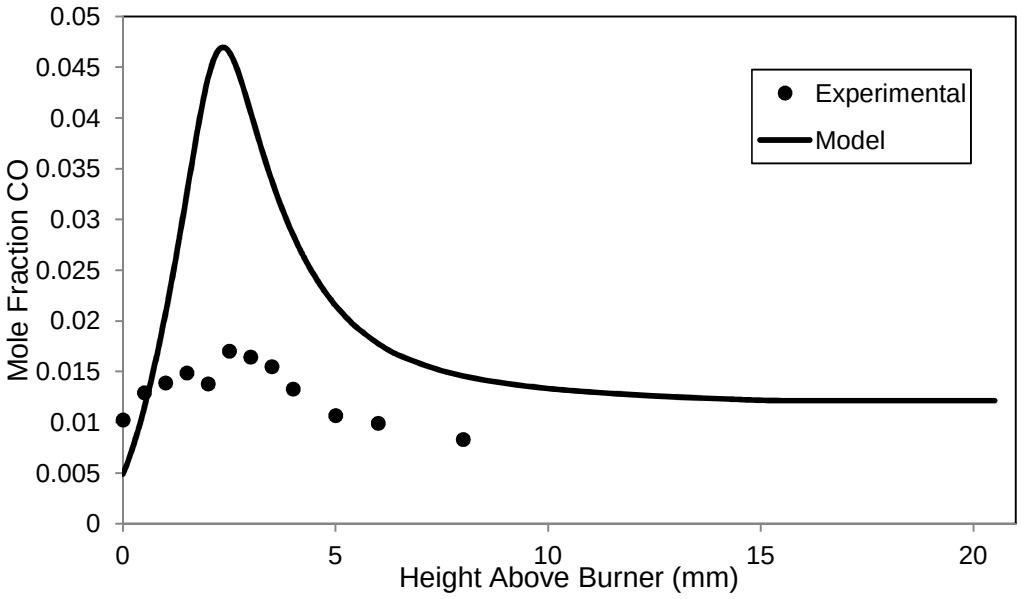

Figure 4-33: Comparison of experimental and calculated results of CO mole fractions for the lean (φ=0.8) C_3H_8-air flame. The filled in circles (•) represent the experimentally obtained data, and the solid line shows the results calculated from the Konnov mechanism. Error bars on the experimental results show 1 standard deviation (1σ) from the mean for 256 scans in the FTIR.

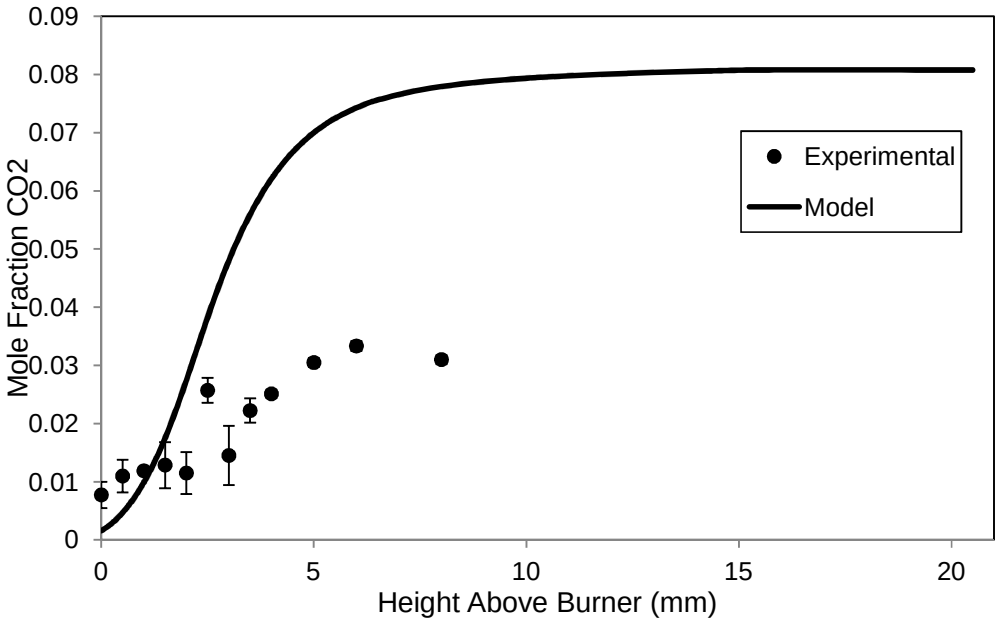

Figure 4-34: Comparison of experimental and calculated results of CO_2 mole fractions for the lean (φ=0.8) C_3H_8-air flame. The filled in circles (•) represent the experimentally obtained data, and the solid line shows the results calculated from the Konnov mechanism. Error bars on the experimental results show 1 standard deviation (1σ) from the mean for 256 scans in the FTIR.

Figures 4-35, 4-36, and 4-37 compare the model and experimental results in the rich propane flames for NO concentrations (ppm), CO, and CO_2 mole fractions, respectively. The experimentally measured NO is again higher than the model prediction in the pre-heat region. However, in this instance the experimental NO is over-predicted by the model in regions further downstream. CO and CO_2 again follow curves similar to the calculated mole fractions, but are still a great deal lower quantitatively, just as for the stoichiometric and lean propane flames.

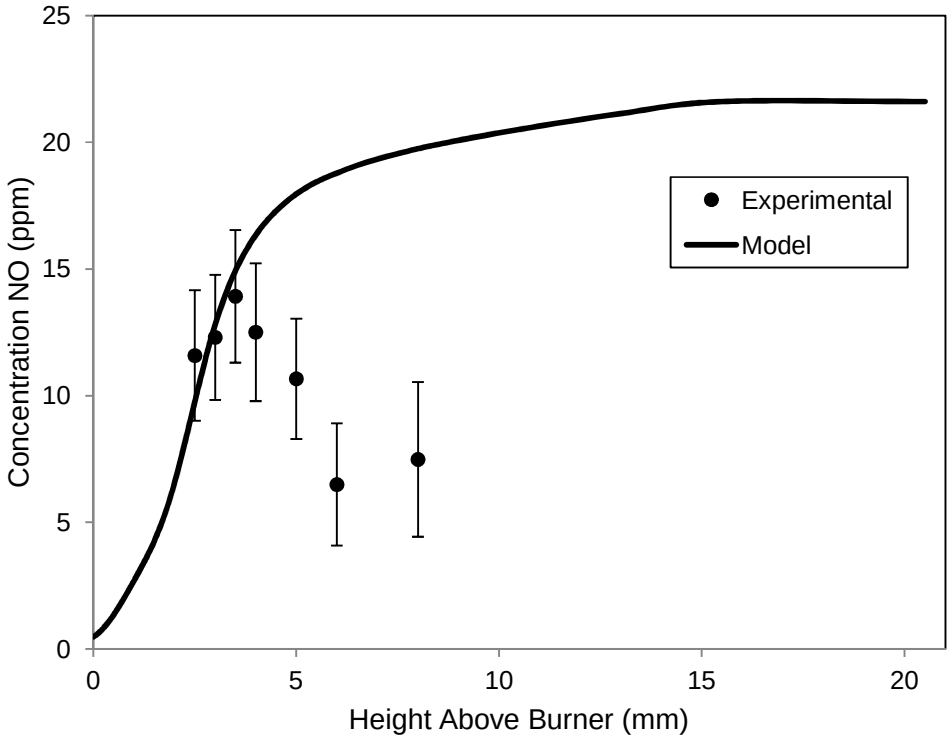

Figure 4-35: Comparison of experimental and calculated results of NO concentrations (PPM) for the rich (φ=1.2) C_3H_8-air flame. The filled in circles (•) represent the experimentally obtained data, and the solid line shows the results calculated from the Konnov mechanism. Error bars on the experimental results show 1 standard deviation (1σ) from the mean for 256 scans in the FTIR.

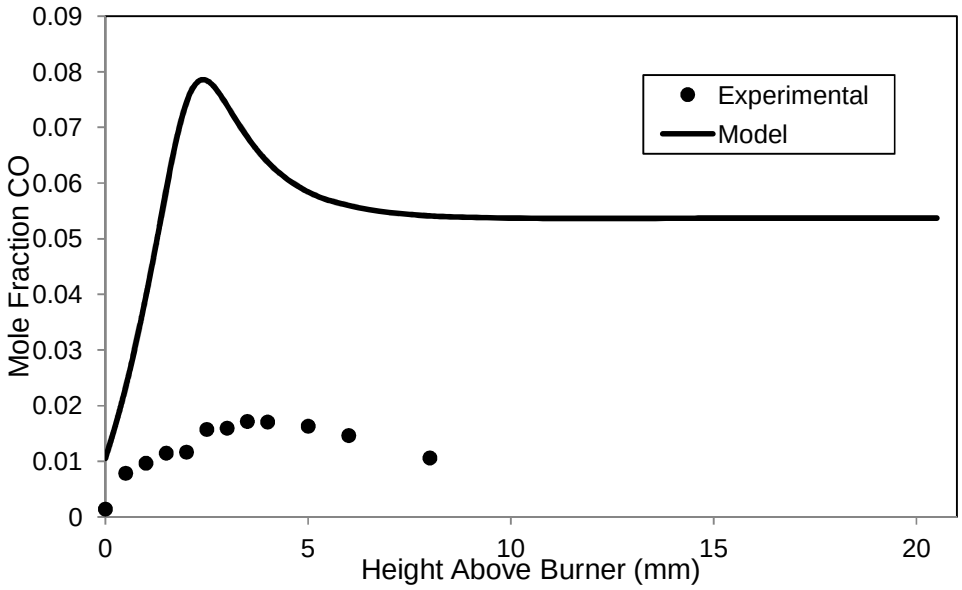

Figure 4-36: Comparison of experimental and calculated results of CO mole fractions for the rich (φ=1.2) C_3H_8-air flame. The filled in circles (•) represent the experimentally obtained data, and the solid line shows the results calculated from the Konnov mechanism. Error bars on the experimental results show 1 standard deviation (1σ) from the mean for 256 scans in the FTIR.

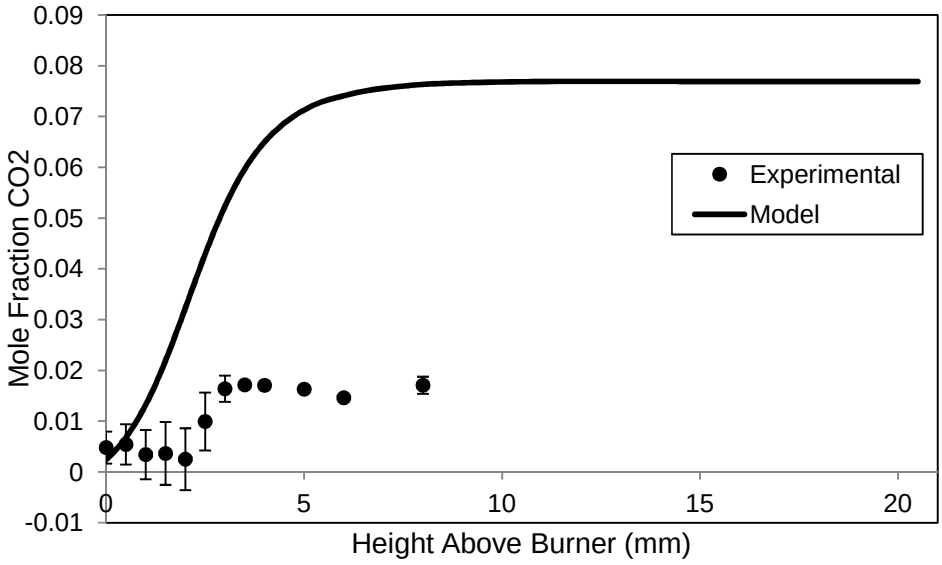

Figure 4-37: Comparison of experimental and calculated results of CO_2 mole fractions for the rich (φ=1.2) C_3H_8-air flame. The filled in circles (•) represent the experimentally obtained data, and the solid line shows the results calculated from the Konnov mechanism. Error bars on the experimental results show 1 standard deviation (1σ) from the mean for 256 scans in the FTIR.

4.3.4 **Species Concentration Data from Fixed Gas Temperature Modeling Solution**

In this section, some results from the fixed gas temperature solution for both rich and lean flames are presented. Stoichiometric results are not included and it is recommended that results for this solution be obtained in the future. The goal of this section is to show that the species concentration results from the fixed gas temperature solution do not substantially differ from the energy equation solution.

First, results for both lean and rich NO concentrations in the methyl butanoate and propane flames are displayed. Just as with the energy equation solution, the modeling results for the lean flames under predict NO concentrations. The rich flames also display similar results, beginning with the model predicting nearly the same concentrations as the experimental results, followed by an over prediction of the NO species concentration by the model.

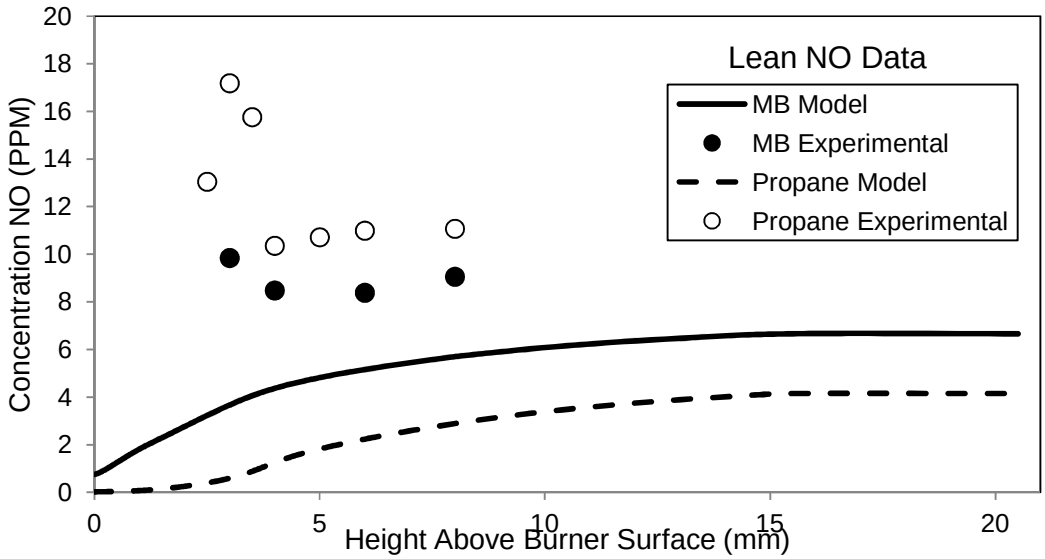

Figure 4-38: Comparison of experimentally obtained and calculated NO species concentrations from the chemical kinetic mechanism. This plot shows the results for the LEAN (φ=0.8) $C_5H_{10}O_2$-air and C3H8-air flames. The filled in circles (•) represent experimental data for MB, empty circles represent propane experimental results, the solid line shows calculated NO for MB, and the dashed line indicates propane calculated NO. The results presented here are from the FIXED GAS TEMPERATURE solution.

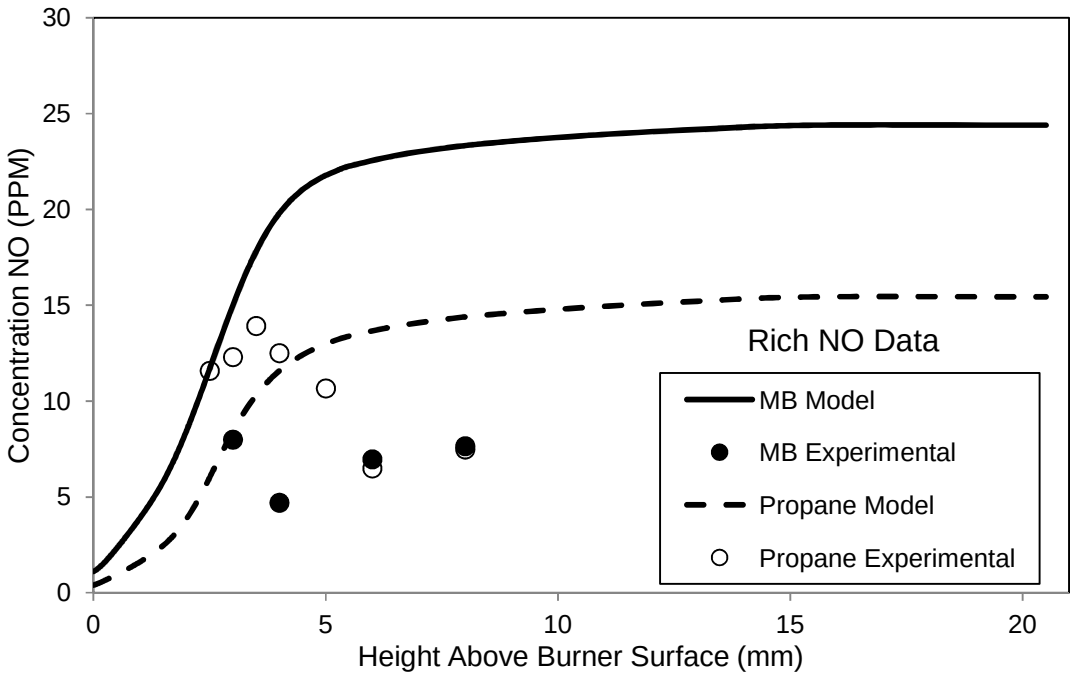

Figure 4-39: Comparison of experimentally obtained and calculated NO species concentrations from the chemical kinetic mechanism. This plot shows the results for the RICH (φ=1.2) $C_5H_{10}O_2$-air and C3H8-air flames. The filled in circles (•) represent experimental data for MB, empty circles represent propane experimental results, the solid line shows calculated NO for MB, and the dashed line indicates propane calculated NO. The results presented here are from the FIXED GAS TEMPERATURE solution.

Figures 4-40, 4-41, 4-42, and 4-43 illustrate the results for CO and CO_2 for the fixed gas temperature solution along with the experimentally obtained results. The data shows that the results for this solution are very nearly the same as for the energy equation solution. In all cases for CO and CO_2, the model determines mole fraction values that are much higher than that obtained in the experimental results. Again, it is believed that the large difference can be attributed to either distortions caused by the microprobe, or by strongly absorbing species, such as H_2O, interfering in the spectra obtained from the FTIR analysis.

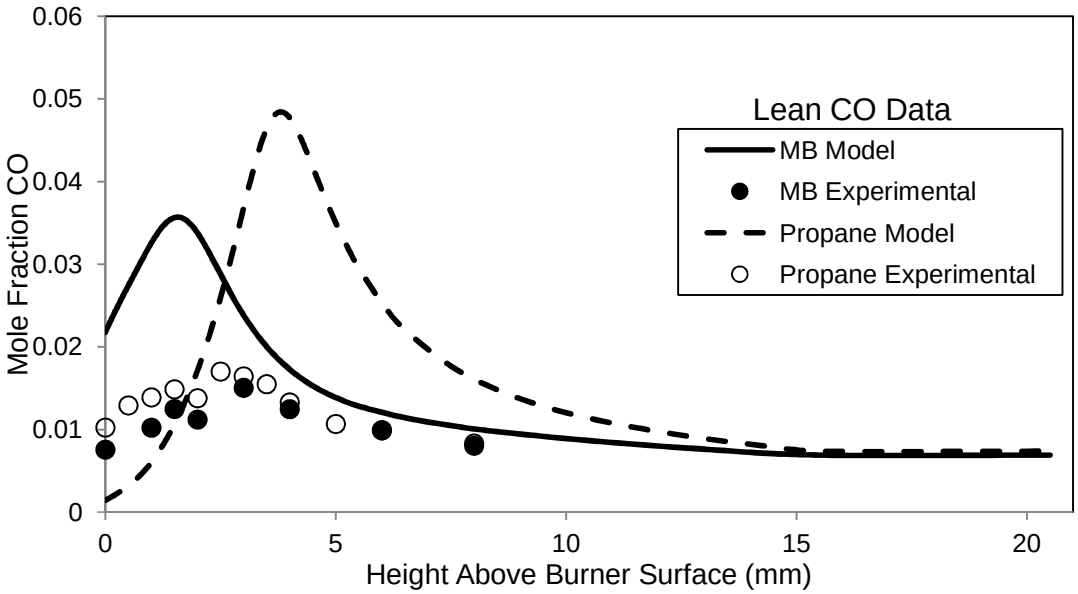

Figure 4-40: Comparison of experimentally obtained and calculated CO species concentrations from the chemical kinetic mechanism. This plot shows the results for the LEAN (φ=0.8) $C_5H_{10}O_2$-air and C3H8-air flames. The filled in circles (•) represent experimental data for MB, empty circles represent propane experimental results, the solid line shows calculated CO for MB, and the dashed line indicates propane calculated NO. The results presented here are from the FIXED GAS TEMPERATURE solution.

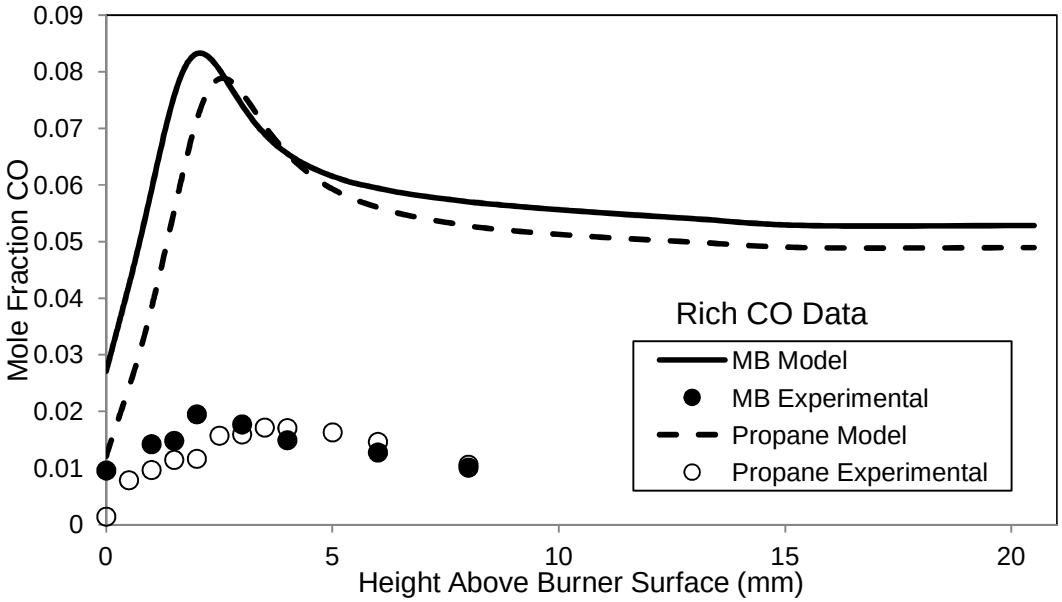

Figure 4-41: Comparison of experimentally obtained and calculated CO species concentrations from the chemical kinetic mechanism. This plot shows the results for the RICH (φ=1.2) $C_5H_{10}O_2$-air and C3H8-air flames. The filled in circles (•) represent experimental data for MB, empty circles represent propane experimental results, the solid line shows calculated CO for MB, and the dashed line indicates propane calculated NO. The results presented here are from the FIXED GAS TEMPERATURE solution.

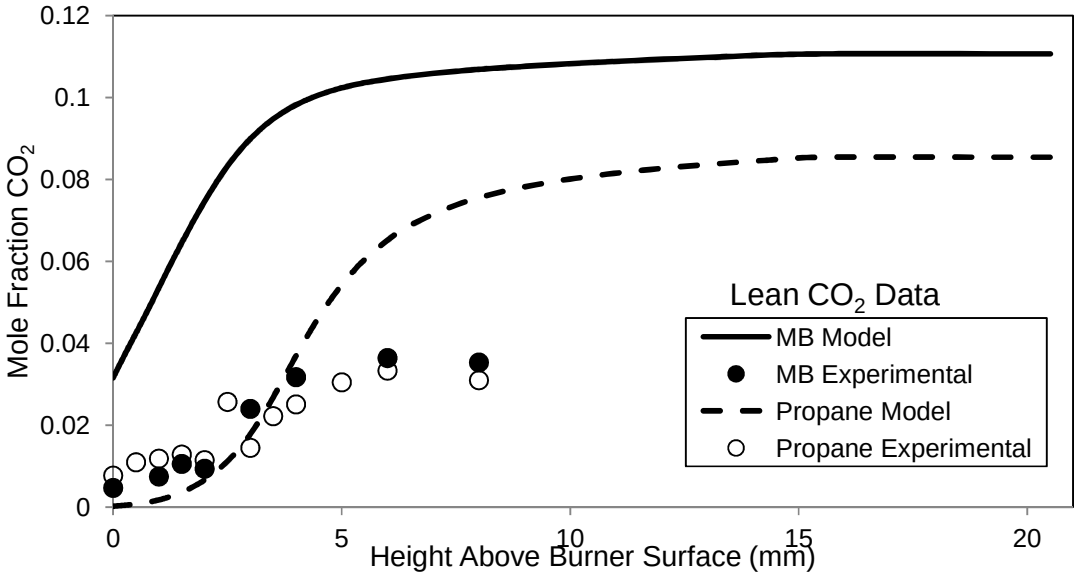

Figure 4-42: Comparison of experimentally obtained and calculated CO_2 species concentrations from the chemical kinetic mechanism. This plot shows the results for the LEAN (φ=0.8) $C_5H_{10}O_2$-air and C3H8-air flames. The filled in circles (•) represent experimental data for MB, empty circles represent propane experimental results, the solid line shows calculated CO_2 for MB, and the dashed line indicates propane calculated NO. The results presented here are from the FIXED GAS TEMPERATURE solution.

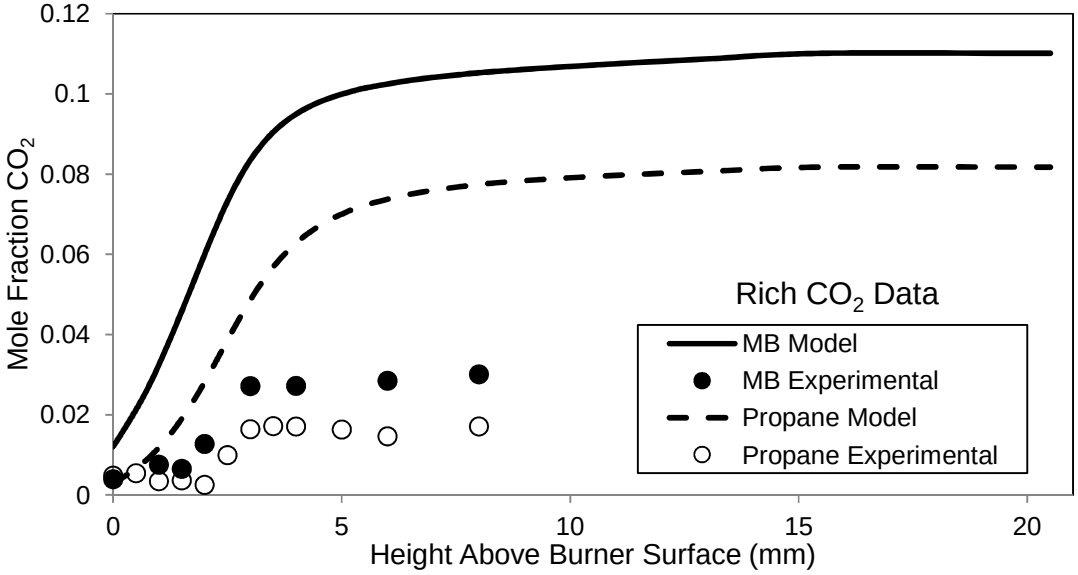

Figure 4-43: Comparison of experimentally obtained and calculated CO_2 species concentrations from the chemical kinetic mechanism. This plot shows the results for the RICH (φ=1.2) $C_5H_{10}O_2$-air and C3H8-air flames. The filled in circles (•) represent experimental data for MB, empty circles represent propane experimental results, the solid line shows calculated CO_2 for MB, and the dashed line indicates propane calculated NO. The results presented here are from the FIXED GAS TEMPERATURE solution.

4.3.5 **Calculated NO Concentration Profiles**

Figure 4-44 illustrates the NO concentration results predicted by each of the models. For the stoichiometric flame and lean flames, the predicted NO concentration level is lower for the methyl-butanoate flames than the propane flames. The maximum predicted value for the stoichiometric and lean MB flames are 10 ppm and 5.9 ppm, respectively; while the propane flames predict maximums of 12.4 ppm and 7.4 for the stoichiometric and lean flames. The Gail-Konnov model predicts a higher NO concentration for the rich MB than the rich propane flame, with maximums of 24.4 ppm for the former and 21.6 ppm for the latter. The difference between the propane and methyl butanoate flames is not substantial, only varying by a few ppm.

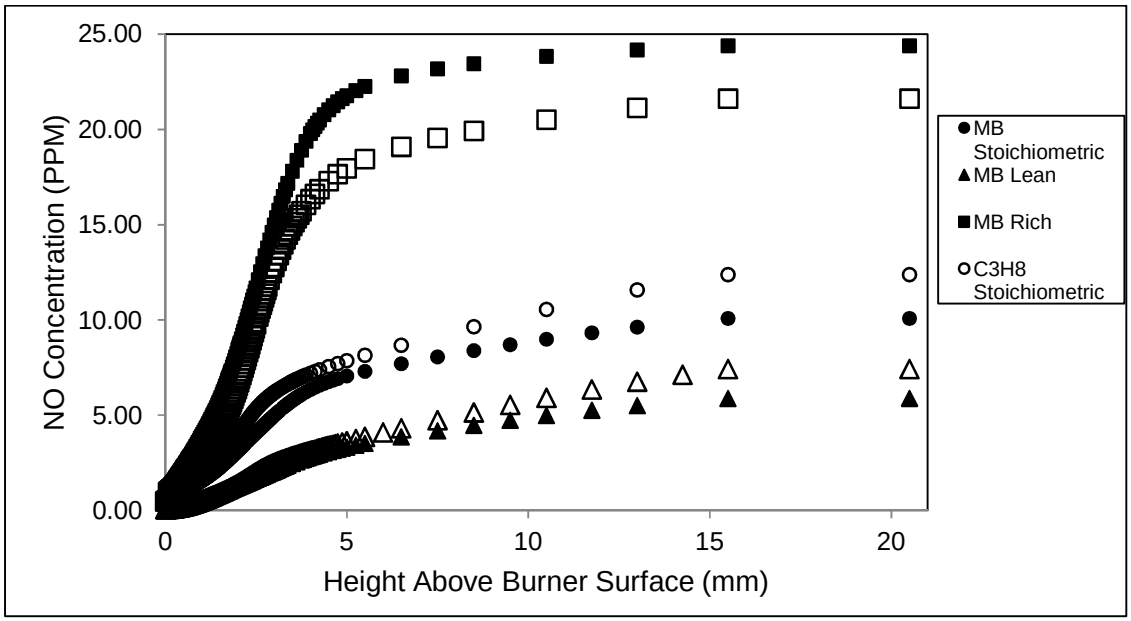

Figure 4-44: Calculated NO concentration (ppm) results for all flames from the Konnov and combined Gail-Konnov mechanism for propane and methyl butanoate, respectively. All flames, save for the rich methyl butanoate flame were solved using the solve gas energy equation. The rich MB flame used the fixed gas temperature solution.

The models also predict when and how much thermal NO_x production takes place in the combustion processes. The results in figure 4-45, originate as a solution variable in the model and are presented as a percentage of the total NO produced by the model calculations. This information is presented here for reference only, to illustrate that the thermal route is not the only NO contributor, nor is it necessarily the largest in the hottest regions of the flame. For each of the flames, thermal NO_x production does not contribute to the overall NO_x concentrations until the reaction zone of the flame, which begins between 1.9 mm and 3.5 mm above the burner surface. Before temperatures become substantially high, it is believed that prompt NO_x is the main contributor to NO concentrations prior to the reaction zones presented in figure 4-44. From the simulation data presented in figure 4-45, it appears that a large portion of the NO produced in the flame is formed through the thermal route, however it does not account for all NO predicted by the model. Other routes that may contribute are the prompt and fuel routes. In the hottest regions of the flame, the fuel route is a likely contributor, which takes place when fuel intermediates containing nitrogen undergo the oxidation process.

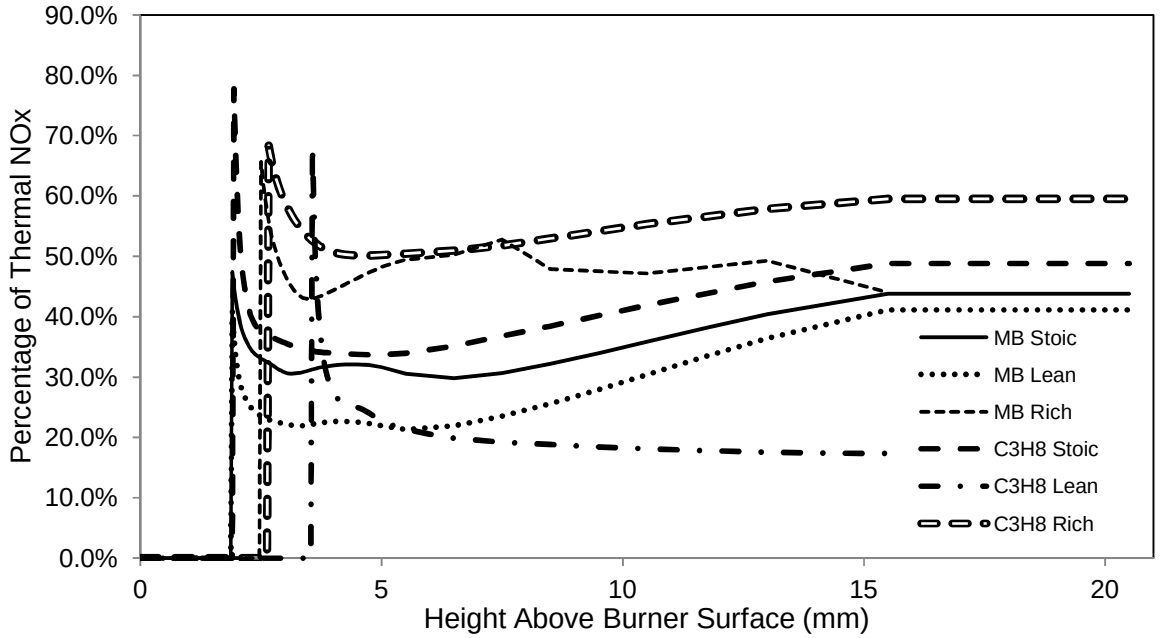

Figure 4-45: Percentage of thermal NOx contribution predicted by the models.

5. Conclusion and Future Work

The objective of this thesis was to compare hydrocarbon fuel and methyl ester fuel nitric oxide emissions of low pressure flat flames for lean (φ=0.8), stoichiometric (φ=1.0), and rich flames (φ=1.2). No conclusive results exist that describe whether nitric oxide emissions for methyl ester flames increase over use of typical petroleum based fuels. It is generally believed, however, that the nitric oxide emissions typically increase for methyl ester fuels due to effects such as higher combustion temperatures, and higher cetane numbers than with traditional fuels. Information was presented about the various formation pathways for NO, including the thermal, prompt and fuel routes. All of these contribute to NO formation in the methyl ester flames at different locations in the flame, and in differing quantities depending on the stoichiometry of the flame.

The flat flame burner apparatus used in the present work was essential in obtaining experimental data in the different regions of the flame, including the pre-heat zone, reaction zone, and post-flame zone. The low pressure in which the experiment was performed allowed for better spatial resolution of these zones. The burner proved to be efficient in its ability to produce a stable and uniform flame. The propane flames were much simpler to keep steady because of the gas form of the fuel. When methyl butanoate was used as a fuel, it was necessary to vaporize the fuel before it entered the burner premixing chamber. Various difficulties arose that contributed to instabilities in the flame stoichiometry, and the vaporizer apparatus was modified to include a valve that increased residence time in the vaporization chamber. This allowed for a more uniform flow of fuel and air, as well as a more stable and consistent flame.

It is recommended that future endeavors spend more time to develop the vaporizer into a more reliable apparatus. Because the pump used for fuel delivery is reliant on the pressure

differential across the upstream and downstream sides of the pump, it may be beneficial to incorporate pressure gauges on either side to better understand the differential pressure and the amount of fuel actually flowing to the vaporization chamber. Implementing yet another pressure gauge downstream of the vaporization chamber and upstream of the valve used to increase the residence time of the flow may also be beneficial. Pressure gauges may also help the user to understand why the equivalence ratio drifts so much over time. While it was helpful to incorporate a thermocouple to make temperature measurements, it is believed that this was not sufficient enough to ensure that the equivalence ratio remained steady.

It would also be beneficial to incorporate different fuel-air stream conditions than those used in the present work in order to achieve more consistent and reliable results between the two fuel types. Ideally, the inlet temperatures of the mixtures should be held at the same temperature and varied in order to keep the flame temperatures constant for each stoichiometry for both the methyl butanoate and propane flames. However, due to time constraints, this was not performed in the present work. Another option is to introduce an inert gas to the flame, such as argon, in order to produce identical temperature results between the two fuels. By varying the level of inert gas introduced, the methyl butanoate and propane flame temperatures could be held constant, allowing for more comparable species concentration results.

The quartz microprobe used as the sampling apparatus performed sufficiently well, but issues arose with disturbances in the pre-flame zone. The possible disturbances that may contribute to inconsistencies in data included those that were external and internal in nature. The results obtained for NO concentrations from the pre-heat zone, do not follow a curve characteristic of a typical flat flame. The measured NO concentrations in the pre-heat zone are high relative to those in the reaction and post-flame regions where the NO concentrations should

reach their maxima. It is believed that these higher concentrations result from internal distortions caused by the probe. The sample is most likely quenching sufficiently at the orifice of the probe, however once the flow in the probe slows again and enters the higher temperature zone of the flame, the temperatures in the probe are potentially hot enough to start combustion reactions all over again. Because the flow is much slower at this location in the probe, more time is available for the constituents to react and thus may lead to higher concentrations of NO. The implementation of a water-cooled probe may be beneficial in negating this effect, but the size of the probe may increase substantially due to this addition and may result in the occurrence of external disturbances. LIF would be a more reliable technique for sampling in the pre-heat region of the flame, due to the lack of a physical probe presence in the flame. LIF, with proper calibration, also has the capability to measure species such as radicals in addition to the stable species present in flames.

Although quenching is not expected to be a problem in the present study, it may be practical to implement an apparatus to verify that flow is choked. For example, Nogueira [47] incorporated a volumetric flowmeter, a bubble flowmeter to be exact, to measure the flow in a microprobe to ensure that the orifice flow was choked rather than just relying on the low downstream pressure in the probe. He determined that once the orifice flow was choked, the volumetric flow rate does not vary with a further decrease in back pressure.

Once the flow is choked, the volumetric flow rate does not vary. The experiments used a probe with orifice diameter of 47 μm and a back pressure of approximately 5 torr.

The FTIR spectrometer proved to be an effective means for measuring the stable species collected with the quartz microprobes. Calibration for each species allowed for the creation of a method for quantitatively measuring the concentrations. The method allowed for quick and easy

quantification of the sample spectra. The method was validated using pure calibration gases and gas mixtures of varying concentration levels. Seven species were quantified and identified including: NO, CO, CO_2, H_2O, C_3H_8, CH_4, and C_2H_6. Only the results for NO, CO, and CO_2 are presented due to limited availability of higher concentrations of the other calibration gases, and the large absorption lines produced for H_2O.

Thermocouple measurements also proved to be rather reliable and consistent with results produced from other experiments and modeling results. Heat losses from the thermocouple to the surroundings created the need for radiation corrections to be incorporated to obtain more accurate temperature measurements. Due to the agreement with the work of Westblom et al [72], it was determined that these alterations did a sufficient job of correcting the temperatures. The corrections for temperature were rather substantial in some cases contributing to an additional 400 K being added to the measured amount. A more accurate method for finding temperatures that does not involve the corrections incorporated is thermometry by OH-LIF, and it is recommended that this be performed in future experiments to obtain more accurate data.

Numerical calculation of species and temperatures for the various fuels was performed using the CHEMKIN software package. The Konnov mechanism was used to perform propane calculations, and a combination of the Gail methyl butanoate mechanism and Konnov mechanism was used to perform calculations for methyl butanoate. The models very accurately predict the temperature profiles obtained experimentally in each of the flames. The NO concentrations obtained in the reaction and post-flame regions of the flame agree well with the predicted values for the stoichiometric MB and propane flames. NO is under-predicted in the rich flames, and over-predicted in the lean flames. While the data for CO and CO_2 mole fractions are over-predicted in all cases. The results from a fixed gas temperature solution are

also presented for the lean and rich cases. There was no substantial difference in the species concentrations predicted by this model and the energy equation solution. Stoichiometric results were unable to be obtained, so it is recommended as future work to run the Gail-Konnov flat flame model for the fixed gas temperature case.

The results of the experiment show that there is not a substantial difference in the measured concentration values of NO. For the stoichiometric, lean, and rich conditions concentrations from the MB flames were slightly lower than those determined for propane. Leading to the conclusion that there is not a considerable increase in the amount of NO produced in methyl ester flames. Modeling results show that the stoichiometric and lean methyl butanoate flames produce slightly lower concentrations of NO than their propane counterparts, while the rich MB flame is predicted to produce slightly more NO than propane. The models also predict that a large portion of NO is produced by the thermal route downstream of the pre-heat zone, and the author predicts that another large contributor in this region is fuel NO. Before the reaction zone, it is believed that most of the NO formation is produced through the prompt route. Further work using the LIF technique would prove beneficial because of the issues encountered in the pre-heat zone of the flame with the NO measurements. It is nearly impossible to predict what NO formation routes contribute to the overall concentration without a substantial change to the experimental setup or use of a different technique.

References

[1] IPCC, 2007, Climate Change 2007 : Synthesis Report, An Assessment of the Intergovernmental Panel on Climate Change.

[2] Chapman L., 2007, "Transport and climate change: a review," Journal of Transport Geography, **15**(5), pp. 354–367.

[3] Fisher B., 2009, "Characterization of gaseous and particulate emissions from combustion of algae based methyl ester biodiesel," Colorado State University.

[4] Duncan R. C., and Youngquist W., 1999, "Encircling the Peak of World Oil Production."

[5] Oman H., 2003, "Energy Sources for the World's Post-Petroleum Era," IEEE AES Systems Magazine, pp. 35–40.

[6] U.S. Energy Information Administration, 2012, "How dependent is the United States on foreign oil?"

[7] Fagerstone K. D., 2011, "Measurement of Direct Nitrous Oxide Emissions From Microalgae Cultivation Under Oxiz and Anoxic Conditions," Colorado State University.

[8] Kohse-Höinghaus K., Osswald P., Cool T. a, Kasper T., Hansen N., Qi F., Westbrook C. K., and Westmoreland P. R., 2010, "Biofuel combustion chemistry: from ethanol to biodiesel.," Angewandte Chemie (International ed. in English), **49**(21), pp. 3572–97.

[9] Department of Energy, 2007, “Alternative Fuel Transportation Program; Replacement Fuel Goal Modification,” **72**(50), pp. 12041–12060.

[10] Banweiss G., Chen J., Buchholz B., and Dibble R., 2007, “A numerical investigation into the anomalous slight NOx increase when burning biodiesel; A new (old) theory,” Fuel Processing Technology, **88**(7), pp. 659–667.

[11] Sheehan J., Camobreco V., Duffield J., and Shapouri H., 2000, An overview of biodiesel and petroleum diesel life cycles.

[12] Lin K. C., Lai J. Y. W., and Violi A., 2011, “The role of the methyl ester moiety in biodiesel combustion: A kinetic modeling comparison of methyl butanoate and n-butane,” Fuel, **92**(1), pp. 16–26.

[13] Environmental Protection Agency, 2002, Analysis of Biodiesel Impacts on Exhaust Emissions.

[14] Lapuerta M., Armas O., and Rodriguez-Fernandez J., 2008, “Effect of biodiesel fuels on diesel engine emissions,” Progress in Energy and Combustion Science, **34**(2), pp. 198–223.

[15] Fisher B., and Marchese A., 2010, “Measurement of Gaseous and Particulate Emissions from Algae-Based Fatty Acid Methyl Esters,” SAE International Journal of Fuels and Lubricants, **3**(2), pp. 292–321.

[16] Fernando S., Hall C., and Jha S., 2006, “NO x reduction from biodiesel fuels,” Energy & Fuels, **20**(1), pp. 376–382.

[17] Feng Q., 2011, “An experimental and modeling study of NOx and soot emissions from biodiesel and its surrogates,” University of Southern California.

[18] Chisti Y., 2007, “Biodiesel from microalgae.,” Biotechnology advances, **25**(3), pp. 294–306.

[19] U.S. Congress, 2007, Energy Independence and Security Act of 2007, Congress, 110th United States, House Bill H.R.6.

[20] Hill S. C., and Smoot L. D., 2000, “Modeling of nitrogen oxides formation and destruction in combustion systems,” Progress in Energy and Combustion Science, **26**, pp. 417–458.

[21] Law C. K., 2006, Combustion Physics, Cambridge University Press, New York.

[22] Fenimore C. P., 1971, “Formation of nitric oxide in premixed hydrocarbon flames,” Symposium (International) on Combustion, **13**(1), pp. 373–380.

[23] Marchese A. J., and Yalin A. P., 2011, “Quantitative Validation of the NCN pathway to prompt NOx (NSF Research Proposal),” pp. 1–19.

[24] Moskaleva L. V., and Lin M. C., 2000, “The spin conserved reaction CH ⎯, N 2 → H ⎯, NCN : A major pathway to prompt NO studied by quantum/statistical theory calculations

and kinetic modeling of rate constant," Proceedings of the Combustion Institute, **28**(3), pp. 2393–2401.

[25] Smith G. P., 2003, "Evidence of NCN as a flame intermediate for prompt NO," Chemical Physics Letters, **367**(5-6), pp. 541–548.

[26] Sutton J., Williams B., and Fleming J., 2008, "Laser-induced fluorescence measurements of NCN in low-pressure CH4/O2/N2 flames and its role in prompt NO formation," Combustion and Flame, **153**(3), pp. 465–478.

[27] Lamoureux N., Desgroux P., El Bakali a., and Pauwels J. F., 2010, "Experimental and numerical study of the role of NCN in prompt-NO formation in low-pressure CH4–O2–N2 and C2H2–O2–N2 flames," Combustion and Flame, **157**(10), pp. 1929–1941.

[28] Sutton J. a., Williams B. a., and Fleming J. W., 2012, "Investigation of NCN and prompt-NO formation in low-pressure C1–C4 alkane flames," Combustion and Flame, **159**(2), pp. 562–576.

[29] Williams B. a., and Fleming J. W., 2007, "Experimental and modeling study of NO formation in 10torr methane and propane flames: Evidence for additional prompt-NO precursors," Proceedings of the Combustion Institute, **31**(1), pp. 1109–1117.

[30] Konnov A. A., 2009, "Implementation of the NCN pathway of prompt-NO formation in the detailed reaction mechanism," Combustion and Flame, **156**(11), pp. 2093–2105.

[31] Szybist J. P., Boehman A. L., Taylor J. D., and McCormick R. L., 2005, “Evaluation of formulation strategies to eliminate the biodiesel NOx effect,” Fuel Processing Technology, **86**(10), pp. 1109–1126.

[32] Mueller C., and Boehman A., 2009, “An experimental investigation of the origin of increased NOx emissions when fueling a heavy-duty compression-ignition engine with soy biodiesel,” SAE paper, **2**(1).

[33] McCormick R. L., Graboski M. S., Alleman T. L., Herring a M., and Tyson K. S., 2001, “Impact of biodiesel source material and chemical structure on emissions of criteria pollutants from a heavy-duty engine.,” Environmental science & technology, **35**(9), pp. 1742–7.

[34] Egolfopoulos F. N. (University of S. C. of A. and M. E., 2009, National Center for Metropolitan Transportation Research Final Report METRANS Research Project 08-01 : Combustion and Emission Characteristics of Biofuels Used for Transportation.

[35] Herbinet O., Pitz W., and Westbrook C., 2008, “Detailed chemical kinetic oxidation mechanism for a biodiesel surrogate,” Combustion and Flame, **154**(3), pp. 507–528.

[36] Wang Y. L., 2011, “An Experimental and Numerical Investigation of Fundamental Combustion Properties of Biofuels,” University of Southern California.

[37] Fisher E., Pitz W., Curran H., and Westbrook C., 2000, “Detailed chemical kinetic mechanisms for combustion of oxygenated fuels,” Proceedings of the combustion institute, **28**(2), pp. 1579–1586.

[38] Gaïl S., Thomson M. J., Sarathy S. M., Syed S. a., Dagaut P., Diévart P., Marchese a. J., and Dryer F. L., 2007, "A wide-ranging kinetic modeling study of methyl butanoate combustion," Proceedings of the Combustion Institute, **31**(1), pp. 305–311.

[39] Dooley S., Curran H. J., and Simmie J. M., 2008, "Autoignition measurements and a validated kinetic model for the biodiesel surrogate, methyl butanoate," Combustion and Flame, **153**(1-2), pp. 2–32.

[40] Huynh L. K., and Violi A., 2008, "Thermal decomposition of methyl butanoate: ab initio study of a biodiesel fuel surrogate.," The Journal of organic chemistry, **73**(1), pp. 94–101.

[41] Cheskis S., and Goldman a., 2009, "Laser diagnostics of trace species in low-pressure flat flame," Progress in Energy and Combustion Science, **35**(4), pp. 365–382.

[42] 2012, "Holthuis and Associates."

[43] Ghoddoussi R., 2005, "An Investigation on Thermal Characteristics of Premixed Counterflow Flames Using Micro-Thermocouples," University of Maryland.

[44] Burton K. A., Ladouceur H. D., and Fleming J. W., 1992, "An improved noncatalytic coating for thermocouples," Combustion science and Technology, **81**, pp. 141–145.

[45] Coleman P. B., 1993, Practical Sampling Techniques for Infrared Analysis, CRC Pres, Inc., Boca Raton, FL.

[46] ThermoNicolet, "OMNIC FT-IR Software, QuantPad User's Guide."

[47] Nogueira M. F. M., 2001, “Effects of dimethyl methylphosphonate on premixed methane flames,” Elsevier.

[48] Shaddix C. R., 1999, “Correcting thermocouple measurements for radiation loss: a critical review,” Proceedings of the 33rd National Heat Transfer Conference, pp. 1–10.

[49] Heitor M. V., and Moreira A. L. ., 1993, “Thermocouples and sample probes for combustion studies,” Progress in Energy and Combustion Science, **19**(3), pp. 259–278.

[50] Collis D. C., and Williams M. J., 1959, “Two-dimensional convection from heated wires at low Reynolds numbers,” Journal of Fluid Mechanics, **6**, pp. 357–384.

[51] Kramers H., 1946, “Heat transfer from spheres to flowing media,” Physica, **12**(2-3), pp. 61–80.

[52] Andrews G. E., Bradley D., and Hundy G. F., 1971, “Hot wire anemometer calibration for measurements of small gas velocities,” International Journal of Heat and Mass Transfer, **15**, pp. 1765–1786.

[53] Ranz W. E., and Marshall W. R., 1952, “Evaporation from drops,” Chemical Engineering Progress, **48**, pp. 141–146, 173–180.

[54] Whitaker S., 1972, “Forced convection heat transfer correlations for flow in pipes, past flat plates, single cylinders, single spheres, and for flow in packed beds and tube bundles,” AIChE Journal, **18**(2), pp. 361–370.

[55] Law C. K., 2006, Combustion Physics, Cambridge University Press, New York, NY.

[56] Fristrom R. M., 1995, Flame Structure and Processes, Oxford University Press, Inc.

[57] Blevins L. G., and Pitts W. M., 1999, "Modeling of bare and aspirated thermocouples in compartment fires," Fire Safety Journal, **33**, pp. 239–259.

[58] Colket III M., Chiappetta L., Guile R., Zabielski M., and Seery D., 1982, "Internal aerodynamics of gas sampling probes," Combustion and Flame, **44**(1-3), pp. 3–14.

[59] Kaiser E. W., Rothschild G., and Lavoie G., 1983, "Effect of Fuel-Air Equivalence ratio and temperature on the structure of laminar propane-air flames," Combustion Science and Technology, **33**(1-4), pp. 123–134.

[60] Stepowski D., Puechberty D., and Cottereau M., 1981, "Use of laser-induced fluorescence of OH to study the perturbation of a flame by a probe," Symposium (International) on Combustion, Elsevier, pp. 1567–1573.

[61] Hartlieb A. T., Atakan B., and Kohse-Höinghaus K., 2000, "Effects of a sampling quartz nozzle on the flame structure of a fuel-rich low-pressure propene flame," Combustion and flame, **121**(4), pp. 610–624.

[62] Cattolica R. J., Yoon S., and Knuth E. L., 1982, "OH Concentrations in an Atmospheric Methane-Air Flame from Molecular Beam Mass Spectrometry and Laser Absorption Spectroscopy," Combustion Science and Technology, **28**, p. 225.

[63] Castaldi M. J., 1997, "Formation of Polycyclic Aromatic Hydrocarbons (PAH) in Laminar, Premixed, Flat, Atmospheric Flames," University of California, Los Angeles.

[64] Yi A., and Knuth E., 1986, “Probe-induced concentration distortions in molecular-beam mass-spectrometer sampling,” Combustion and flame, **63**(3), pp. 369–379.

[65] kaiser E., Hothschild W., and Lavoie G., 1984, “Chemical species profiles of laminar propane-air flames,” Combustion Science and Technology, **41**(5-6), pp. 271–289.

[66] Seery D. J., and Zabielski M. F., 1989, “Comparisons between flame species measured by probe sampling and optical spectrometry techniques,” Combustion and Flame, **78**(1), pp. 169–177.

[67] Sarathy S. M., 2010, “Chemical kinetic modeling of biofuel combustion.”

[68] Reaction Design, 2010, “CHEMKIN / CHEMKIN-PRO Theory Manual CHEMKIN ® Software,” (August), pp. 1–360.

[69] Simmie J. M., 2003, “Detailed chemical kinetic models for the combustion of hydrocarbon fuels,” Progress in Energy and Combustion Science, **29**(6), pp. 599–634.

[70] NIST, 2011, “NIST Chemical Kinetics Database.”

[71] NIST, 2012, “NIST Chemistry WebBook.”

[72] Westblom U., Fernandez-Alonso F., Mahon C. R., Smith G. P., Jeffries J. B., and Crosley D. R., 1994, “Laser-induced fluorescence diagnostics of a propane/air flame with a manganese fuel additive,” Combustion and flame, **99**(2), pp. 261–268.

Appendix

The following tables present the measured concentrations and standard errors for the lean, stoichiometric, and rich conditions for methyl butanoate and propane fuels including the following species: NO, CO, CO_2, H_2O, C_3H_8, and CH_4.

Table A-1: Lean MB measured concentration results

LEAN METHYL BUTANOATE						
Height (mm)	**NO (PPM)**	**Error (1.96*σ)**	**Error (1*σ)**	**CO (PPM)**	**Error (1.96*σ)**	**Error (1*σ)**
0	16.36	4.54	2.32	7578.66	124.75	63.65
1	24.74	8.83	4.50	10236.96	143.69	73.31
1.5	37.35	13.42	6.84	12494.26	320.50	163.52
2	34.40	9.50	4.85	11218.21	86.51	44.14
3	9.85	3.65	1.86	15063.21	176.96	90.29
4	8.48	4.79	2.45	12472.43	157.05	80.13
6	8.39	5.09	2.60	9932.45	196.80	100.41
8	9.06	4.88	2.49	8054.68	164.55	83.95
Height (mm)	**CO2 (PPM)**	**Error (1.96*σ)**	**Error (1*σ)**	**H2O (PPM)**	**Error (1.96*σ)**	**Error (1*σ)**
0	4762.18	1619.07	826.06	52090.42	823.92	420.37
1	7529.37	2615.29	1334.33	58183.93	1060.99	541.32
1.5	10618.81	4097.90	2090.76	91539.78	1499.60	765.10
2	9427.44	3522.36	1797.12	24521.99	1424.24	726.65
3	24047.50	2346.43	1197.16	43572.20	1036.26	528.71
4	31788.24	1332.96	680.08	45636.71	673.80	343.78
6	36448.84	1545.34	788.44	52107.04	731.24	373.08
8	35364.72	1758.68	897.28	58943.35	691.10	352.60
Height (mm)	**C3H8 (PPM)**	**Error (1.96*σ)**	**Error (1*σ)**	**CH4 (PPM)**	**Error (1.96*σ)**	**Error (1*σ)**
0	3402.25	167.48	85.45	1255.22	827.79	422.34
1	2812.51	138.23	70.53	1248.72	678.73	346.29
1.5	1759.99	88.08	44.94	1360.02	428.31	218.53
2	338.09	17.94	9.15	699.12	91.57	46.72
3	134.02	11.49	5.86	936.03	61.07	31.16
4	158.92	13.24	6.75	1079.91	69.68	35.55
6	251.53	18.77	9.58	1179.93	90.38	46.11
8	124.40	10.74	5.48	943.88	72.56	37.02

Table A-2: Lean propane measured concentration results

LEAN PROPANE						
Height (mm)	**NO (PPM)**	**Error (1.96*σ)**	**Error (1*σ)**	**CO (PPM)**	**Error (1.96*σ)**	**Error (1*σ)**
0	32.49	8.53	4.35	10249.02	432.84	220.84
0.5	55.65	17.55	8.95	12927.76	518.72	264.65
1.5	76.88	25.64	13.08	14880.92	454.14	231.70
2	65.61	20.47	10.44	13803.17	619.55	316.10
2.5	13.05	4.51	2.30	17028.44	497.13	253.64
6	10.99	3.94	2.01	9916.11	625.09	318.92
8	11.07	5.05	2.58	8323.16	654.92	334.14
Height (mm)	**CO2 (PPM)**	**Error (1.96*σ)**	**Error (1*σ)**	**H2O (PPM)**	**Error (1.96*σ)**	**Error (1*σ)**
0	7773.04	4422.11	2256.18	61217.23	2701.69	1378.41
0.5	11017.58	5505.58	2808.97	42501.88	2480.07	1265.34
1.5	12896.05	7758.75	3958.55	44483.10	2962.22	1511.34
2	11533.74	7074.16	3609.26	35261.48	2755.34	1405.79
2.5	25745.71	4210.55	2148.24	36254.68	1700.51	867.61
3	14544.03	9974.32	5088.94	36047.41	3939.06	2009.73
3.5	22268.68	4069.67	2076.36	28622.77	1638.18	835.80
4	25143.65	1434.65	731.96	42513.20	719.91	367.30
5	30525.32	1502.92	766.79	56783.44	714.82	364.71
6	33371.23	1634.25	833.80	87509.63	732.25	373.60
8	31031.80	1528.72	779.96	33991.59	676.88	345.35
Height (mm)	**C3H8 (PPM)**	**Error (1.96*σ)**	**Error (1*σ)**			
0	3704.81	569.12	290.37			
0.5	9558.73	634.11	323.53			
1.5	11074.24	612.11	312.30			
2	11333.70	694.45	354.31			
2.5	124.47	12.65	6.45			
3	675.97	22.19	11.32			
3.5	122.58	14.42	7.35			
4	123.51	14.19	7.24			
5	173.39	20.75	10.59			
6	210.21	26.25	13.39			
8	151.26	18.44	9.41			

Table A-3: Stoichiometric MB measured concentration results

STOICHIOMETRIC METHYL BUTANOATE						
Height (mm)	**NO (PPM)**	**Error (1.96*σ)**	**Error (1*σ)**	**CO (PPM)**	**Error (1.96*σ)**	**Error (1*σ)**
0	21.17	5.23	2.67	8862.44	173.18	88.36
1	64.52	20.78	10.60	16596.16	267.77	136.62
1.5	67.55	20.83	10.63	16643.44	184.65	94.21
2	33.70	9.58	4.89	18101.73	231.04	117.88
3	8.35	3.97	2.03	15354.62	182.59	93.16
4	10.18	4.45	2.27	12826.36	164.56	83.96
6	7.48	4.54	2.32	15231.89	239.02	121.95
8	9.56	5.64	2.88	14587.83	204.51	104.34
Height (mm)	**CO2 (PPM)**	**Error (1.96*σ)**	**Error (1*σ)**	**H2O (PPM)**	**Error (1.96*σ)**	**Error (1*σ)**
0	4957.52	2912.15	1485.79	56169.60	1156.81	590.21
1	11916.99	9594.15	4894.98	85567.29	3604.34	1838.95
1.5	14108.76	9024.82	4604.50	21548.40	3541.06	1806.66
2	16748.34	11019.63	5622.26	35000.30	4399.09	2244.43
3	31461.10	1404.66	716.66	47851.72	688.29	351.17
4	30578.25	1327.46	677.28	33002.93	610.63	311.54
6	48348.30	1889.05	963.80	70804.99	694.71	354.45
8	46578.68	2026.75	1034.06	76798.24	732.10	373.52
Height (mm)	**C3H8 (PPM)**	**Error (1.96*σ)**	**Error (1*σ)**	**CH4 (PPM)**	**Error (1.96*σ)**	**Error (1*σ)**
0	4950.61	266.47	135.95	3354.24	1782.52	909.45
1	2014.01	97.54	49.77	1712.14	491.50	250.77
1.5	748.54	38.75	19.77	1233.37	195.68	99.84
2	166.70	14.11	7.20	1004.41	69.44	35.43
3	144.48	11.58	5.91	833.67	60.11	30.67
4	144.69	11.62	5.93	940.66	62.67	31.97
6	368.80	27.14	13.85	1728.99	131.48	67.08
8	275.99	19.32	9.86	1023.54	85.38	43.56

Table A-4: Stoichiometric propane measured concentration results

STOICHIOMETRIC PROPANE						
Height (mm)	**NO (PPM)**	**Error (1.96*σ)**	**Error (1*σ)**	**CO (PPM)**	**Error (1.96*σ)**	**Error (1*σ)**
0	36.41	10.26	5.23	10595.68	726.73	370.78
0.5	58.52	17.52	8.94	12628.43	621.56	317.12
1	65.92	20.53	10.47	13393.80	832.20	424.59
1.5	64.97	20.36	10.39	14740.82	755.95	385.69
2	23.15	5.77	2.94	15186.57	729.54	372.21
5	11.54	4.47	2.28	12167.71	703.70	359.03
6	9.91	4.03	2.06	11589.79	628.87	320.85
8	10.75	3.69	1.88	11130.15	645.88	329.53
Height (mm)	**CO2 (PPM)**	**Error (1.96*σ)**	**Error (1*σ)**	**H2O (PPM)**	**Error (1.96*σ)**	**Error (1*σ)**
0	5845.02	6669.82	3402.97	49235.70	2531.26	1291.46
0.5	5798.16	9562.21	4878.68	27103.24	3611.88	1842.80
1	6015.00	10845.15	5533.24	45488.20	3990.06	2035.74
1.5	6290.19	13400.98	6837.23	44374.11	5174.15	2639.87
2	11896.80	10235.50	5222.19	45903.30	3956.82	2018.79
2.5	19146.72	2244.57	1145.19	36907.17	929.20	474.08
3	24197.68	1454.99	742.34	38266.34	675.63	344.71
3.5	26518.06	1562.92	797.41	40227.09	707.20	360.82
4	26690.29	1628.10	830.66	41542.75	718.59	366.63
5	29054.18	1587.15	809.77	43443.45	722.90	368.83
6	30628.31	1536.20	783.78	37035.02	688.15	351.10
8	29389.63	1551.63	791.65	33088.77	682.03	347.98
Height (mm)	**C3H8 (PPM)**	**Error (1.96*σ)**	**Error (1*σ)**			
0	10692.88	681.74	347.82			
0.5	11133.02	592.93	302.52			
1	2322.68	32.69	16.68			
1.5	543.29	25.66	13.09			
2	199.02	23.38	11.93			
2.5	148.39	18.16	9.26			
3	153.72	19.56	9.98			
3.5	205.14	24.18	12.34			
4	197.15	23.50	11.99			
5	165.45	20.02	10.22			
6	146.82	17.73	9.05			
8	129.49	13.69	6.98			

Table A-5: Rich MB measured concentration results

RICH METHYL BUTANOATE						
Height (mm)	**NO (PPM)**	**Error (1.96*σ)**	**Error (1*σ)**	**CO (PPM)**	**Error (1.96*σ)**	**Error (1*σ)**
0	24.19	6.55	3.34	9594.44	161.11	82.20
1	50.66	15.43	7.87	14246.14	160.74	82.01
1.5	43.97	13.69	6.99	14836.46	199.62	101.85
2	42.88	14.57	7.43	19517.43	308.43	157.36
3	8.00	4.14	2.11	17732.46	403.37	205.80
4	4.70	5.86	2.99	14946.57	517.47	264.01
6	6.97	3.85	1.97	12775.86	177.77	90.70
8	7.65	3.75	1.91	10098.13	163.29	83.31
Height (mm)	**CO2 (PPM)**	**Error (1.96*σ)**	**Error (1*σ)**	**H2O (PPM)**	**Error (1.96*σ)**	**Error (1*σ)**
0	3945.27	4454.99	2272.96	32482.24	1712.49	873.72
1	7561.98	8964.21	4573.58	51846.60	3512.19	1791.93
1.5	6539.57	11046.14	5635.78	46910.64	4403.22	2246.54
2	12737.48	14769.97	7535.70	79315.57	5875.75	2997.83
3	27156.79	2700.56	1377.83	57291.31	1094.33	558.33
4	27217.32	3494.90	1783.11	60581.25	637.00	325.00
6	28493.18	1382.94	705.58	48389.57	671.89	342.80
8	30098.77	1487.10	758.72	62357.99	753.77	384.58
Height (mm)	**C3H8 (PPM)**	**Error (1.96*σ)**	**Error (1*σ)**	**CH4 (PPM)**	**Error (1.96*σ)**	**Error (1*σ)**
0	1904.88	92.53	47.21	1171.73	460.06	234.73
1	589.64	30.71	15.67	1269.23	156.07	79.63
1.5	235.58	18.71	9.55	1254.97	86.74	44.25
2	222.51	19.19	9.79	1526.70	92.59	47.24
3	204.69	18.95	9.67	1385.27	91.02	46.44
4	1063.66	96.21	49.09	2188.86	357.10	182.19
6	385.39	24.70	12.60	1447.59	120.37	61.41
8	276.68	21.64	11.04	1294.58	103.49	52.80

Table A- 6: Rich propane measured concentration results

RICH PROPANE						
Height (mm)	**NO (PPM)**	**Error (1.96*σ)**	**Error (1*σ)**	**CO (PPM)**	**Error (1.96*σ)**	**Error (1*σ)**
0	16.29	5.72	2.92	1437.99	7.57	3.86
0.5	25.56	6.07	3.10	7875.01	847.71	432.51
1	37.38	11.12	5.67	9679.71	739.11	377.10
1.5	46.14	14.66	7.48	11480.87	1076.48	549.22
2	34.66	10.06	5.13	11662.91	993.51	506.89
5	10.67	4.66	2.38	16334.14	1112.98	567.85
6	6.49	4.73	2.41	14643.64	634.01	323.48
8	7.48	5.98	3.05	10615.28	1037.22	529.19
Height (mm)	**CO2 (PPM)**	**Error (1.96*σ)**	**Error (1*σ)**	**H2O (PPM)**	**Error (1.96*σ)**	**Error (1*σ)**
0	4835.36	6181.09	3153.62	59505.29	1352.33	689.97
0.5	5447.79	7784.47	3971.67	48284.11	1977.20	1008.78
1	3451.31	9519.60	4856.94	41227.23	3120.98	1592.34
1.5	3670.61	12131.82	6189.70	36908.72	4102.32	2093.02
2	2545.93	11934.82	6089.19	33303.70	4420.18	2255.19
2.5	9954.07	11151.60	5689.59	105631.17	4122.85	2103.50
3	16410.08	5099.89	2601.98	64368.57	1783.58	909.99
3.5	17177.86	845.40	431.33	63526.32	1097.80	560.10
4	17086.13	1105.51	564.04	61011.57	990.71	505.46
5	16334.14	1112.98	567.85	53900.42	857.86	437.69
6	14643.64	634.01	323.48	93550.20	639.29	326.17
8	17106.06	3284.11	1675.57	113356.76	644.46	328.81
Height (mm)	**C3H8 (PPM)**	**Error (1.96*σ)**	**Error (1*σ)**			
0	6621.85	291.86	148.91			
0.5	4692.43	223.05	113.80			
1	2270.73	70.85	36.15			
1.5	1564.53	93.59	47.75			
2	667.22	60.88	31.06			
2.5	687.53	71.24	36.35			
3	534.36	51.63	26.34			
3.5	447.90	44.78	22.85			
4	373.64	42.11	21.49			
5	279.19	34.62	17.66			
6	275.32	31.82	16.24			
8	742.18	85.52	43.63			

The following lines of text include MATLAB files used in computation of the thermocouple radiation corrections for temperature.

PROP.M – calculates the gas phase properties for air and fuel/air mixtures at the measured thermocouple temperature

```
%%USE IN THERMOCOUPLE CORRECTIONS%%

%User must specify values for the following for their desired constituents:
%Mole fractions
%Molecular weights
%Pressure
%Diameters of the thermocouple bead and wire
%Lennard-Jones well depth and collision diameters
%Mass flow rate of the oxidizer and fuel (and their molecular weights)
%Air fuel ratio
%Things to do with emissivity of the thermocouple....

%NOTE: The below calculations are valid for a binary mixture only.

function[cpair,gammaair,kair,visair,rhoair,rhomix,v] = prop(T)

%Species mole fractions (AIR)
xo2 = 0.21;
xn2 = 0.79;

%Molecular Weights (kg/kmol)
mwo = 15.9994;
mwn = 14.0067;
mwo2 = 31.99886;
mwn2 = 28.01344;
mwair = xo2*mwo2 + xn2*mwn2;

%Constants
avo = 6.022*(10^26);        %avogadros number (molecules/kmol)
kb = 1.38065*(10^-23);      %Boltzmann constant (J/K)
R = 8314;                   %(J/kmolK)
Rair = 8314/mwair;

%Mass of molecules (kg)
mo = mwo/avo;
mn = mwn/avo;
mo2 = mwo2/avo;
mn2 = mwn2/avo;
mair = mwair/avo;

%Pressure
Ptorr = 100;               %Torr
P = 133.3224*Ptorr;        %Pascals
```

```
%Diameters and areas
db = .06452;                %burner diameter (m)
Ab = pi()*(db/2)^2;         %burner area (m^2)
dtc = 450E-6;             %thermocouple bead diameter (m)
dw = 300E-6;                %thermocouple wire diameter (m)

%%%%%%%%%%%%%%%%%%%%%%%%%%%%%%%%%%%%%%%%%%%%%%%%%%%%%%%%%%%%%%%%%%%%%%%%%%%%%%%
                            %SPECIFIC HEAT%
%%%%%%%%%%%%%%%%%%%%%%%%%%%%%%%%%%%%%%%%%%%%%%%%%%%%%%%%%%%%%%%%%%%%%%%%%%%%%%%

%Load in specific heat and temp files from JANAF tables for O2 and N2.
%Define the values in the loaded files then convert the cp values from the
%JANAF tables given as molar specific heats(J/molK) and convert to J/kgK.
%Create polynomial fit, using polyfit, of the given data, then evaluate
%using the polyval function.

if T >= 300 && T < 1000
    oxygen = load('oxygen300-1000.csv','-ascii');
    nitrogen = load('nitrogen300-1000.csv','-ascii');
    TO = oxygen(:,1);
    TN = nitrogen(:,1);
    CPO = (oxygen(:,2)./mwo2).*1000;
    CPN = (nitrogen(:,2)./mwn2).*1000;
    cpO = polyfit(TO,CPO,5);
    cpN = polyfit(TN,CPN,5);
    cpo = polyval(cpO,T);
    cpn = polyval(cpN,T);
elseif T >= 1000 && T <=3000
    oxygen = load('oxygen1000-3000.csv','-ascii');
    nitrogen = load('nitrogen1000-3000.csv','-ascii');
    TO = oxygen(:,1);
    TN = nitrogen(:,1);
    CPO = (oxygen(:,2)./mwo2).*1000;
    CPN = (nitrogen(:,2)./mwn2).*1000;
    cpO = polyfit(TO,CPO,5);
    cpN = polyfit(TN,CPN,5);
    cpo = polyval(cpO,T);
    cpn = polyval(cpN,T);
end

%Calculate specific heat, Cv
cvo = cpo - kb/mo2;
cvn = cpn - kb/mn2;

%Calculate Cp/Cv, gamma
gammao2 = cpo./cvo;
gamman2 = cpn./cvn;

%Calculate specific heat of air, cp (J/kgK)
cpair = (xo2.*cpo + xn2.*cpn);
cvair = cpair - kb/mair;
gammaair = cpair./cvair;
```

```
%%%%%%%%%%%%%%%%%%%%%%%%%%%%%%%%%%%%%%%%%%%%%%%%%%%%%%%%%%%%%%%%%%%%%%%%%%%%%%%
                %THERMAL CONDUCTIVITY, VISCOSITY, AND DENSITY%
%%%%%%%%%%%%%%%%%%%%%%%%%%%%%%%%%%%%%%%%%%%%%%%%%%%%%%%%%%%%%%%%%%%%%%%%%%%%%%%

%epsilon/boltzmann constant - Lennard Jones potential well depth, K
epso = 80;
epsn = 71.4;
epso2 = 107.40;
epsn2 = 97.53;

%Sigma - Lennard Jones Collision Diameters, Angstrom = 10^-10 m
sigmao = 2.750*(10^-10);
sigman = 3.2989*(10^-10);
sigmao2 = 3.458*(10^-10);
sigman2 = 3.621*(10^-10);

%Calculate T* - characteristic temperature for N and O
Tso = T./epso;
Tsn = T./epsn;
Tso2 = T./epso2;
Tsn2 = T./epsn2;

%Calculate collision integral Omega(2,2)(T*,delta*) for N and O
%For nonpolar gases delta*=0

o22o = 1.155.*(Tso).^(0.1462) + 0.3945*exp(-0.6672.*Tso)...
    +2.05*exp(-2.168.*Tso);

o22n = 1.155.*(Tsn).^(0.1462) + 0.3945*exp(-0.6672.*Tsn)...
    +2.05*exp(-2.168.*Tsn);


o22o2 = 1.155.*(Tso2).^(0.1462) + 0.3945*exp(-0.6672.*Tso2)...
    +2.05*exp(-2.168.*Tso2);


o22n2 = 1.155.*(Tsn2).^(0.1462) + 0.3945*exp(-0.6672.*Tsn2)...
    +2.05*exp(-2.168.*Tsn2);


%Calculate viscosity coefficient of the monatomic gases, kg/ms
viso = (5/16)*(sqrt(pi()*mo*kb.*T)./(pi().*sigmao^2.*o22o));
visn = (5/16)*(sqrt(pi()*mn*kb.*T)./(pi().*sigman^2.*o22n));


%Calculate viscosity of the diatomic gases, kg/ms
viso2 = (5/16)*(sqrt(pi()*mo2*kb.*T)./(pi().*sigmao2^2.*o22o2));
visn2 = (5/16)*(sqrt(pi()*mn2*kb.*T)./(pi().*sigman2^2.*o22n2));


%Calculate thermal conductivity of monatomic gases, W/mK
ko = (15/4).*(kb.* viso)./mo;
```

```
kn = (15/4).*(kb.* visn)./mn;


%Calculate thermal conductivity of diatomic gases, W/mK
%Eucken formula for polyatomic gases, uses gamma calculated in specific
%heat portion of this function
ko2 = ko.*((3/5)+ (4./(15.*(gammao2-1))));
kn2 = kn.*((3/5)+ (4./(15.*(gamman2-1))));


%Calculate Phi of the mixture, for use in viscosity and thermal
%conductivity equations
phimix = (1/sqrt(8))*sqrt(1+mwo2/mwn2).*(1+sqrt(viso2./visn2)...
    .*((mwn2/mwo2)^(1/4))).^2;


%Calculate Viscosity of the mixture, kg/ms
visair = viso2./(1+(1/xo2).*(xn2.*phimix))...
    + visn2./(1+(1/xn2).*(xo2.*phimix));


%Calculate Thermal Conductivity of the mixture, W/mK
kair = ko2./(1+(1.065/xo2).*(xn2.*phimix))...
    + kn2./(1+(1.065/xn2).*(xo2.*phimix));

%Calculate density of the air mixture, kg/m^3
rhoair = P./(Rair.*T);

%%%%%%%%%%%%%%%%%%%%%%%%%%%%%%%%%%%%%%%%%%%%%%%%%%%%%%%%%%%%%%%%%%%%%%%%%%%%%%%
                                %FLOW VELOCITY%
%%%%%%%%%%%%%%%%%%%%%%%%%%%%%%%%%%%%%%%%%%%%%%%%%%%%%%%%%%%%%%%%%%%%%%%%%%%%%%%
%Mass flow rate and molecular weight of oxidizer and fuel
mdot = 9.71E-5;       %From data logger data
mwa = 28.97;
mwf = 44.01;

%Air-Fuel Ratio
af = 23.8;

%Mass fractions
yf = 1/(af+1);
ya = 1 - yf;

%MW of mix
mwmix = 1/(yf/mwf + ya/mwa);

rhomix = P./((R/mwmix).*T);

% %Mole fractions
% xf = yf*mwmix/mwf;
% xa = ya*mwmix/mwa;
%
```

```
% %Partial pressures of fuel and air in mixture (Pascal)
% Pf = xf*P;
% Pa = xa*P;
%
% %Gas Constants
% Rf = R/mwf;
% Ra = R/mwa;
%
% %Calculate density (kg/m^3)
% rhof = Pf./(Rf.*T);
% rhoa = Pa./(Ra.*T);
% rhomix = xf.*rhof + xa.*rhoa;

%Calculate mixture velocity (m/s)
v = mdot./(rhomix.*Ab);


%%%%%%%%%%%%%%%%%%%%%%%%%%%%%%%%%%%%%%%%%%%%%%%%%%%%%%%%%%%%%%%%%%%%%%%%%%%%%%%
                                    %REFERENCES%
%%%%%%%%%%%%%%%%%%%%%%%%%%%%%%%%%%%%%%%%%%%%%%%%%%%%%%%%%%%%%%%%%%%%%%%%%%%%%%%

%Specific heat data taken from:
%NIST-JANAF Thermochemical Tables
%http://kinetics.nist.gov/janaf/

%Calculations for thermal conductivity and viscosity taken from:
%Law, C.K. Combustion Physics (2006) Chapter 4:Transport Phenomena
```

CORRECTED_TEMP_CALC.M – Begins with inputs of the thermocouple temperature, emissivity, and an initial guess at the gas stream temperature, then pulls the properties from the PROP.M file along with the equations derived from the heat transfer energy balance discussed in Chapter 2 and iterates to calculate the gas temperature.

```
%%USE IN THERMOCOUPLE CORRECTIONS%%

%Thermocouple temperature (K)
Tb =1199;

%Wall temperature (K) (for radiation calculations)
Tw = 313.1;

%Emissivity
emis = .5203;

%Temperature of the freestream gas (K)
Tinf = 2000;

%Thermocouple bead diameter (m)
dwire = .450E-3;

%Stefan-Boltzmann constant (W/m^2K^4)
sigma = 5.67E-8;


tol = 0.01;
e = 100;
n=1;

while e >= tol
    Tinf
    [cpair,gammaair,kair,visair,rhoair,rhomix,v] = prop(Tinf)
    Re = (rhoair.*v.*dwire)./visair
    Pr = (visair.*cpair)./kair

    Nu = 2.0 + 0.6.*Re.^(2/3).*Pr.^(1/3)  %Ranz and Marshall Correlation

    h = Nu.*kair./dwire

    Tg = Tb + (emis.*sigma.*(Tb.^4 - Tw.^4)).*(dwire./(kair.*Nu))
    e(n) = abs(Tg-Tinf)
    Tinf = Tg
    Tm = (1/2).*(Tb+Tinf);
    n = n+1
end
```